ULTRAFAST IMAGING: LASER INDUCED ELECTRON DIFFRACTION

by

JUNLIANG XU

B.S., University of Science and Technology of China, 2006

AN ABSTRACT OF A DISSERTATION

submitted in partial fulfillment of the
requirements for the degree

DOCTOR OF PHILOSOPHY

Department of Physics
College of Arts and Sciences

KANSAS STATE UNIVERSITY
Manhattan, Kansas
2012

Abstract

Imaging of molecules has always occupied an essential role in physical, chemical and biological sciences. X-ray and electron diffraction methods routinely achieve sub-Å spatial resolutions but are limited to probing dynamical timescales longer than a picosecond. With the advent of femtosecond intense lasers, a new imaging paradigm emerges in last decade based on laser-induced electron diffraction (LIED). It has been placed on a firm foundation by the quantitative rescattering theory, which established that large-angle e-ion elastic differential cross sections (DCS) can be retrieved from the LIED spectrum. We further demonstrate that atomic potentials can be accurately retrieved from those extracted DCSs at energies from a few to several tens of electron volts. Extending to molecules, we show mid-infrared (mid-IR) lasers are crucial to generate high-energy electron wavepackets ($>$ 100 eV) to resolve the atomic positions in a molecule. These laser-driven 100 eV electrons can incur core-penetrating collisions where the momentum transfer is comparable to those attained in conventional keV electron diffraction. Thus a simple independent atom model (IAM), which has been widely used in conventional electron diffractions, may apply for LIED. We theoretically examine and validate the applicability of IAM for electron energies above 100 eV using e-molecule large-angle collision data obtained in conventional experiments, demonstrating its resolving powers for bond lengths about 0.05 Å. The Validity of IAM is also checked by an experimental LIED investigation of rare gas atoms in the mid-IR regime. We show that the electron's high energy promotes core-penetrating collisions at large scattering angles, where the e-atom interaction is dominated by the strong short range *atomic-like* potential. Finally, we analyze the measured LIED spectrum of N_2 and O_2 at three mid-IR wavelengths (1.7, 2.0, and 2.3 μm). As expected, the retrieved bond lengths of N_2 at three wavelengths are about same as the equilibrium N_2 bond length. For O_2, the

data is also consistent with a bond length contraction of 0.1 Å within 4-6 fs after tunnel ionization. This investigation establishes a foundation for this novel imaging method for spatiotemporal imaging of gas-phase molecules at the atomic scale.

ULTRAFAST IMAGING: LASER INDUCED ELECTRON DIFFRACTION

by

JUNLIANG XU

B.S., University of Science and Technology of China, 2006

A DISSERTATION

submitted in partial fulfillment of the
requirements for the degree

DOCTOR OF PHILOSOPHY

Department of Physics
College of Arts and Sciences

KANSAS STATE UNIVERSITY
Manhattan, Kansas
2012

Approved by:

Major Professor
Dr. Chii-Dong Lin

Copyright

Junliang Xu

2012

Abstract

Imaging of molecules has always occupied an essential role in physical, chemical and biological sciences. X-ray and electron diffraction methods routinely achieve sub-Å spatial resolutions but are limited to probing dynamical timescales longer than a picosecond. With the advent of femtosecond intense lasers, a new imaging paradigm emerges in last decade based on laser-induced electron diffraction (LIED). It has been placed on a firm foundation by the quantitative rescattering theory, which established that large-angle e-ion elastic differential cross sections (DCS) can be retrieved from the LIED spectrum. We further demonstrate that atomic potentials can be accurately retrieved from those extracted DCSs at energies from a few to several tens of electron volts. Extending to molecules, we show mid-infrared (mid-IR) lasers are crucial to generate high-energy electron wavepackets ($>$ 100 eV) to resolve the atomic positions in a molecule. These laser-driven 100 eV electrons can incur core-penetrating collisions where the momentum transfer is comparable to those attained in conventional keV electron diffraction. Thus a simple independent atom model (IAM), which has been widely used in conventional electron diffractions, may apply for LIED. We theoretically examine and validate the applicability of IAM for electron energies above 100 eV using e-molecule large-angle collision data obtained in conventional experiments, demonstrating its resolving powers for bond lengths about 0.05 Å. The Validity of IAM is also checked by an experimental LIED investigation of rare gas atoms in the mid-IR regime. We show that the electron's high energy promotes core-penetrating collisions at large scattering angles, where the e-atom interaction is dominated by the strong short range *atomic-like* potential. Finally, we analyze the measured LIED spectrum of N_2 and O_2 at three mid-IR wavelengths (1.7, 2.0, and 2.3 μm). As expected, the retrieved bond lengths of N_2 at three wavelengths are about same as the equilibrium N_2 bond length. For O_2, the

data is also consistent with a bond length contraction of 0.1 Å within 4-6 fs after tunnel ionization. This investigation establishes a foundation for this novel imaging method for spatiotemporal imaging of gas-phase molecules at the atomic scale.

Table of Contents

List of Figures

List of Tables

Acknowledgments

The fruition of my PhD work is achieved with help of many people, but a few should be singled out in particular. First and foremost, I would like to thank my advisor Dr. Chii-Dong Lin for his continuous support and guidance during my PhD years at Kansas State University, especially his support which helped me go through my bad and good times in my PhD years. He brought me to the field of dynamic molecular imaging, and has trained me to have a right perspective on physics problems. My thanks also go to the previous and present members in his group, especially Dr. Zhangjin Chen, Dr. Anh-Thu Le, Dr. Toru Morishita, and Dr. Samuel Micheau, with whom I have benefited from numerous discussions. Their constructive suggestions helped me quickly grasp the concepts about HATI and LIED.

Second, I would like to thank Dr. Lou DiMauro, Dr. Pierre Agostini, and Dr. Cosmin Blaga at the Ohio State University for the wonderful cooperation and the beneficial discussions. In particular, I enjoyed the conversations with Cosmin, which gave me a valuable insight into the problems we were working on together. It is after the discussion with him that I formed the idea about bond relaxation in O_2^+.

Third, special thanks are due my friends Yujun Wang for helping to improve my computational skills, He Wang for helping me understanding the experiments for strong laser physics, and Siddique Khan for helping to improve the presentations of my dissertation and final talk.

Fourth, I want to give my thanks to my committee members, Dr. Brett Esry, Dr. Vinod Kumarappan, and Dr. Christine Aikens, and outside chairperson Dr. J. Kenneth Shultis for serving on my thesis committee. I also want to thank Dr. Brett Esry and Dr. Christine Aikens for their excellent teachings, which benefit my entire project.

Finally, I would love to acknowledge my parents and my wife Ziyan Liu. I most certainly could never have accomplished my PhD work and make any achievement without their unqualified, loving and sacrificial support.

Dedication

To my wife Ziyan, our coming baby Duoduo, and my parents.

Chapter 1

Introduction

Imaging, or the direct probing of the atomic structure of matter, has always occupied an essential role in physical, chemical and biological sciences[1,2]. For decades, the invention of imaging techniques, such as electron and X-ray diffraction, neutron diffraction, optical and NMR spectroscopy, has enlarged our knowledge about static structures of matter, ranging from single molecules to crystals, and from small molecules to macromolecules such as DNA and proteins, and to cells and viruses[1,3–7]. The microscopic structure of matter, especially the spatial arrangement of atoms in a molecule, is essential to its physical and chemical properties, and is the starting point to study its (electronic, vibrational, and rotational) spectrum, possible isomeric configurations, chemical reactivity and functions[8]. Great effort has been consistently made for about one century to push forward the frontier of structural determination[9]. With the advent of femtosecond lasers and extremely bright free electron X-ray lasers, it is quite promising for us to monitor and control molecular transformations, such as chemical reactions and phase transitions, with atomic scale spatiotemporal resolutions[9–14]. A new age of structural dynamics has come. However, despite all the advances of the microscopic and spectroscopic tools for studying molecular dynamics, there are still many difficulties and challenges for us to directly "watch" the motions of atoms during these processes.

1.1 Electron and X-ray Diffraction

1.1.1 Static Structural Imaging

Among all the conventional imaging techniques, electron and X-ray diffraction are the two principal experimental tools for the determination of molecular structures, which provide us our knowledge about static geometrical information of almost all small molecules and most of the biomolecules[3,5,15,16]. Electrons and photons strongly interact with either the atomic cores in the molecule or electronic charge density cloud, and are scattered from the molecule, producing a spatial diffraction pattern, which bears the imprint of molecular structure. A certain Fourier-transform-based inversion procedure can be taken to reconstruct the molecule from the diffraction spectrum. To the present day, electron and X-ray diffraction still serve as the major probes in stereochemical experiments, and routinely achieve atomic scale spatial resolutions[11,17,18].

Both electron and X-ray diffraction microscopes have been invented for about one century. Usage of X-ray photons to study the molecular structure, especially for crystalline molecules, is attributed to Von Laue's discovery of X-ray diffraction from crystals in 1912. One year later, W. H. Bragg and W. L. Bragg proposed the law of diffraction from crystals, known as Bragg's law, and started to use X-rays to determine the structural constants of single crystals such as NaCl[19]. This method later was developed into a powerful imaging technique, X-ray crystallography, to determine the atomic positions inside the unit cells of a crystal, and has since made a tremendous impact in physics, chemistry, biology and other fields[4,20,21]. The idea of using electrons as probes is rooted in the revolutionary concept that electron has wave/particle duality in early 1920s, which along with other ground-breaking ideas marked the beginning of a new quantum era[3]. The first electron diffraction investigation of structural determination was carried out by Mark and Wierl in 1930, and carbon tetrachloride was studied in gas phase, which initiated the field of gas-phase electron diffraction (GED)[22].

Electron and X-ray diffraction have many similarities, but also have some sharp differ-

ences. Both techniques use high energy electrons or photons as probes. Electron energy is about 10-100 keV, and X-ray photon energy is about 1-10 keV. Electron or X-ray beams impinging on molecular samples are usually externally prepared and collimated, and the incident electron or photon energy is so high that it is often assumed that they interact with each individual atom in the molecule, which is the so-called independent atom model (IAM)[3,23]. Electrons or photons are elastically scattered off the molecule producing a diffraction spectrum in momentum space, which is inversely transformed into an atomic position map in real space by use of tools such as inverse sine transform for electrons and Fourier transform for X-rays. On the other hand, electrons possess charge and mass, and thus the strong interaction between electrons and the irradiated samples gives strong scattering signals, which is about 5-6 orders of magnitude higher than that of X-rays[3,24]. In turn, the elastic mean free path of X-rays in the sample is longer than that of electrons, so it is easier to apply X-ray diffraction to molecules in condensed phases and macromolecules such as DNA and proteins, while electron diffraction is better suited for studying small molecules in the gas phase, thin films and surfaces[1,12]. Thus far, gas phase electron diffraction and X-ray crystallography complement, rather than compete with each other, providing us the vast majority of static molecular structures. One of the latest works is the X-ray crystallography investigation of the subunit structures of the ribosome, a protein-making machine, by V. Ramakrishnan, T. A. Steitz, and A. E. Yonath, who were jointly awarded the 2009 Nobel Prize in Chemistry[25].

In up-to-date gas phase electron diffraction structure analysis, the internuclear distances obtained could be accurate to the order of 0.001 Å, which can be improved after a careful error analysis, by taking accounting for several sources of errors, e.g., effects of anharmonic vibrations[3]. The spatial resolution achieved by X-ray crystallography is a little inferior to that of GED, about 0.01 Å in favorable cases, using a single crystal sample of sufficient size (typically 1 mm×1 mm×1 mm) and high flatness[4,21,26]. However, X-ray diffraction analysis of molecular structures is greatly limited by the crystal size and the X-ray photon flux[4].

For instance, the intensities of Bragg peaks are proportional to N^2, where N is the total number of unit cells in the crystal, as a result, the strength of diffraction signals decreases parabolically with the crystal size. Unfortunately, for many important molecules of interest, especially biomolecules such as membrane proteins, it is particularly challenging to grow large enough crystals of good quality[12,21,27]. To obtain diffraction signals of adequate quality, reducing the size of crystals in turn requires an necessary increase in X-ray dose. Today, the best X-ray source utilizes synchrotron radiation from relativistic electron beams in storage rings. Its low photon flux leads to a scattering signal weaker than that of GED by 6 orders of magnitude[12], which greatly limits the spatial resolution obtainable. An additional problems for small crystals is the radiation damage, which can cause deterioration of the samples due to the long exposure time needed to obtain a diffraction image with high contrast[28]. New X-ray sources with high intensities generated by free electron lasers (FEL) and methods such as coherent X-ray diffraction imaging and femtosecond X-ray diffraction have been proposed to overcome the difficulties of X-ray diffraction[10,29], which will be described in the following part of this chapter. The spatial resolutions for micrometer- and nanometer-sized objects obtained using X-ray FELs is from few to tens of nanometers, and still has space to improve[27,29]. Miao et al.[30] has predicted theoretically that with the above new techniques, the resolution can reach up to 2.5 Å for submicrometer biomeolcules.

1.1.2 Ultrafast Dynamic Imaging: Challenges

The concept of the atomic structure of matter, especially the nature of chemical bonding, was well established more than a half century ago[31–33], and ever since, the theoretical study of structural transformations of matter, e.g. transition-state theory formulated by M. G. Evans and M. Polanyi in 1935, has never been halted[34,35]. The world is intrinsically dynamic, and static images of matter do not tell how things happen. It has become a dream of chemical physicists to "watch" the migration of atoms during a chemical reaction, conformational dynamics, or other kinds of molecular processes, and it is still one of the grand scientific

challenges of our times.

As we know, the molecular transformation is based on the motions of atoms, which is on the femtosecond time scale, e.g., the molecular vibrational period is about 20 fs[36]. In order to capture atomic motions, one generally needs a "camera" with a "shutter speed" on the order of one femtosecond. Experimental observation of molecular dynamics on the atomic level didn't occur until 1980s when the technology of pulse compression became available, which can reduce the optical pulse widths to sub-picosecond. In 1985, reaction dynamics, photodissociation of the ICN molecule in gas phase was first studied using optical pump-probe spectroscopy by A. H. Zewail's group[37]. The dissociation process is initiated and clocked by an optical ultraviolet pump pulse and the reaction progress is monitored by the other optical ultraviolet probe pulse which arrives at different time delays with respect to the clock pump pulse. They were able to observe the ICN transient. Soon after, in 1987, with the help of femtosecond optical pulses, they could resolve in real time the transition-state configuration *en route* to the dissociation[38–40]. Dr. Zewail was awarded the 1999 Nobel Prize in Chemistry for his extraordinary contribution of dynamic imaging of transient structures[41].

However, for optical (and also NMR) pump-probe spectroscopy, the signals are sensitive to only specific energy states of a molecule or one of its functional groups[42,43], and thus it is hard to convert the signals into structural information, e.g., bond lengths, bond angles and torsion angles. Electrons and X-ray photons are still the most preferable probes to directly "see" the transient positions of atoms in a molecule. For this purpose, temporal resolution needs to be integrated with electron and X-ray diffraction. Femtosecond ultrashort electron or X-ray pulses are required to meet this time resolution standard[44–46].

The representative method of time-resolved electron diffraction is ultrafast electron diffraction (UED), developed from the static imaging technique of gas-phase electron diffraction[1,47–49]. UED experiments have been performed in a number of laboratories in the last decade or so. These pulsed electrons are generated by femtosecond lasers from photocath-

odes and accelerated to tens or hundreds of keVs[50,51]. Important applications of UED have provided structural changes on atomic level of molecules in chemical reactions. The first direct observation of transient structural changes was done by Zewail's group at Caltech in 1999, and elimination reaction of 1,2-diiodotetrafluoroethane ($C_2F_4I_2$) was the focus of interest. With temporal resolution less than 10 ps, they were able to trace the structural details of $C_2F_4I_2$ in course of the reaction, and succeeded to observe the nonbridged structure of the reactive intermediate C_2F_4I after one iodine atom was removed from $C_2F_4I_2$[52,53]. The time resolution was pushed down to sub-picosecond (about 600 fs) for the first time by Siwick et al. in 2003 for the study of structural evolution of aluminum undergoing a laser-induced melting phase transition[54]. However, sub-picosecond resolution is still relatively poor compared with the timescales of many chemical molecular processes. Moreover, repulsion between electrons in one pulse, known as space charge effects, dominate the temporal profile of an electron pulse, and it is hard to break the femtosecond barrier for ultrafast electron diffraction[1,55]. Application of UED is limited to probing slow dynamics timescales longer than a picosecond.

For time-resolved X-ray diffraction, laser-driven plasma-based femtosecond hard X-ray pulses (100 to 500 fs) have been utilized to experimentally study the dynamics of phonons and phase transitions in simple solid systems[56,57]. But to date, their low photon flux (10^4-10^8 photons per pulse) inhibits us from resolving the atomic details of the samples[46,58]. Synchrotrons can generate X-ray pulses with a higher intensity (10^9-10^{10} photons per pulse), however the best pulse duration obtained is about 100 ps, far off the femtosecond requirement[12,46]. It is worth noting that femtosecond X-ray pulses are needed not only for the purpose of resolution, but also for avoiding X-ray irradiated damage on crystalline samples due to the long exposure time. The damage processes usually happen on order of tens of femtosecond to picoseconds, so diffraction has to terminate before damage begins[59,60].

Over all, though electron and X-ray diffraction gives good spatial resolutions in their respective fields, the major and also the most notable limitation of both techniques is the

poor temporal resolutions they achieved up to now. How to obtain the femtosecond temporal resolution, i.e., how to make femtosecond electron or X-ray pulses, becomes the main challenge in time-resolved electron and X-ray diffraction of our times. For electron diffraction, single electron diffraction has been proposed as a new approach to improve the time resolution[1,51]. As we know, a single electron packet is fully coherent[1], and moreover, there is no space charge effect as there is only one electron in each pulse. This method is still on the conceptual level and needs more investigation. For X-ray diffraction, the novel radiation source, free electron laser, promises to generate intense ultrashort X-ray pulses and will greatly extend X-ray diffraction microscopy to the femtosecond realm with spatial resolutions on the atomic scale[10,12]. It has been reported that ultrabright (more than 10^{12} photons per pulse) X-ray pulses at a wavelength of 0.69 nm with durations of 10, 70, and 200 fs have been available in LCLS at SLAC[27]. In addition, the unprecedented high X-ray photon flux also lifts the limitation on the size of the crystalline molecules[61]. X-ray FELs have been used to study the structures of nanocrystals[27] and hold promise for investigating molecules in liquid and gas phases and even for imaging a single macromolecule in a single short[12]. But X-ray FELs are costly and often require large-scale facilities, and are only becoming available at several spots in the world, e.g. SPring-8 in Japan, LCLS at Stanford SLAC, and FLASH at DESY in Hamburg. They are usually shared and beamtime at them is limited. Also, there is still a long way to go for diffraction of X-ray FELs to get atomic scale spatiotemporal resolution.

1.2 Strong Laser Physics and Laser Induced Electron Diffraction

The advent of femtosecond intense infrared (IR) lasers brings light to observation of atomic motions in molecules undergoing ultrafast dynamics on a timescale of a molecular vibrational period[62–68]. Presently, femtosecond optical lasers at various intensities with tunable wavelengths are available in university laboratories worldwide, and the femtosecond pulse

duration opens up new ways to improve spatiotemporal resolution, most commonly by mating ultrashort IR laser pulses with time-resolved electron and X-ray diffraction. Most recently, laser-induced photoelectron emission from metal surfaces was studied in Germany and succeeded to generate femtosecond (100 fs) single-electron pulses experimentally, which is an important breakthrough in ultrafast atomic-scale imaging[69]. Laser-assisted keV electron scattering from Xe atom was carried out by R. Kanya et al.[70], and they were able to observe side signals (though weak) around the incident electron energy in the diffraction image. Those extra signals convey the structural information of the target, and the presence of them are due to interaction of the incident electron and the the assisted laser field (electron energy shift by $\pm$ photon energy). In this way the temporal resolution is integrated into the scattering through the laser field. They demonstrated that this could be a new method of time-resolved gas-phase electron diffraction.

Alternatively, a whole new imaging paradigm emerged in the last decade based on the new phenomena that occur in the IR-laser-matter interaction, especially when the laser electric field strength is comparable with the Coulomb field (intensity $\sim 10^{16}$ W/cm^2) that governs the electron dynamics in atoms or molecules[71]. When an atom or molecule is exposed to such an intense linearly polarized laser pulse, the target atom or molecule will be tunnel ionized, releasing a valence electron. Born in the laser's oscillating field, the electron can fly directly to the detector, dubbed the direct electron, or may also be driven back in a semiclassical motion by the laser field to recollide with the parent ion, whereupon it may elastically scatter, kick out another electron, or photo-recombine into the initial electronic state, correspondingly incurring highly nonlinear phenomena: high-energy above threshold ionization (HATI), nonsequential double ionization (NSDI), and high-order harmonic generation (HHG), respectively[72,73]. Since both electron scattering and photoionization are conventional tools for probing the structure of matter, there has been great interest in using the returning electrons for self-imaging the target[13,74–76]. This possibility has been placed on a firm foundation with the recent development of quantitative rescattering (QRS) the-

ory[13,76–78] (other equivalent work see papers by Čerkić et al.[79] and Frolov et al.[80]). In particular, the QRS established that the large-angle electron-ion elastic differential cross section (DCS) can be retrieved from experimental HATI electron momentum spectra and that photo-recombination dipole matrix elements can be retrieved from the intensity and the phase of HHG. Since rescattering occurs in sub-optical cycle, HHG and HATI spectra may serve to determine molecular structure, with the benefit of achieving few-femtosecond temporal resolutions offered by the short laser pulses.

In recent years, HHG spectroscopy as a tool for determining the structure of molecules has generated a big wave of excitement[81–83] since it was reported that a tomographic procedure can be used to extract the wavefunction of the outermost molecular orbital[81] of N_2. However, the tomographic procedure is based on a number of questionable assumptions and approximations[84,85], among them is that the continuum electron wavefunction can be represented by a plane wave. This assumption, which is essential to the tomographic procedure, is in strong contradiction to the well-established electron-ion collision theories. This limitation makes the use of orbital tomography questionable as a practical tool for retrieving structural information of a molecule.

1.2.1 Laser-Induced Electron Diffraction and Quantitative Rescattering Theory

Meanwhile, elastic scattering of those returning electrons from the target ions, a process dubbed laser-induced electron diffraction (LIED), also gets masses of attention for its potential for structural determination[76,77,79,80,86–88]. The basics of laser-induced electron diffraction is the same as ultrafast electron diffraction, except that the probing electron pulse is generated from its parent target based on tunnel ionization by an intense laser. The HATI spectrum generated by the rescattering electrons in the far field conveys target structural information.

In Figure 1.1 we show a typical angular-resolved photoelectron spectrum in momentum space for Ar, in which the p_z axis is parallel to the laser polarization direction. The laser

is a 5 fs pulse at the peak intensity of $1.0{\times}10^{14}$ W/cm^2 with the wavelength of 800 nm, and the spectrum is obtained by solving the time-dependent Schrödinger equation (TDSE). The general features of the spectrum have been well understood with the aid of the classical model and strong field approximation (SFA) (e.g., see the pioneer work by Corkum[72], Becker et al.[89], and Chen et al.[90]). In this figure, two specific energies of 2 U$_p$ and 10 U$_p$ are marked, where U$_p$ is the electron ponderomotive energy, i.e., the cycle-averaged electron quiver energy, and scales as U$_p \propto I\lambda^2$, where I and λ are the field's intensity and wavelength, respectively. The 2 U$_p$ energy is often used to roughly differentiate the low-energy and high-energy above-threshold-ionization photoelectrons, and the 10U$_p$ cutoff energy is the maximum energy that electrons can reach in the laser field predicted by the classical model.
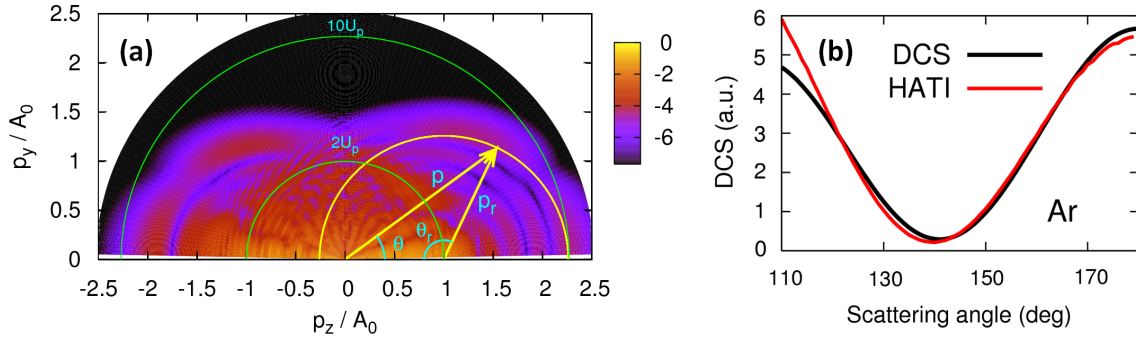
Figure 1.1: *(a) A typical 2D momentum distribution of photoelectrons for Ar atom in a 5-cycle laser pulse at the peak intensity of $1{\times}10^{14}$ W/cm^2 and the wavelength of 800 nm. (b) Comparison between extracted DCS from HATI spectrum from (a) at p_r=1.22 a.u. and corresponding elastic scattering DCS at the same energy. Figure is adapted from a paper by Chen et al.[77]*

Direct electrons are abundant and contribute to the low-energy distribution with maximum cutoff energy 2 U$_p$[90]. The returning electrons propagate longer in the field than the direct ones, and during propagation those electrons can acquire significant kinetic energy from the field prior to recollision and then are scattered in the far field off the target ion, extending the spectrum up to 10 U$_p$[77,90]. In the strong field approximation, the detected electron momentum, $\boldsymbol{p}=(p,\theta)$, can be deconstructed into the momentum during recollision,

$\boldsymbol{p}_r{=}(p_r,\theta_r)$, using the vector relationship $\boldsymbol{p}{=}\boldsymbol{p}_r-\boldsymbol{A}_r$ (see Figure 1.1(a)), where the additional momentum $\boldsymbol{A}_r$ is the vector potential of the laser field at recollision, and θ and θ_r are the detected angle and rescattering angle, respectively. To be specific, electrons backscattered at $180°$ with the maximum rescattering energy $p_r^2/2 = 3.17\mathrm{U}_p$ would reach the $10~\mathrm{U}_p$ cutoff. It is worth noting that those backscattering electrons gain additional momentum from the field, resulting in a larger detected momentum and separability from the direct ones, while the electrons scattered in the forward direction, as shown in Figure 1.1(a), completely mix with the direct ones[77,90].

According to QRS, the momentum distribution $D(p,\theta)$ along the circumference defined by a constant p_r (the yellow solid circle in Figure 1.1(a)) can be factorized simply as:

$$D(p,\theta) = W(p_r)\sigma(p_r,\theta_r), \tag{1.1}$$

where $W(p_r)$ and $\sigma(p_r,\theta_r)$ are the momentum distribution of electron returning wavepacket (RWP) and the electron DCS for *free* electron scattering on the target ion, respectively. We comment that in QRS the extracted DCS is not absolute, and RWP $W(p_r)$ is the overall normalization factor to the absolute DCS, which does not depend on the rescattering angle. As an illustration, in Figure 1.1(b) we show the DCS extracted from the HATI spectrum in (a) at rescattering momentum $p_r{=}1.22$ a.u. and compare it with theoretically calculated DCS for Ar at the same energy. We can see they agree well with each other in the angular region shown. The validity of QRS has been established in theory for detected energies from about $4~\mathrm{U}_p$ to $10~\mathrm{U}_p$, i.e., rescattering energies from $1~\mathrm{U}_p$ to $3.17~\mathrm{U}_p$[77]. It is worth emphasizing that from HATI spectrum only DCSs at large rescattering angles can be extracted. The interference between forward-scattered and direct electrons makes the DCS extraction at small angles nearly intractable.

In the last few years, following the idea of QRS, several experiments have demonstrated that *field-free* elastic electron-target-ion differential cross sections, or diffraction images, can be extracted from the HATI spectra for atoms and molecules[91–95]. Same as GED, these diffraction images are the input, from which target structural information can be retrieved by

using certain inversion algorithms. However, as all these dated experiments were performed near 800 nm, the wavelength of the Ti-Sapphire lasers, the returning electrons have energies of few tens of eV, too low, for example, to resolve the position of atoms in a molecule. Recall that in a strong laser field, electron rescattering energy is characterized by the ponderomotive energy U_p, which scales as $U_p \propto I\lambda^2$. By increasing the laser wavelength, e.g., using mid-infrared (mid-IR) lasers, the returning electron kinetic energy can reach up to hundreds of eV, and the electron de Broglie wavelength is comparable to interatomic distances (~ 1 Å) in a molecule, promising a good spatial resolution. Nevertheless, a rigorous study in both theory and experiments is essential to demonstrate if rescattered electrons can serve as an imaging tool for ultrafast dynamic system with adequate spatiotemporal resolution[96,97].

1.3 Overview of this Dissertation

This thesis is dedicated to developing a novel imaging technique, laser induced electron diffraction, to film the structural changes of a dynamic system with atomic scale spatiotemporal resolution.

In Chapter 2, we aim at finding a robust inversion method which can be used to obtain accurate model potentials for rare-gas atoms based on the differential elastic-scattering cross sections[98]. Treating theoretically simulated DCSs as the "experimental" data, with help of genetic algorithm (GA), we successfully identified each atom and retrieved their corresponding effective nuclear charges.

In Chapter 3, we demonstrate it is possible to use intense mid-infrared lasers to probe the structure of a molecule[96]. Mid-IR lasers can generate electrons with energies high enough (above 100 eV) and de Broglie wavelengths matching typical molecular bond lengths. We also establish the validity of a simple model, independent atom model, to accurately describe diffraction images at large scattering angles for electron collisions above 100 eV. Bond lengths in average accuracy of about 0.05 Å are retrieved from DCSs for CO_2, N_2, and C_2H_4 at collision energies above 100 eV obtained in conventional electron-gun experiments. We also

demonstrate in theory the importance of aligning molecules for 3D imaging of molecules.

In Chapter 4, we extract high-quality e-ion collision DCSs from experimental HATI data of rare-gas atoms in the mid-IR regime[97]. We also prove that at this high energy, backscattered electrons are able to penetrate the atomic core, such that long-range Coulomb potential plays little role in the collision in backward direction. Therefore e-neutral and e-ion DCSs are identical.

In Chapter 5, we apply the new image technique to experimental LIED data with mid-IR lasers for N_2 and O_2, which was taken by Agostini-DiMauro's group at the Ohio State University, and show the extracted bond lengths[68]. The N-N bond length retrieved from the data agrees with that for N_2 to within 0.05 Å. For O_2, the retrieved bond length is consistently much smaller than the known O-O bond length of 1.21 Å. Instead, it is much closer to the bond length of O_2^+, 1.12 Å. We interpret this result in terms of bond relaxation of O_2 following tunnel ionization. O_2^+ has a vibrational period of 17 fs while the returning time for a 2000 nm laser is about 5-6 fs, thus allowing the two O atoms to relax from its initial separation of 1.21 Å to the new separation of 1.12 Å of O_2^+. This investigation establishes the foundation for this novel method for dynamic imaging of transient molecules with sub-Å spatial and few-femtosecond temporal resolution.

Finally a short remark is given to summarize the entire dissertation.

Atomic units are used in this dissertation unless otherwise indicated.

Chapter 2

Atomic Imaging: Genetic-Algorithm Implementation of Inverse Scattering[*]

The deconvolution procedure for extracting *field-free* electron-ion differential cross sections from the LIED distribution is provided by the framework of the recently developed quantitative rescattering theory. It opens up a possibility for structural determination using LIED DCSs. However, quantum-mechanical inverse scattering problems are not well investigated in atomic or molecular systems. Amos and co-workers[99] extracted the spin-orbit interaction from elastic-scattering cross sections at 5 eV between electrons with Xe atoms. No such investigations have been carried out for the collision between electrons with atomic or molecular ions. In this chapter, we report our results of imaging attempts with atoms, and demonstrate the feasibility of genetic algorithm for the retrieval of atomic potentials using backscattering DCSs between free electrons and atomic ions for electron energies from a few to several tens of electron volts. We first explain in Sec. 2.1 how GA functions and how the DCSs are calculated quantum mechanically if a central potential $V(r)$ is given. In Sec. 2.2, we used a model potential of Ar to generate the DCS, and then used GA to retrieve this potential. This method is shown to work for the model Ar, Ne, Kr, and Xe atoms. In Sec. 2.3 we used DCSs calculated with R-matrix (RMAT) approach as "experimental" data. We assume random errors of no more than 10% and angular resolution of 5° and only

---

the relative cross sections are known. Using GA we are able to obtain the potentials $V(r)$ for Ne, Ar, and Kr. For Xe, the potential which gives the best fit of the cross sections turns out to be incorrect, but the next better-fit one is correct, which indicates the importance of the "prior" knowledge about the target. A short summary and discussion of extending this work for dynamic chemical imaging with infrared lasers are given in the last section. The materials in this chapter have been published in Phys. Rev. A by Xu. el al.[98] in 2009.

2.1 Inverse Scattering and Genetic Algorithm

2.1.1 Statement of the problem

Suppose elastic differential scattering cross sections $\sigma_e(k, \theta)$ have been obtained between an incident electron and a singly charged atomic ion, over a range of electron momentum and scattering angles experimentally, we wish to construct a spherically symmetric model potential $V(r)$ which will reproduce the DCS as close to $\sigma_e(k, \theta)$ as possible. Since the range of k and θ will be limited, it will not be treated as a standard inverse scattering problem. Instead, we seek the solution by using GA. The potential will be parameterized in the form

$$V(r; \boldsymbol{a}) = -\frac{1 + a_1 e^{-a_2 r} + a_3 r e^{-a_4 r} + a_5 e^{-a_6 r}}{r}. \tag{2.1}$$

Since we are treating neutral atoms, the asymptotic charge in Eq. 2.1 has been set to 1.0. We assume that we do not know the target, but for small r, the target nucleus charge is related to the coefficients $\{a_i\}$ by $Z = 1 + a_1 + a_5$. Note that in this model, we treat the atom using single active electron approximation. Rare gas atoms will be used for this test.

The parameter set $\boldsymbol{a} = \{a_1, a_2, a_3, a_4, a_5, a_6\}$ forms a six-dimensional search space. For each known possible solution, $\boldsymbol{a}$, which is called an individual in GA, we first calculate the DCS, $\sigma(k, \theta; \boldsymbol{a})$, for the scattering by the potential $V(r; \boldsymbol{a})$. The fitness of this individual is then calculated from a fitness/objective function

$$\chi^2(\boldsymbol{a}) = \sum_{i,j} k_i^4 [\sigma(k_i, \theta_j; \boldsymbol{a}) - \sigma_e(k_i, \theta_j)]^2. \tag{2.2}$$

Note that we use weighted DCS, $k^2\sigma$, in order to give more or less equal weight to the DCS at different energies. Obviously individuals with lower fitness values are considered better designs, and we aim to find a parameter set $\boldsymbol{a} = \{a_i\}$ with possibly lowest fitness using GA.

We comment that the model potential approach for the DCS calculation used here neglects the electron exchange, core polarization and other many-electron correlation effects. This approximation is adequate for electron scattering for energies above 10 eV and more. The DCS calculated from model potential method are in good agreement with those from the R-matrix calculations, see Section 2.1.3.

2.1.2 The genetic algorithm

In this work we used the GA driver, GA v1.7a, implemented by David Carroll, written in Fortran language[100]. In this code, binary encoding of the parameter set $\{a_i\}$ is adopted. Both Simple GA (SGA) and micro-GA (or μGA) can be used. We use micro-GA in this work. Similar to SGA[101,102], two operators are employed in micro-GA: (parent) selection and crossover. Both GA's start with an initial population, i.e., a group of candidate parameter sets, which are randomly selected from the search space. Next, the fitness of each individual is evaluated, which identifies their survival ability.

In the following evolutionary process, to create offspring for the next generation which will totally replace the current population, parents are selected according to their fitness. In other words, the fitter individuals will be emphasized more in hope that in turn they will have offspring with even lower fitness. The selection scheme applied in the work is tournament selection with tourney size 2. In this scheme, 2 candidate individuals will be randomly chosen with shuffling technique; the fitter will then win out to be one mate; the other mate will be fixed by running another tournament.

Afterwards, marriage of all pairs of mates will generate the new generation, whose genetic construction descends from their parents by crossover. It is worthy of pointing out again that crossover is performed on the basis of binary encodings instead of real-valued encodings.

In more detail, each individual, an ordered list of the 6 real-valued parameters in each set, will be encoded into a binary sequence with each bit representing a "gene". In this study, uniform crossover is adopted in which gene exchange happens at each bit locus with probability p_{cross}. Elitism is also applied which simply retains the current best fit individual in the next generation, in case that it may be destroyed by crossover. GA practice tells us elitism could efficiently cover against the negativeness of crossover and significantly improve the GA's performance. Different from SGA, micro-GA does not perform mutation operation on the offspring.

Once the next generation is created, a new round of evolution procedure starts over again. This loops until the maximum number of generations G_{max} set previously is reached and ends with output of the best parameter set found by then.

Besides the difference in mutation from SGA, micro-GA evolves only a small population (typically population size N_{pop} is 4∼10), which will largely cut down the number of fitness-function evaluations and the computer time. Nevertheless, genetic diversity is not able to be maintained for many generations if "the population evolves in normal GA fashion"[103]. To prevent premature convergence, similarity of the whole population is checked for every generation. The genes of the best individual in each generation will be compared with the rest population locus by locus. If the variability, defined as the weight of the non-identical bits out of the total bits, is less 5%, the micro-GA will restart with the best individual and randomize the others.

2.1.3 The calculation of differential elastic scattering cross sections

Since the fitness function is based on the elastic DCS, we describe briefly how the DCS is calculated for each candidate potential $V(r; \boldsymbol{a})$. First, we separate out the long-range Coulomb potential, such that

$$V(r) = -\frac{1}{r} + V_S(r), \tag{2.3}$$

in which $V_S(r)$ is the short-range potential. In standard quantum mechanics textbooks, $V(r)$ is called a modified Coulomb potential. The total differential scattering amplitude for such a potential can be written as

$$f(\theta) = f_c(\theta) + f_S(\theta),$$ (2.4)

where $f_c(\theta)$ is the Coulomb scattering amplitude,

$$f_c(\theta) = -\frac{\eta}{2k\sin^2\frac{\theta}{2}}e^{-\mathrm{i}\left\{\eta\ln\left[\sin^2(\theta/2)\right]-2\sigma_0\right\}}$$ (2.5)

with $\eta = -1/k$ and $\sigma_0 = \arg[\Gamma(1 + i\eta)]$. The scattering amplitude f_S from the short-range potential $V_S(r)$ is given by

$$f_S(\theta) = \sum_{l=0}^{\infty}\frac{2l+1}{k}e^{2\mathrm{i}\sigma_l}e^{\mathrm{i}\delta_l}\sin\delta_l P_l(\cos\theta).$$ (2.6)

where the Coulomb phase shift for each partial wave is

$$\sigma_l = \arg[\Gamma(l + 1 + i\eta)]$$ (2.7)

and δ_l is the phase shift from the short-range potential.

For the present purpose, we do not have experimental DCS, $\sigma_e(k,\theta)$. Thus we generate the "experimental" data in two ways. One is to start with a given model potential for a given atom to generate the DCS. We then use the GA, and see if we can recover this potential. Alternatively, we can use the R-matrix method[104] to calculate the DCS. In the R-matrix method, the target states are expressed as configuration-interaction expansion of Hartree-Fock orbitals. The resulting close-coupling equations for the continuum electron are solved with the R-matrix method. Note that in RMAT calculation, all the electrons in the atom are considered, *i.e.,* not in the single active electron approximation.

2.1.4 GA parameters and restrictions on the potential parameters

This is an indirect fitting procedure. We want to construct the potential $V(r; \boldsymbol{a})$ by best fitting the elastic DCS. In sum, there are 4 GA parameters: population size N_{pop}, crossover

rate p_{cross}, maximum number of generations G_{max}, and initial random number seed i_{seed} which is negative to warm up the random number generator. The computer time mainly depends on the total number of fitness evaluations which is proportional to N_{pop} and G_{max}. Generally speaking, smaller population size will make the GA run faster and yet evolution flow converges slower; while, larger G_{max} surely lowers the risk of getting a nonconverged best fit but will linearly increase the computer time. Thus we balance computer time and GA convergence, but give the priority to the latter. For micro-GA, $p_{cross} = 0.5$ is appropriate for uniform crossover and we prefer $N_{pop} = 5 \sim 6$. We set G_{max} a number as large as possible within the limit of computer time that we are willing to accept. Using micro-GA, the computer time is shorter, but at the expense of slower evolution convergence. Another way to reduce computer time is to put some restrictions on the potential parameters. For example, the nuclear charge Z should be between 1 and 118, and the effective charge $Z_{eff}(r; \boldsymbol{a}) = -rV(r; \boldsymbol{a}) > 0$ be a decreasing function of radius r, i.e., $Z'_{eff}(r; \boldsymbol{a}) < 0$. For the parameter sets $\boldsymbol{a}$ which do not satisfy these conditions, there is no need to further calculate the DCS. We simply set a very large fitness value for them. Note that the inverse problem does not guarantee a unique solution in general. This is also true for GA. These additional constraints are useful for helping to sort out the acceptable solutions.

2.2 GA Fitting with Elastic DCS Generated from a Given Model Potential

In this first test, we feed the DCS generated from a known potential $V(r)$. The range of k is taken to be [0.3, 2.0] with 21 equal-spaced grid points. The scattering angle θ runs from $120°$ to $180°$ with an increment of $1°$. The GA parameters are set up with $N_{pop} = 6$ and $G_{max} = 6400$. We chose Ar for this test, using the model potential from[105]. In Figure 2.1(a) the "experimental" DCS surface is shown (note that the DCS is weighted by k^2). In the test, we set i_{seed} to a series of numbers from -50 to -1500 in step of 50, which results in assorted curves in Figure 2.1(b), ending with different fitness values at generation $G_{max} = 6400$. Note
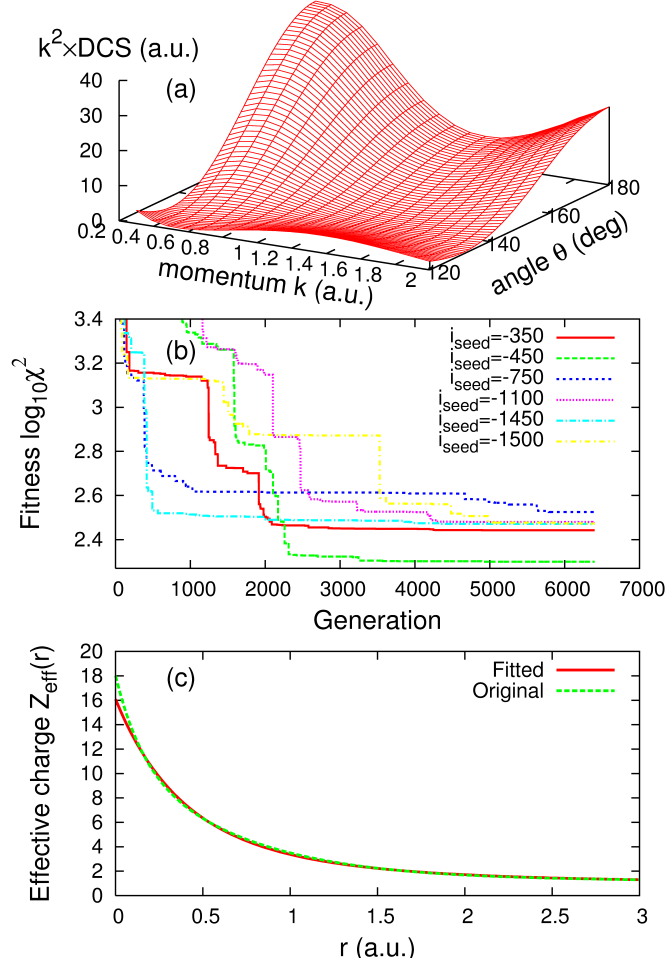
Figure 2.1: *(a) Weighted elastic DCS of Ar feeded in the micro-GA, for momentum $k \in [0.3, 2.0]$ and angle $\theta \in [120°, 180°]$. (b) Evolution of the best fitness per generation associated with different random number generator seeds i_{seed}. (c) Comparison of the fitted and the original effective charge $Z_{eff}(r)$.*

that only six curves with the lowest fitness are shown in Figure 2.1(b) for clarity. However, it is difficult to draw a simple rule about the final behavior of fitness curves with different i_{seed}, as two vicinal seeds could have the fitness scattered far away from each other at the end, and vice versa. It is therefore fair to say that GA outcomes are "randomly" distributed. In this study, 30 seeds, i.e., 30 independent runs deem capable of providing a reasonably good fit.

The fitted potential from this test run is shown in Figure 2.1(c), which is compared to

the input potential. Good agreement between the two can be seen. The ratio of the error is less than 4% over all range of r except near the origin where the error is 10%. Nevertheless, from GA, we obtained $1+a_1+a_5$=16.1 which is close to Z=18 for Ar.
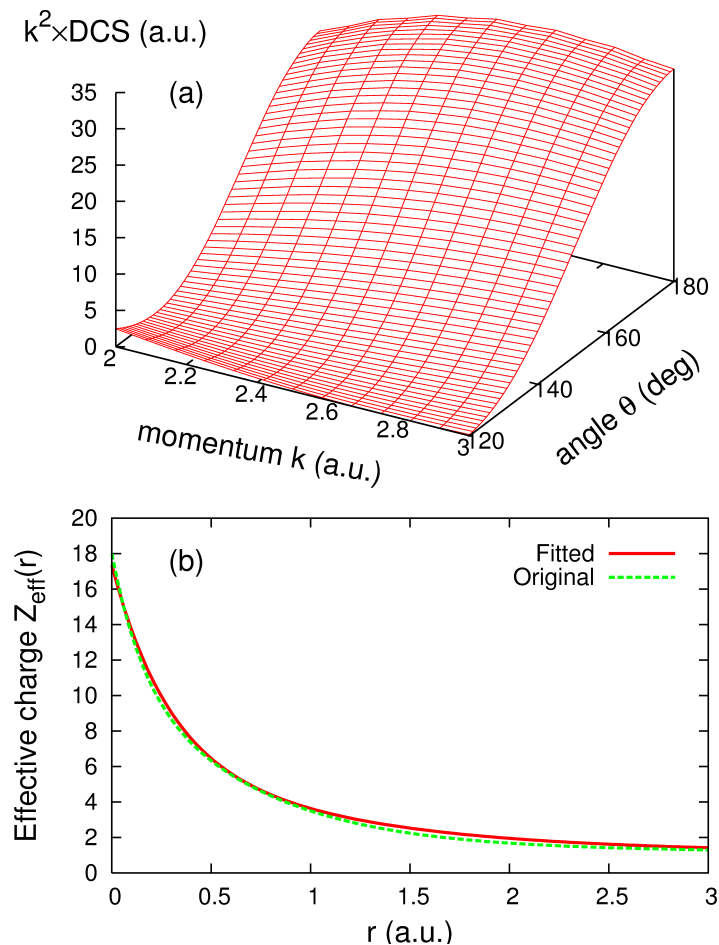
Figure 2.2: *(a) Weighted DCS of Ar for $k \in [2.0, 3.0]$ and $\theta \in [120°, 180°]$. (b) Comparison of the fitted and the original effective charge $Z_{eff}(r)$.*

In Figure 2.1, the "experimental" data were selected for the region of k=[0.3, 2.0]. Since low-energy electrons do not penetrate near the nucleus, this may explain why the retrieved potential there is not as accurate as we like. We next used "experimental" data for k=[2.0, 3.0]. The DCS surface in this range is shown in Figure 2.2(a). The potential obtained from GA is compared to the input potential in Figure 2.2(b). We can see clear improvement in the agreement in the small-r region. The nuclear charge calculated from $1+a_1+a_5$=17.35 is
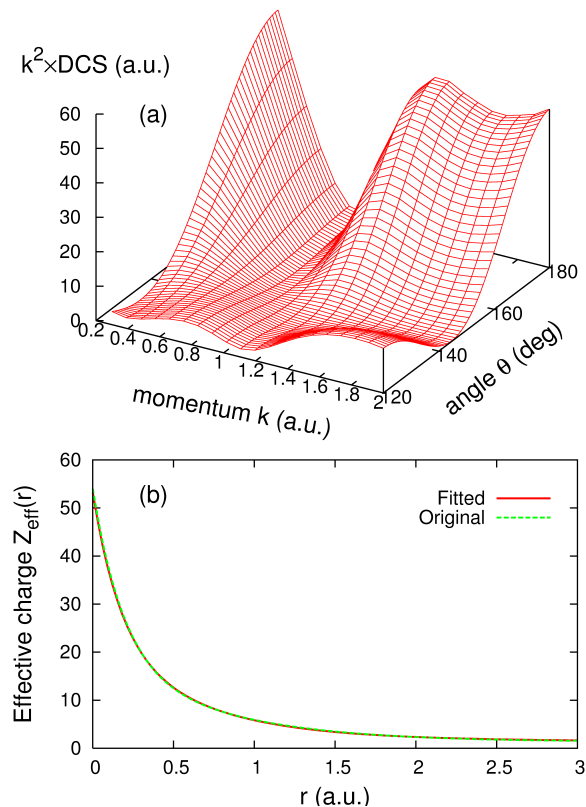
Figure 2.3: *(a) Weighted DCS of Xe for $k \in [0.3, 2.0]$ and $\theta \in [120°, 180°]$. (b) Comparison of the fitted and the original effective charge $Z_{eff}(r)$.*

now close to $Z=18$ used in the input.

We have tested GA for other rare gas atoms such as Ne, Kr and Xe, and similar results have been obtained. As an example, the "experimental" DCS for Xe are shown in Figure 2.3(a) and the retrieved potential is shown in Figure 2.3(b), which is in good agreement with the input potential.

2.3 GA Fitting with Elastic DCS Generated from R-Matrix Calculation

In this section, we will use the elastic DCS calculated with RMAT method as "experimental" data. Different from the previous section, in RMAT calculations no input potential is available and all the electrons are considered in the DCS calculation. To make the simula-

tion more "realistic", we assume that experimentally only the relative DCS are provided, thus we arbitrarily multiply the calculated DCS by a factor of 10. We further introduce "experimental" errors of no more than 10% using a random number generator and "instrumental" angular resolution $\Delta\theta = 5°$ (i.e., convolute the data with a 5° wide Gaussian filter) on the data. The angular range is taken between 100° and 180° and k is chosen in the range of [0.4, 2.0] at 21 equally spaced points.

Because the theory calculates absolute DCS, while the experiment gives only the relative values, the fitness function now is modified to

$$\chi^2(\boldsymbol{a}) = \sum_{i,j} k_i^4 [f \times \sigma(k_i, \theta_j; \boldsymbol{a}) - \sigma_e(k_i, \theta_j)]^2. \tag{2.8}$$

The factor f is determined by,

$$f = \frac{\sum_{i,j} k_i^4 \sigma(k_i, \theta_j; \boldsymbol{a}) \sigma_e(k_i, \theta_j)}{\sum_{i,j} k_i^4 [\sigma(k_i, \theta_j; \boldsymbol{a})]^2}, \tag{2.9}$$

which corresponds to the minimum of $\chi^2(\boldsymbol{a})$ in Eq. 2.8.

In Figure 2.4 the DCS surfaces for Kr, Ar and Ne obtained from the RMAT calculations are shown. They actually are quite close to those generated from model potentials used in the previous section (but we assume that is not known). With GA setup of $N_{pop} = 5$ and $G_{max} = 6400$, the fitting process went through very smoothly, and the fitted model potentials are given in Figure 2.5. In this figure, we also show the model potentials obtained from the paper by Tong et al.[105]. Note that for the latter, the model potential is fitted with the energy of the ground state as well as a few excited states. From GA, the extracted nuclear charges are 9.5, 16.7 and 35.2, for Ne, Ar and Kr, respectively. As noted earlier, more accurate nuclear charges can be obtained if DCS at higher energies are used.

Without the $V(r)$ to check the accuracy, one can compare the energy levels calculated from the retrieved $V(r)$ with their expectation values calculated from the experimental spectroscopy data on NIST webpage[106]. This is shown in Table 2.1. We note that the agreement is good. For the excited states, the error is typically better than 5%, with larger error for the ground state. The larger error for the ground state is not surprising. To begin
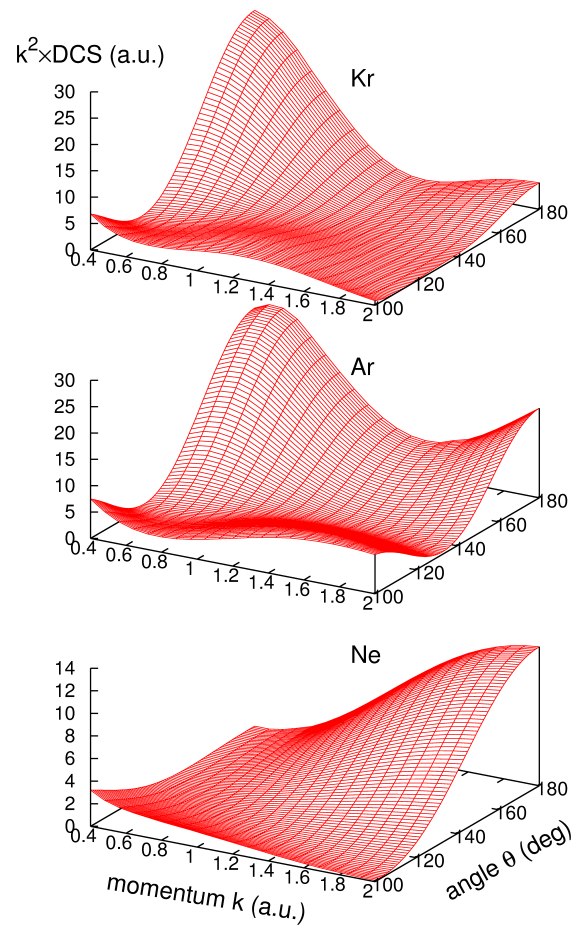
Figure 2.4: *Weighted DCS calculated with RMAT method for Ne, Ar, Kr for momentum $k \in [0.4, 2.0]$ and angle $\theta \in [100°, 180°]$.*
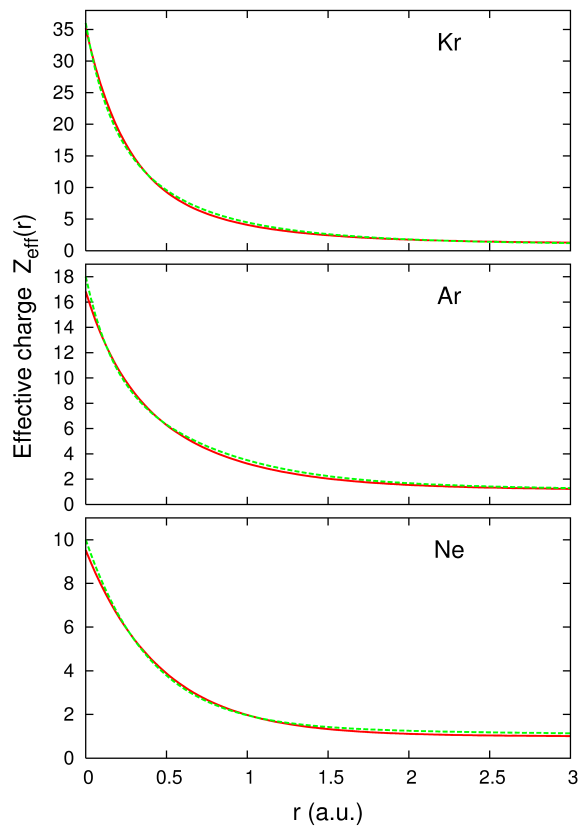
Figure 2.5: *Fitted effective charge $Z_{eff}(r)$ (solid red line) by using the data shown in Figure 2.4 for Ne, Ar, Kr respectively. For comparison, effective charges (dashed green line) from the model potentials in the paper by Tong et al.[105] are also plotted.*

	Configuration	NIST	GA
	$2s^2 2p^6$	-0.792482	-0.832242(5.02%)
	$2s^2 2p^5 3s$	-0.178868	-0.170281(4.80%)
Ne	$2s^2 2p^5 3p$	-0.108140	-0.106876(1.17%)
	$2s^2 2p^5 4s$	-0.068261	-0.067332(1.36%)
	$2s^2 2p^5 4p$	-0.048987	-0.049522(1.09%)
	$2s^2 2p^5 5s$	-0.035578	-0.035754(0.49%)
	$3s^2 3p^6$	-0.579155	-0.467188(19.33%)
	$3s^2 3p^5 4s$	-0.150964	-0.150609(0.23%)
Ar	$3s^2 3p^5 4p$	-0.095147	-0.098672(3.70%)
	$3s^2 3p^5 5s$	-0.061856	-0.060740(1.80%)
	$3s^2 3p^5 5p$	-0.043744	-0.045780(4.65%)
	$3s^2 3p^5 6s$	-0.033707	-0.032724(2.92%)
	$4s^2 4p^6$	-0.514476	-0.464244(9.76%)
	$4s^2 4p^5 5s$	-0.140347	-0.143238(2.06%)
Kr	$4s^2 4p^5 5p$	-0.093071	-0.092664(0.44%)
	$4s^2 4p^5 6s$	-0.060086	-0.058833(2.08%)
	$4s^2 4p^5 6p$	-0.044650	-0.044134(1.16%)
	$4s^2 4p^5 7s$	-0.032900	-0.031910(3.01%)

Table 2.1: *Comparison of the energy levels (in a.u.) from experiments and from the fitted potentials for Ne, Ar and Kr. Error ratios are also shown in percentage. The experimental levels are calculated by using term average.*

with, we already know that the potential near the nucleus is not as well retrieved using the set of "experimental" DCS data in this simulation. Furthermore, the fitness function is for the DCS only.

Despite of the success shown above, one should not come away with the impression that GA always works so well. Using the DCS calculated from RMAT approach for Xe, as shown in Figure 2.6(a), we retrieved the effective charge $Z_{eff}(r)$, showing results from the two with the best fitness. It is clear that the one with the best fitness is incorrect since it would give a nuclear charge close to 90. The second best fit actually results in model potential that is closer to the correct answer. On the other hand, this example also teaches us a lesson on the importance of our "prior" knowledge imposed about the target. As mentioned earlier in this chapter, there is no a unique solution in general to a inverse problem, but additional constraints will be useful to sort out the acceptable solutions. In the current case, we also narrowed down the searching space of Z from [1, 118] to [1,70] which covers almost all of atoms we commonly use in experiments, and the best fit turns out to be the correct one.

2.4   Summary and Outlook

In this chapter the collision between an atomic ion with electrons is treated as the scattering of electrons from a model potential. By expressing the atomic potential in the form of Eq. 2.1 with six parameters, and assuming that elastic differential scattering cross sections are available "experimentally" over a range of energies and angles, we set to find the six parameters using the genetic algorithm. The input "experimental" data were obtained theoretically from another input potential, or from R-matrix calculations, assuming that only the relative cross sections are available and that there are in general a 10% intrinsic random errors and 5° angular resolution in the data. We found that the atomic potential retrieved using GA is quite accurate, as also evidenced by the fact that the retrieved potential reproduces experimental binding energies accurately. We emphasize that DCS from back scattered electrons are used, and electron energies of a few to a few tens of electron volts,
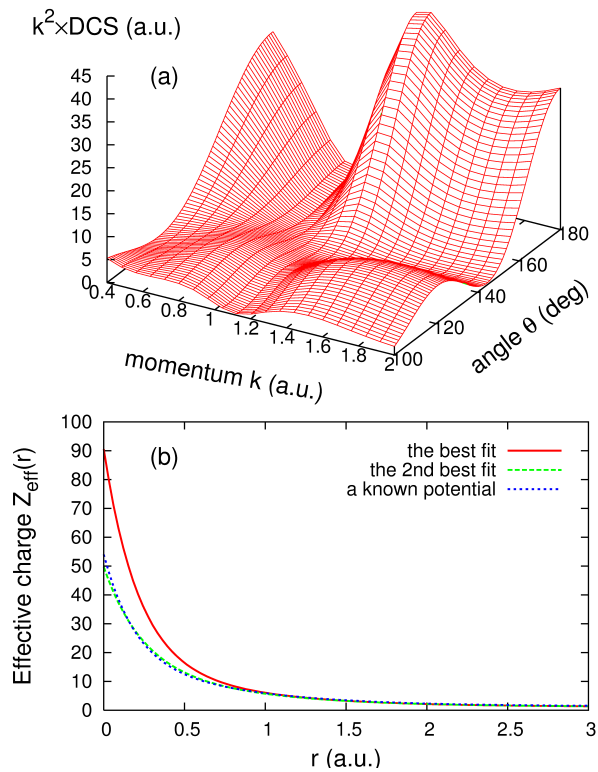
Figure 2.6: *(a) Weighted DCS of Xe with the same range as in Figure 2.4; (b) Fitted effective charge $Z_{eff}(r)$. In (b), $Z_{eff}(r)$ of the two best fits are shown. Note that the best fit actually is incorrect. The second best fit agrees well with the known model potential in the paper by Tong et al.[105].*

28

as these are the typical returning electron energies when infrared lasers are used in laser-atom and laser-molecule interactions, in contrast to the standard electron diffraction method where the electrons are in the hundreds of keV's and the scattering angles are in the forward directions.

Our ultimate goal is to retrieve structure of a transient molecule using high-energy above-threshold-ionization electrons generated by few-cycle laser pulses where the laser duration is of a few femtoseconds[107]. According to the quantitative rescattering theory, it is possible to extract accurate DCS from the momentum distributions of the HATI electrons. Using a pump laser to initiate a transition, the HATI electron momentum spectra can be measured with another few-cycle probe laser pulse. As shown in Chen et al.[77], for this purpose the phase stabilization of the laser pulse is not needed. Our next goal is to generate DCS from fixed-in-space molecules, or molecules that are partially aligned or oriented and test the GA method to extract the structure of the molecule. Experimental HATI electron momentum spectra from isotropically[93,108,109] or partially aligned molecules[65,110] are beginning to emerge in many laboratories. The success of the method presented in this chapter convinces us that GA may be used to retrieve the structure, i.e., the bond lengths and bond angles of a transient molecule, with temporal resolution of a few femtoseconds.

Chapter 3

Molecular Imaging: Independent Atom Model and Mid-IR Lasers*

Dynamic imaging of molecules has been one of the ultimate goals of molecular physics and chemistry[44,111]. Two conventional tools, X-ray and electron diffraction methods routinely achieve sub-Angstrom spatial resolutions but are limited to probing dynamical timescales longer than a picosecond[12]. Since the advent of femtosecond intense infared laser, an alternative method, laser-induced electron diffraction has emerged in last decade. The ultrashort duration of the laser pulses is greatly beneficial for using LIED studying dynamics on femtosecond timescales. However, can laser induced electron diffraction be used to reveal the structure of a molecule? In this chapter, we show that if mid-IR lasers are used, the images generated by the returning electrons are similar to images observed in typical gas phase electron diffraction. These spectra can be used to retrieve the positions of atoms in a molecule as in GED. In Sec. 3.1 we describe the theoretical basis that makes dynamic imaging with infrared lasers possible. In particular, the independent atom model is described which has been widely used in GED. The returning electron energies in LIED are often about 2-3 order of magnitude lower than that in GED. We point out that using Mid-IR lasers, rescattering

---

*Major part of this chapter is reprinted with permission from "Self-imaging of molecules from diffraction spectra by laser-induced rescattering electrons" by Junliang Xu el al.[96], 2010, Phys. Rev. A, **82**, 023814. Minor part of this chapter is reprinted with permission from the supplementary information of "Imaging ultrafast molecular dynamics with laser-induced electron diffraction" by Cosmin I. Blaga and Junliang Xu el al.[68], 2012, Nature, **483**, 194-197. See the text for details. For the copyright permission, please see Appendix A.

electrons energy can be increased to about 100 eV and backscattered electrons could obtain a momentum transfer q comparable to that in GED, promising the feasibility of IAM to accurately describe the backscattering DCSs. The validity of IAM is further examined in Sec. 3.2. We first demonstrate that IAM can be applied to describe diffraction images for incident electron energies down to about 100 eV if the images are taken at large scattering angles. We then illustrate how to retrieve interatomic separations for isotropically distributed molecules as well as for molecules that are aligned. The material in this chapter is an adaption of a published paper in Phys. Rev. A. by Xu. et al.[98], except for the bond-length retrieval of N_2 molecule in Sec. 3.2.1, which is adapted from the supplementary material of a published paper in Nature, which is a joint work between Lin's Group and Agostini-DiMauro's group[68].

3.1 Theory of Dynamic Imaging with Infrared Lasers

3.1.1 Independent atom model for e-molecule collisions

In traditional gas-phase electron diffraction, a beam of electrons with energies of a few hundreds keV's are aimed at randomly distributed molecules. The scattered electrons are measured in the forward directions. The DCS, or the diffraction images, are calculated using the independent atom model[23,112,113]. In IAM, a molecule is modeled as a collection of its component atoms fixed in space. The potential seen by the incident electron is taken to be the sum of the individual potential from each atom. These atoms do not interact and there is no consideration of chemical bonding, nor of molecular orbitals. Let atom i be fixed at $\boldsymbol{R}_i$. The interaction potential of each atom i is represented by a short-range potential. If f_i is the complex scattering amplitude of the ith atom by the incident electron, according to IAM, the total scattering amplitude for a molecule fixed in space is given by

$$F(k, \theta, \varphi; \Omega_L) = \sum_i f_i e^{i\boldsymbol{q}\cdot\boldsymbol{R}_i}, \tag{3.1}$$

where Ω_L denotes the orientation/alignment angles of the molecule, and $\boldsymbol{q} = \boldsymbol{k} - \boldsymbol{k}_0$ is the momentum transfer. The incident electron momentum $\boldsymbol{k}_0$ is taken to be along the z-axis, and $\boldsymbol{k} = (k, \theta, \varphi)$ is the momentum of the scattered electrons. From Eq. 3.1, the differential cross section is then given by

$$I_{\text{tot}}(\theta, \varphi; \Omega_L) = I_A + \sum_{i \neq j} f_i f_j^* e^{i\boldsymbol{q} \cdot \boldsymbol{R}_{ij}}, \tag{3.2}$$

where $\boldsymbol{R}_{ij} = \boldsymbol{R}_i - \boldsymbol{R}_j$, and $I_A = \sum_i |f_i|^2$. Here I_A is an incoherent sum of scattering cross sections from all the atoms in the molecule. The second term is defined to be the molecular interference term (MIT). We can see that molecular structural information is only included in the second term, MIT. For electron scattering from a sample of randomly distributed molecules, the average of the above expression over Ω_L gives

$$\langle I_{\text{tot}} \rangle(\theta) = I_A + \sum_{i \neq j} f_i f_j^* \frac{\sin(q R_{ij})}{q R_{ij}} \tag{3.3}$$

in which q and R_{ij} are the moduli of $\boldsymbol{q}$ and $\boldsymbol{R}_{ij}$, respectively. The IAM equations can be easily derived from the first Born (B1) approximation in scattering theory. In B1, the scattering amplitude is a real number. Since the phase is essential for the interference, and accurate elastic scattering amplitudes from an atomic target are easily obtained, "exact" atomic scattering amplitudes will be used.

Note that the molecular interference term does not vanish after the angular average over Ω_L. This was pointed out early by Cohen and Fano in 1966[114]. From Eq. 3.3, we note that the electron diffraction image obtained from randomly distributed molecules depends only on the magnitude of the interatomic separations. By taking the inverse sine transform of the scattering image, the radial distribution function of the molecule can be obtained[3,23,113]. This is the essential idea behind gas-phase electron diffraction theory.

In GED, there are a few well-known limitations. Since the experimental data can cover only a range of angles, or more precisely, a limited range of q, each peak in the retrieved radial distribution function acquires a width. Thus if several interatomic separations are

nearly identical, they cannot be separated. Second, the diffraction image is obtained from the contributions of all the atoms. For light atoms, they do not deflect high-energy incident electrons significantly. Therefore, the position of light atoms is more difficult to determine in GED. This is also true for X-ray diffraction.

Since the molecular structure parameters (meaning bond lengths, bond angles and/or torsion angles) are determined from the molecular interference term, we can define a molecular contrast factor (MCF)

$$\gamma = \frac{1}{I_A} \sum_{i \neq j} f_i f_j^* \frac{\sin(qR_{ij})}{qR_{ij}}. \tag{3.4}$$

The value and the number of oscillations in MCF will determine the quality of the retrieved molecular structure parameters. Clearly the oscillations are determined by the parameters qR_{ij}. In typical GED[3,23], q takes the range of 1 to 30 Å^{-1}, but others[49] take as small as 2.2 to about 10 Å^{-1}. For small q, the IAM is not expected to work since effect of chemical bonding will come into play. For large q, especially for higher energies, the scattering is too weak. This points out that there is no need to use electrons with energies as high as hundred keV's as in GED in principle. One can obtain the same range of q using lower electron energies, but for large scattering angles. For typical GED, there is no obstacle to go to higher energies. In fact, a high energy electron is easier to manipulate and it has smaller de Broglie wavelength. However, to make short pulses out of high-energy electron beams would be much more of a challenge.

As indicated in the Chapter 1 and Chapter 2, our goal here is to obtain diffraction images using the returning electrons generated by a laser pulse. To get a large q for low energy incident electrons, the scattering angle θ should be large. These are exactly the processes how HATI electrons are generated.

In Figure 3.1(a), we depict the relation between the classical impact parameter and scattering angle for different incident electron energies, using neutral carbon atom target as an example. We define that an electron can "see" the carbon atom center when the impact parameter is less than 0.5 a.u. The upper shaded area defines the angular range
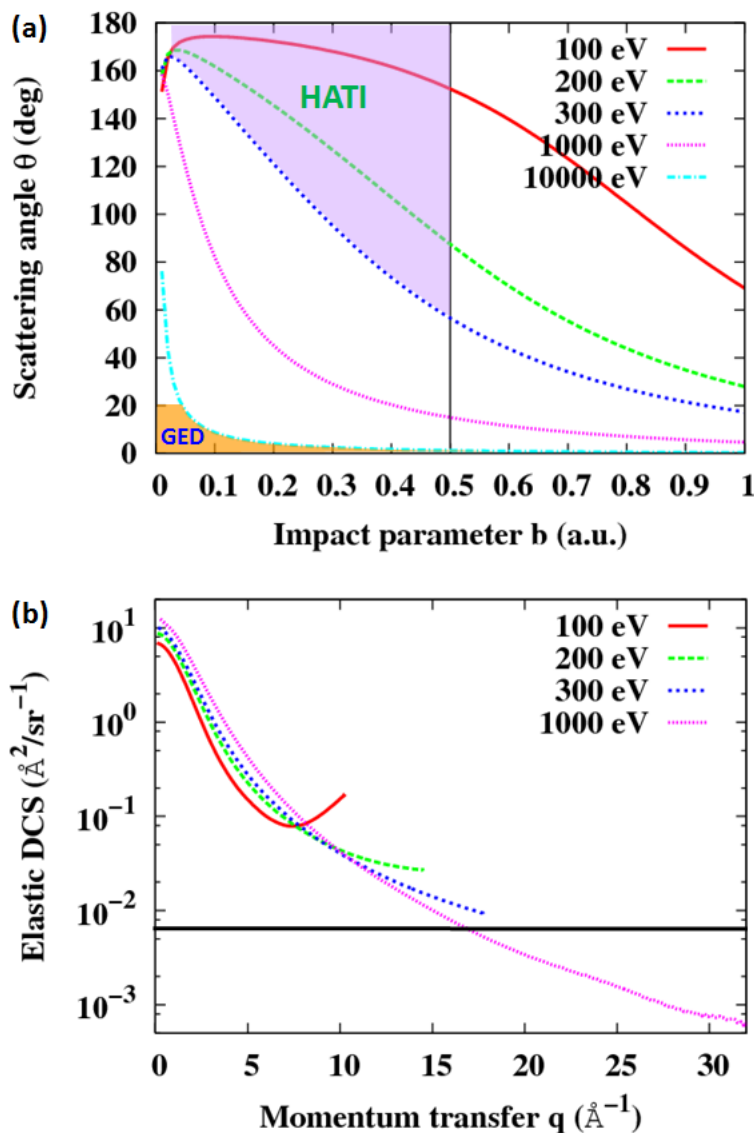
Figure 3.1: *(a) Relation between classical impact parameter b and scattering angle θ for an electron scattered by the potential of a carbon atom. Different curves for incident energies from 100 eV to 10 keV are shown. The vertical line is used to "define" close collisions. The region in scattering angles where GED and HATI spectra can be used for electron diffraction studies are indicated. (b) Differential cross sections against momentum transfer q for carbon atom at different incident energies. For small q, the DCS's depend on q only. For large q, the DCS's depend on q and on incident energy. The horizontal line is drawn to indicate the limit where the DCS's can be conveniently measured.*

for incident electron energies from 100 eV to 300 eV where the IAM can describe the DCS adequately. To the right of the vertical line, the effect of chemical bonding as well as many-electron correlation effect are expected to play important roles in electron scattering, thus the simple IAM does not work. In actual measurements, the magnitude of the DCS is also important. In Figure 3.1(b) the DCS is plotted against the momentum transfer q. Note that to first order, the DCS depends on q only, not on electron energies. If we set the lower limit where DCS can be measured is above the horizontal line shown in the figure, or to q at about 16 Å^{-1}, then the DCS for higher q will be too small. For example, for 10 keV electrons, 20° is about the largest angle where DCS can be used for structure retrieval.

If we take the maximum q at 16 Å^{-1} in Figure 3.1(b) to be the lower limit where diffraction image can be taken, then we can define the region in Figure 3.1(a) where IAM will work for collision energies between 100 and 300 eV and the region for GED when the energy is above 10 keV. In GED it occupies the lower left portion of this allowed region, while for HATI it is in the upper right corner region. Diffraction images taken outside of this shaded region are not useful: either the signal is too weak, or that many-electron as well as chemical bonding will affect the images and they would be too difficult for structure retrieval. In Section 3.2. A the validity of IAM will be examined for collision energies near 100 eV. If the IAM works, then the same method used in GED can be used for diffraction images taken at the lower incident energies.

3.1.2 Extracted DCSs, ionization rate and alignment distribution

The basic idea of using infrared lasers for imaging the structure of a molecule is same as that for atoms. Using the QRS theory[13,77], we have been able to demonstrate that the photoelectron angular distributions $D(k, \theta)$ can be expressed as

$$D(k, \theta) = W(k_r)\sigma(k_r, \theta_r). \tag{3.5}$$

We can extract e-molecular-ion collision cross section $\sigma(k_r, \theta_r)$, and retrieve the molecular structural parameters from it. For a fixed-in-space molecule in a linearly polarized laser

pulse, the HATI spectra depends on the polar angle as well as the azimuthal angle. Since gas-phase molecules are either isotropically distributed or only partially aligned or oriented, the HATI spectra obtained should include such average. In Eq. 3.5, the magnitude of the wave packet depends on the tunneling ionization rate, which in turn depends on the orientation/alignment of the molecules. Thus the electron diffraction images extracted from HATI spectra should be weighted by tunneling ionization rates. For isotropically distributed molecules this is

$$
\begin{aligned}
\langle I_{\text{tot}}\rangle(\theta) = (\sum_i |f_i|^2) \int N(\Omega_L)d\Omega_L \\
+ \sum_{i\neq j} f_i f_j^* \int e^{i\boldsymbol{q}\cdot\boldsymbol{R}_{ij}} N(\Omega_L)d\Omega_L,
\end{aligned}
\tag{3.6}
$$

where $N(\Omega_L)$ are the tunneling ionization rates calculated using the MO-ADK theory[115–117], and Ω_L is the orientation/alignment angles with respect to the polarization direction of the laser beam, same as in Eq. 3.1. A corresponding molecular contrast factor can also be defined using

$$
\gamma = \frac{\sum_{i\neq j} f_i f_j^* \int e^{i\boldsymbol{q}\cdot\boldsymbol{R}_{ij}} N(\Omega_L)d\Omega_L}{(\sum_i |f_i|^2)\int N(\Omega_L)d\Omega_L}
\tag{3.7}
$$

If the molecules are partially oriented or aligned, clearly the angular distribution should be included in the integral over Ω_L.

3.1.3   Structural retrieval using genetic algorithm

In Section 3.2, with the diffraction images from electron collisions with molecules, or from the HATI spectra, we also conducted several retrieval tests using the Genetic Algorithm. The GA driver, GA v1.7a, was implemented by David Carroll[100] with Fortran language, which has both Simple GA and micro-GA options. We actually used micro-GA[98], which evolves small populations (typically 4~10 individuals).

In our approach, a Z-matrix is chosen to build up the geometry of an isolated candidate molecule, which consists of bond lengths, bond angles, and torsion angles. These structural variables, named by $\boldsymbol{X}$, form a search space (parametric space). In general, a molecule,

especially a N-atom nonlinear molecule has $3N - 6$ degrees of freedom. The fitness function $\chi^2(\boldsymbol{X})$ is defined by the least squares of the difference between the experimental data and the calculated DCS with trial structural parameter set, but since the experimental DCS doesn't have absolute values, a scaling factor is needed to bring it onto the same scale as theoretical DCS[98]. The fittest candidate geometry is the one which gives lowest χ^2 value (meaning best agreement with experimental diffraction image).

Micro-GA starts an evolution with an initial population, which are randomly picked up from the parametric space, and the fitness value of each individual then is calculated, giving an evaluation of the quality of each trial structure. In the next step, parents are selected according to their fitness values, and micro-GA always bias the fitter candidates, which is the so-called "survival of the fittest". Uniform crossover operator is then applied to each pair of two mates to produce new generations. Crossover procedure is performed on the basis of binary encodings instead of real-valued encodings, and each bit in the binary representation of each parametric set represents a gene. Elitism is also applied to retain the current fittest structure in the next generation, which is expected to efficiently wipe out the negative effect of crossover. Once a new generation is created, micro-GA starts another evolution loop with it as the parent generation. This will go on up to some preset number of generations. It ends with output of the best geometry. Since micro-GA evolves with small population, premature convergence can happen easily, i.e., different individuals converge to an identical local minimum. To prevent this, micro-GA will check the similarity of the whole population for each generation, by comparing the genes of the current best fit with the other individuals locus by locus. If the number of non-identical bits is less than 5% of the total bit number, micro-GA will restart with the best fit and randomize the rest. More details may be found in Chapter 2 and also the paper by Xu et al.[98]. This method has been used to reconstruct atoms[98,118,119] from the atomic DCS's at large angles.

	Z	λ (a.u.)
H	1	0.881
Li	3	0.774
C	6	1.276
N	7	1.695
O	8	1.720
F	9	1.902

Table 3.1: *Parameters in Yukawa potential $V(r) = -Ze^{\lambda r}/r$ for selected atoms. The nuclear charge Z and a damping factor λ are listed.*

3.2   Results and Discussion

3.2.1   Electron-molecule scattering and IAM model for isotropically distributed molecules

CO_2

We first check how well the IAM works for electron collisions with neutral molecules. Consider electron collisions with CO_2 targets for incident energies of 20, 50, 100 and 200 eV. In Figure 3.2 are shown the IAM results compared with the experimental data taken from Register et al.[120], Iga et al.[121], Kanik et al.[122], and Tanaka et al.[123]. Only data for large angles are shown. In the IAM calculations, the interaction potential between the incident electron with the carbon atom is approximated by a Yukawa potential with the parameter λ listed in Table 3.1. The λ for other atoms used in this article are also given in this Table. It is chosen such that the ground state energy of the negative ion calculated has best agreement with the experimental data[124]. The calculation of the scattering amplitude for each atom can be found in standard quantum mechanics textbook, e.g.,[125], or in Section II.D of[77]. In the IAM simulation, the bond lengths are taken from the experimental data. From Figure 3.2, it is clear that IAM does not give a good description of the DCS for collisions below 50 eV. At 100 eV and higher, the agreement becomes quite good. In the covered energy region, the DCS becomes larger at large angles, with a pronounced broad minimum. This broad minimum is due to the diffraction from individual atoms. This is different from collisions at
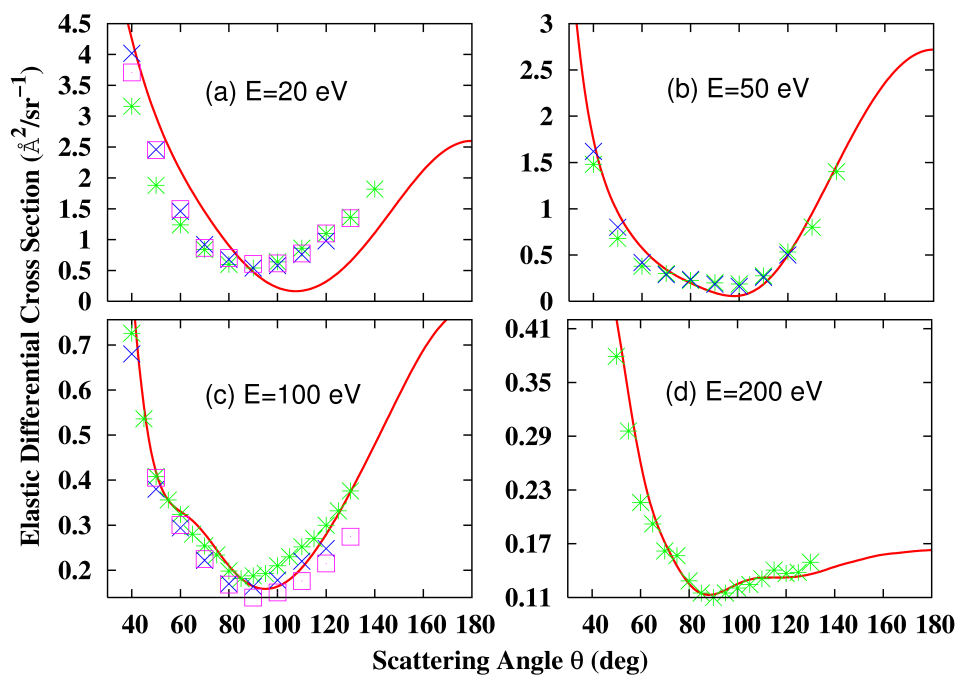
Figure 3.2: *Elastic differential cross sections for e^--CO_2 collisions at incident energies of 20 eV, 50 eV, 100 eV, and 200 eV. Solid red curves are IAM simulation. Symbols are experimental data from different groups. Asterisks: (a,b) from Register et al.[120], (c,d) from Iga et al.[121]; crosses: from Kanik et al.[122]; empty squares: from Tanaka et al.[123].*
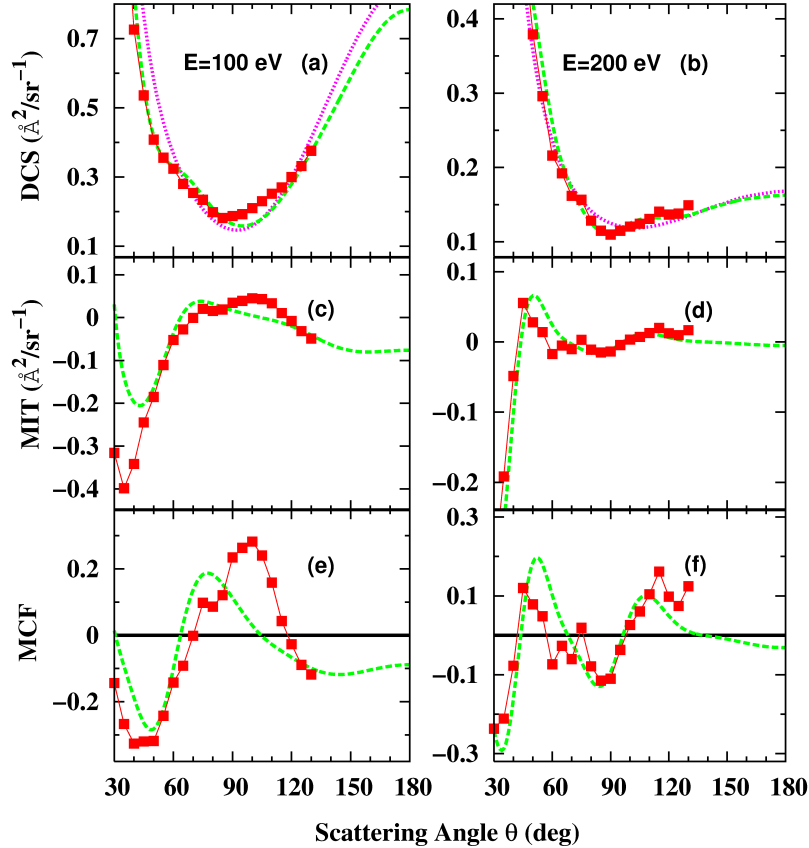
Figure 3.3: *(a,b) Experimental (red solid squares) and theoretical (dashed green curves) DCS's vs the atomic terms (dotted pink curves). (c,d) molecular interference terms, comparing experimental data with IAM. (e,f) Same as (c,d) but for molecular contrast factors.*

the hundreds of keV's used in GED where the DCS decreases monotonically at large angles.

In Figure 3.2, there is no clear evidence of molecular interference in the experimental DCS. In Figures 3.3(a,b) we display the same experimental DCS from Iga et. al.[121] and compare to the atomic term, for collision energies of 100 and 200 eV's. One can see that the IAM predictions and the experimental data oscillate about the atomic DCS. Recall that these results are for isotropically distributed CO_2. It demonstrates that molecular interference survives the average over the randomly distributed molecules.

To appreciate the difference of the DCS calculated from the simple IAM model with the experimental data, we subtract the atomic DCS and show the difference as the molecular

interference term. For this purpose, we renormalize the experimental data by a multiplicative factor α,

$$I_{\mathrm{MIT}} = \alpha \times I_{\mathrm{tot}}^{\mathrm{exp}} - I_{\mathrm{tot}}^{\mathrm{atom}}. \tag{3.8}$$

Factor α is chosen such that the mean square of the difference between the renormalized experimental data and the atomic DCS is minimum. The resulting molecular interference term from the experimental data and from the IAM are shown in Figures 3.3(c,d). Note that both the IAM and the experimental data show oscillations. There are shifts in the oscillations between the data and the IAM predictions which we take to indicate the inaccuracy of the IAM at these energies. At 200 eV we can see the difference is smaller. This result is expected since IAM is a model built upon the high-energy scattering theory.

We can also display the molecular contrast factor, MCF, see Eq. 3.4, for the experimental data and the IAM prediction, shown in Figures 3.3(e,f). It shows that there is a shift in the oscillations between the data and IAM, more so at 100 eV than at 200 eV. By presenting MCF, it allows us to evaluate the degree of fluctuations in the experimental data. Clearly the last experimental point in Figure 3.3(f) is too high. In practical GED applications, experimental data are often first smoothed[113] before they are used to retrieve the radial distributions of molecules.

C_2F_6

We next consider a more complex molecule like C_2F_6 where elastic differential cross sections for e^--C_2F_6 collisions have been reported by Iga et al.[126]. In Figure 3.4(a) the shape of this molecule is depicted, and values of the molecular interference terms from the experiment and from the IAM are shown at three collision energies of 150, 200 and 300 eV in Figures 3.4(b,c,d). It is interesting to note that for the angular range of 30° to 70° there is a pronounced interference maximum and minimum, respectively, at each energy. At larger angles the molecular interference term is quite flat. At these energies there is a general agreement between the IAM prediction and experiment.
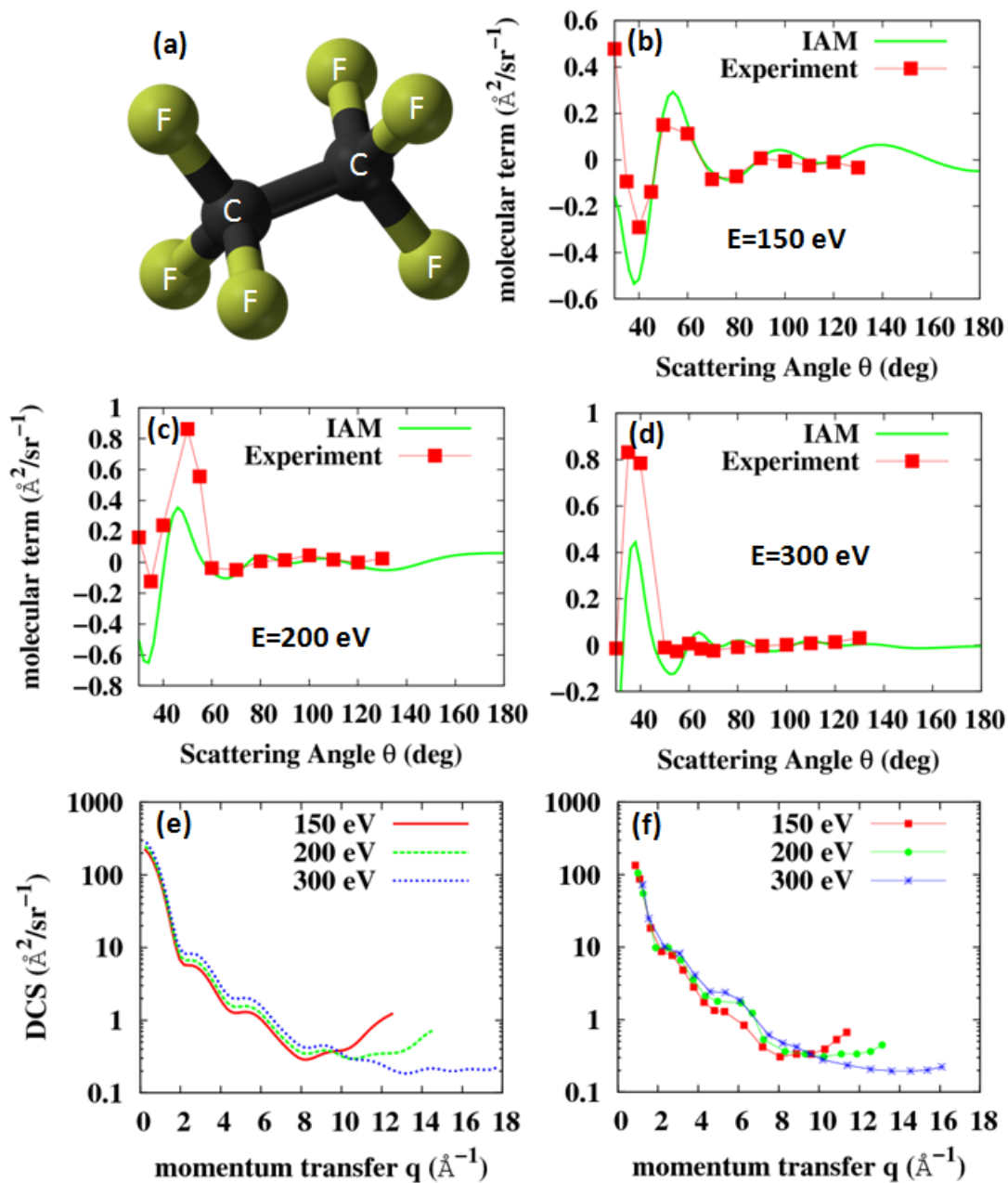
Figure 3.4: *(a) Structure of a hexafluoroethane C_2F_6 molecule in ball-and-stick model. (b,c,d) Molecular interference terms for e^--C_2F_6 collisions, experimental data[126] vs IAM, at incident energies of 150 eV, 200 eV, and 300 eV. Elastic DCS's plotted against momentum transfer q, IAM (e) vs experimental data (f), for the three energies, respectively.*

	C-O bond length (Å)
experiment	1.163
50 eV	1.28(+10%)
100 eV	1.08(−6.7%) [Iga et.al.]
	1.18(+1.5%) [Tanaka et.al.]
	1.10(−5.4%) [Kanik et.al.]
200 eV	1.13(-2.9%)

Table 3.2: *Retrieved C-O bond length of CO_2 from experimental DCS's at 50 eV, 100 eV, and 200 eV, respectively.*

The similarity of the molecular interference term in Figures 3.4(b,c,d) is not surprising. In Figure 3.4(e) we plot the DCS obtained from the IAM in terms of the momentum transfer q for the three energies. One can see that within a range of q, they lie on top of each other. Only at large angles we see deviation from the universal curve. We comment that within the first Born approximation, the DCS depends only on q, not on the scattering energies and angles independently. In Figure 3.4(f) we plot the experimental data against q. It shows that they lie on a universal curve mostly, very similar to the predictions of the IAM.

More tests on the validity of the IAM over the intermediate-energy region were carried out elsewhere, for example in [127–130]. Especially in [130], Iga et al. presented an experimental verification on the applicability of the IAM in the above energy region, with DCS's for acetylene, *n*-butane, and benzene measured.

Retrieval of bond length from the DCS of randomly distributed molecules

In this subsection, we address how much error is introduced on the retrieved interatomic separations if we assume that the experimental DCS is described by the IAM. Note that we use GA for the retrieval instead of the inverse sine transform used in GED. Here we first take the simple example of CO_2. Using the experimental DCS the retrieved C-O bond length is 1.28, 1.08 and 1.13 Å, using experimental data at 50, 100 and 200 eV, respectively, see Table 3.2. Compared to the known bond length of 1.163 Å, the errors are +10%, −6.7% and −2.9%, respectively. These results are consistent with our conclusion we drew in Sec. 3.2.1

that IAM works better for energies above 100 eV. It's worth noting that for the fitting at 100 eV, we used the data from Iga et. al., which actually agrees worst with the IAM prediction than data from Kanik et. al.[122] and Tanaka et. al.[123] (see Figure 3.2). Using the latter two data, the retrieved bond lengths turn out to be more accurate, 1.18 Å and 1.10 Å. The average accuracy is about 5 pm. Such accuracy is inferior to what can be accomplished using GED. Note that there are very few experimental data points used in the retrieval and data at many larger angles are not available. These experimental data were not taken for the purpose of GED, thus there are few data points at large angles. In spite of this, reasonable C-O bond length can already be retrieved. For future dynamic imaging, such errors are acceptable since the goal there is to follow the change of bond length with time, rather than the precise values at a given time.

For another example, we consider N_2. Figure 3.5(a) and (b) show measured DCSs for 100 eV (solid red squares) and 200 eV (solid orange circles) electrons colliding with N_2 at large scattering angles[129]. The e-N interaction is modeled by a Yukawa potential $V(r) = Ze^{-\lambda r}r/r$ with $Z = 7$ and $\lambda = 1.695$, see Table 3.1. Figure 3.5(a) shows the calculated DCS curve (dotted green line) with the known N-N equilibrium bond length, R_{eq}, of 1.10 Å. The atomic term is also shown (blue dashed line). Note that the experimental data and the IAM predictions oscillate about the atomic term. The phase of the oscillation from the IAM model agrees well with the experiment, even though the amplitude shows deviations. A consistency check of our bond length retrieval method is performed by using the same scattering amplitudes and taking the N-N distance as a free parameter to fit the experimental data. This procedure yields a N-N bond length R_{fit} =1.13 Å for 100 eV and 1.09 Å for 200 eV, in very good agreement with the accepted value of 1.10 Å. The resulting DCS curves are also plotted in Figure 3.5(a,b).

Figure 3.5(c) shows the molecular contrast factor calculated via IAM using the two fitted R's from Figure 3.5(a) and (b) (maintaining the same label convention used above). According to Eq. 3.4, for homonuclear diatomic molecules, the two curves should be con-
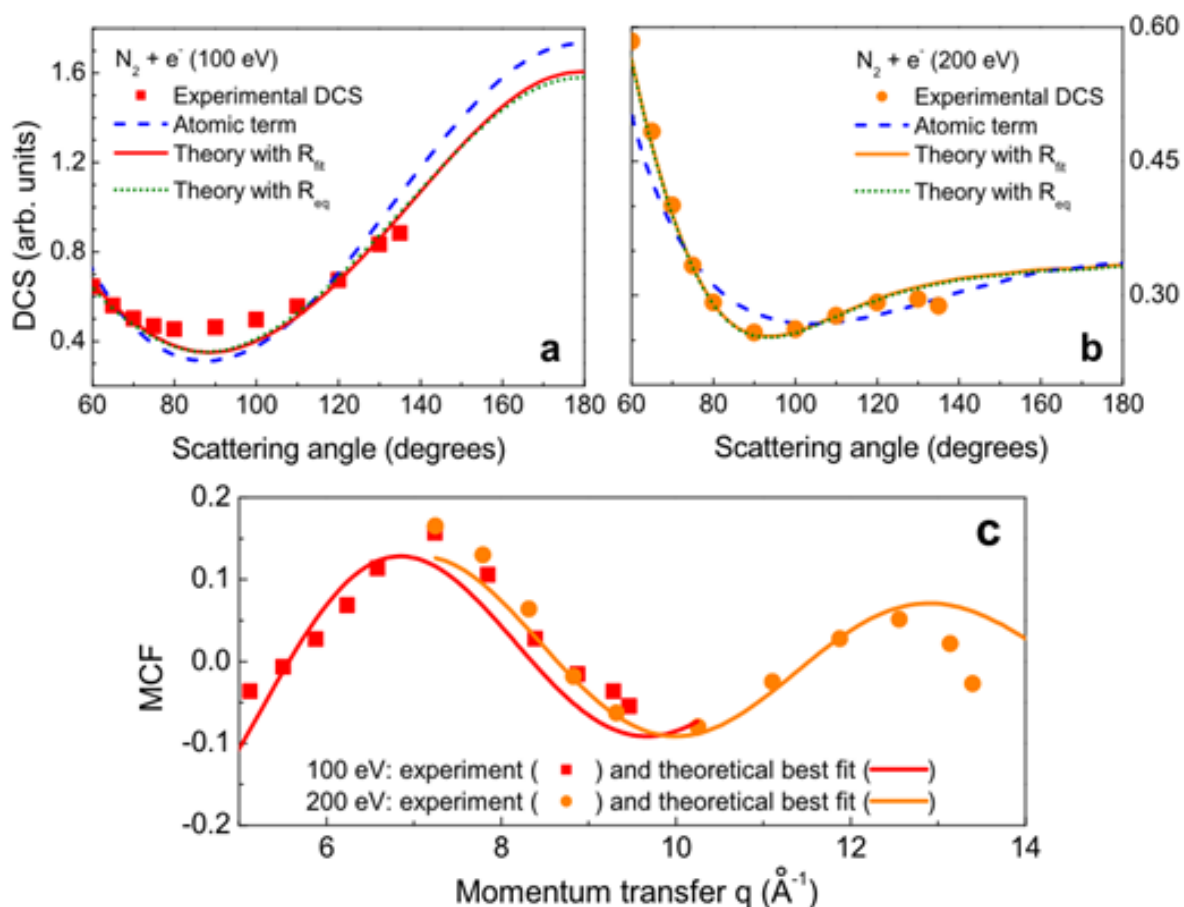
Figure 3.5: *Retrieval of N_2 bond length using experimental molecular collision DCSs. Full solid squares and circles are experimental DCSs from electron-molecule collisions at large angle for incident energy of (a) 100 eV and (b) 200 eV, respectively. They are compared with their corresponding theoretical DCSs (green dotted lines) calculated using IAM with the known equilibrium bond length and the atomic terms (blue dashed lines) are also given. The theoretical DCSs with fitted N-N distances are also shown by the red curve in (a) and the orange curve in (b). In (c), MCF from experimental DCSs in (a) and (b) and their corresponding best fits are plotted against the momentum transfer q. For 100 eV, the experimental MCF curve has been multiplied by 0.3 from the actually calculated ones. Note that scaling does not change the position of the peak of the curve or the values of q where it changes sign. The IAM approximation may not lose accuracy at 100 eV but the global oscillation in the MCF still provides an accurate method for retrieval of the bond distance.*

45
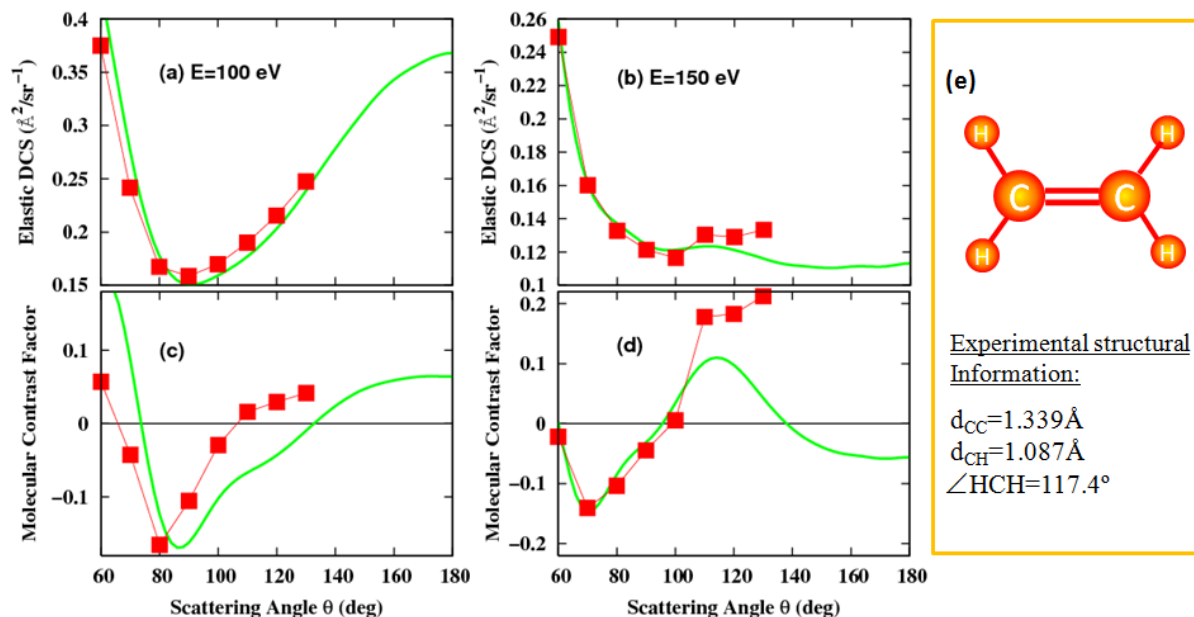
Figure 3.6: *(a,b) Comparison between measured DCS (red solid squares) of C_2H_4 at electron incident energy of 100 and 150 eV's and the IAM simulations (green full lines). (c,d) Comparison of the molecular contrast factors. The known bond lengths and the bond angle are shown in (e).*

tinuous if the derived R's are identical. The 200 eV data does agree well with the IAM curve except the deviations of the last three points, possibly due to the small cross section at large angles. The 100 eV experimental data points have been scaled by 0.3 but this does not affect the peak position or the q-value where the MCF changes sign. Note that the R was fitted from the DCS directly, i.e. without scaling. The MCF shows that the experiment still follows the oscillation in q as predicted by the IAM, even though the magnitude does not. Despite this limitation, the retrieved R is accurate (1.13 Å versus 1.10 Å) and clearly demonstrates that the retrieval method of R is sensitive to the oscillatory behavior of the molecular term and not the magnitude of MCF. This same conclusion can be drawn with respect to Young's double slit experiment where the information on the slit separation is contained in the global oscillation of the fringe pattern and not the fringe luminosity.

We finally consider a complex molecule, ethylene. In Figure 3.6(e) the known structure of C_2H_4, the C=C and C-H bond lengths, and the angle ∠HCH are given. This system is

	C=C length (Å)	C-H length (Å)	∠HCH
experiment	1.339	1.087	117.4°
100 eV	1.436(7%)	1.281(18%)	144.4°
150 eV	1.324(-1%)	1.075(-1%)	105.8°
100 eV	1.058(-21%)	0.947(-13%)	163.7°
150 eV	1.271(-5%)	1.134(4.3%)	109.0°

Table 3.3: *Retrieved structural information of C_2H_4 from experimental DCS's at 100 eV and 150 eV, respectively, compared to the known experimental values. The first set are obtained from fitting the molecular interference term, the second one are from fitting the molecular contrast factor, see Text.*

considered to be a challenge for GED since the DCS from H is much smaller than that from C such that information on H is difficult to retrieve. In Figures 3.6(a,b) we show the DCS data from e^--C_2H_4 collisions for incident energies at 100 eV and 150 eV from Brescansin et al.[131], as well as the prediction of the IAM using the known molecular parameters. The same results are shown in terms of the molecular contrast factors γ in Figures 3.6(c,d). Using the experimental DCS from Figures 3.6(a,b) and GA, we retrieve the molecular parameters and the results are shown in Table 3.3. At 100 eV, the retrieved data have 7% error in the C=C bond length, while the C-H length and the angle ∠HCH have larger errors. However, the retrieved results using the experimental data at 150 eV look very good. Here we use the DCS directly for the fitting. If we use the molecular contrast factors in Figures 3.6(c,d) for the fitting, we obtained the different results as shown in the bottom two rows in Table 3.3. The discrepancies between the two methods are not surprising. The fitness functions in the two approaches are not the same. By fitting the DCS, the fitness function emphasizes small angles where the DCS are larger. Using the MCF, all the angles are treated on equal footing. Thus the error at large angles in Figure 3.6(c) is enhanced in the retrieval.

As mentioned earlier, we used GA to retrieve the molecular structure parameters from the electron diffraction images. It turns out that GA has been suggested recently for molecular structure retrieval for diffraction images taken using GED or UED[132,133]. The global GA search for molecular geometries of a dynamic system is especially powerful since data
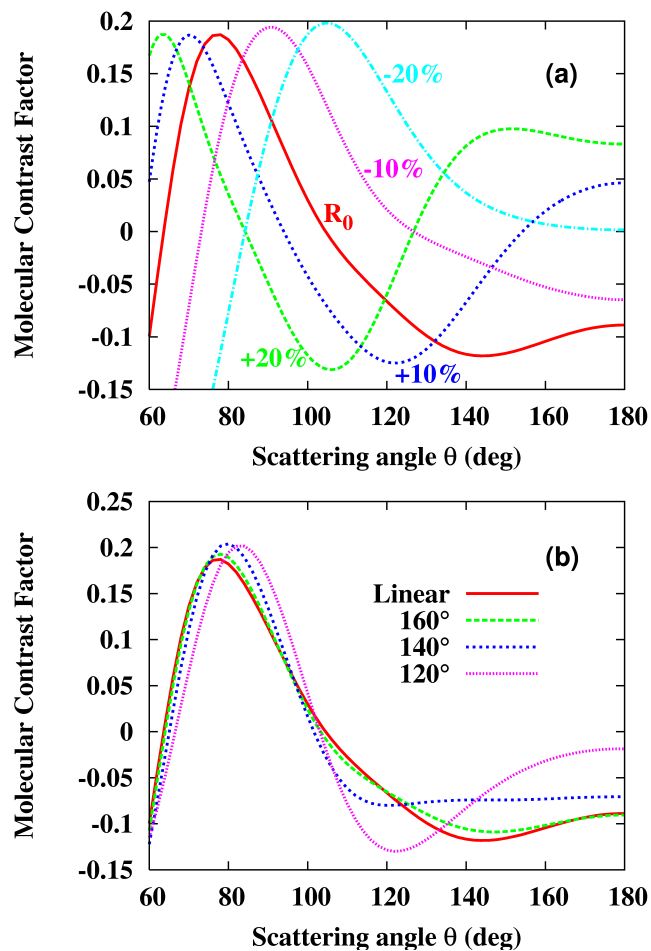
Figure 3.7: *(a) Sensitivity of the molecular contrast factor γ vs the change of C-O bond length for e^- -CO_2 collisions at 100 eV. The bond length has been increased or decreased by 10% and 20% with respect to the equilibrium value, respectively. (b) The same, but for a triangular CO_2, where the bond angle $\angle OCO$ is varied.*

retrieved from an earlier time step can be used to impose constraints on the search space in the next step to achieve faster convergence. By using techniques developed from the larger GED and UED communities, the retrieval of molecular structure from the HATI spectra will be able to proceed significantly faster when experimental data become available.

Dependence of DCS on bond lengths/angles in the molecule

It is interesting to note that electron diffraction image is very sensitive to the interatomic distances for a given molecule, as can be seen in Eq. 3.3 since R_{ij} appears in the phase factor

48

in the IAM. When the positions of the atoms in a molecule change as in a dynamic system, the atomic DCS will remain the same, but the molecular interference term will evolve in time. In Figure 3.7(a) we show how the molecular contrast factor changes when the bond distance between C and O is changed in CO_2. Shown are for electron collisions at 100 eV, and for the C-O length that has been increased or decreased from its normal value by 10% and 20%, respectively. As the bond length increases, the oscillation shifts to smaller angles and the oscillation becomes faster. This is easily understood from the IAM since the phase $\boldsymbol{q} \cdot \boldsymbol{R}_{ij}$ in Eq. 3.3 increases with the bond length.

We have also examined the case where the CO_2 is assumed to be nonlinear, see Figure 3.7(b). We change the bond angle while the C-O bond length is kept fixed. This is equivalent to decreasing the internuclear distance of O-O. The conclusion is the same. When the change of bond length is large, the molecular contrast factor γ changes more rapidly. For large angles, say from 180° to 160°, the change in O-O distance is small and thus γ does not change much. For θ from 140° to 120°, the γ changes much more since the O-O bond length changes more.

3.2.2 Electron-molecule scattering and IAM model for aligned or oriented molecules

Electron diffraction images from molecules aligned in one dimension

The above discussions focused on molecules that are isotropically distributed. If the molecules are oriented or aligned, clearly the diffraction images will have more pronounced interferences. Field-free molecules can be partially aligned or oriented by infrared lasers[134], or by photodissociation[49,53] using linearly polarized lights. For simplicity, here we consider molecules aligned in 1D only. This can be carried out by exposing molecules to a short linearly polarized infrared laser. After the pulse is over, the molecules will change from aligned to anti-aligned (or vice versa) near the time intervals of rotational revivals. In 1D alignment, the molecules are distributed cylindrically symmetric with respect to the polarization axis (the z-axis) of the aligning laser. We consider electron collisions with these
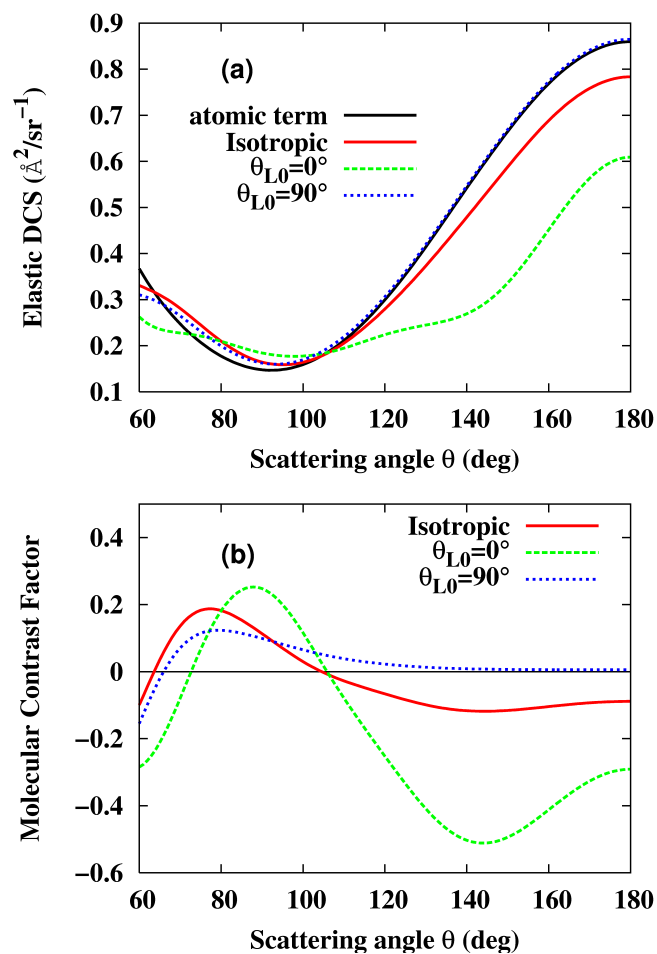
Figure 3.8: *(a) Comparison of DCS's for parallel-aligned, perpendicularly-aligned, and isotropic CO_2 molecules. The atomic term is also shown (barely separable from the 90° curve at large angles). (b) Same data presented in terms of molecular contrast factor.*

aligned molecules, where the incident electrons are directed along the z-axis. In this simple geometry, the DCS depends on the polar angle θ only, not on the azimuthal angle ϕ. We mention that we are not aware of any such measurements yet. For molecules aligned by photodissociation, there have been a few reported so far, with the time resolutions of a few hundred femtoseconds[49,53].

In Figure 3.8(a) we show the calculated DCS for electron collisions with aligned CO_2 molecules at incident energy of 100 eV, for molecules aligned parallel and perpendicular to the z-axis, respectively. We assume that the angular distribution of the molecules has the $\cos^6(\theta_L - \theta_{L0})$ dependence, where θ_L is the angle between the molecular axis and the incoming direction of electron beam, and θ_{L0} is the central angle of the aligned molecules. In this figure, the DCS for the atomic terms only, and the DCS for isotropically distributed molecules are also shown.

From Figure 3.8(a), it is interesting to note that the oscillation is much stronger for parallel-aligned molecules than for the perpendicularly-aligned molecules. This is expected for all linear molecules and can be understood from the IAM. In Eq. 3.3, the phase of the interference term is give by $\boldsymbol{q} \cdot \boldsymbol{R}_{ij}$. For large scattering angles, the momentum transfer vector $\boldsymbol{q}$ is nearly antiparallel to the incident direction. Thus $\boldsymbol{q} \cdot \boldsymbol{R}_{ij}$ is near zero if the molecule is perpendicularly aligned and maximum when it is aligned. This is opposite to GED where the electron is scattered in the forward directions and $\boldsymbol{q}$ is nearly perpendicular to the incident direction. In this limit, more favorable interference is expected when molecules are perpendicularly aligned. Thus for linear molecules, to obtain large molecular contrast, sharper features in the diffraction images are obtained by aligning molecules parallel to the incident electrons if the electron energy below 300 eV and the images are taken in the backward directions. For completeness, in Figure 3.8(b) we show the molecular contrast factor obtained from the DCS shown in Figure 3.8(a).

For another example, we compare the molecular contrast factor for aligned C_2F_6, again assuming the molecules have 1D alignment and have angular distributions given by $\cos^6(\theta_L -$
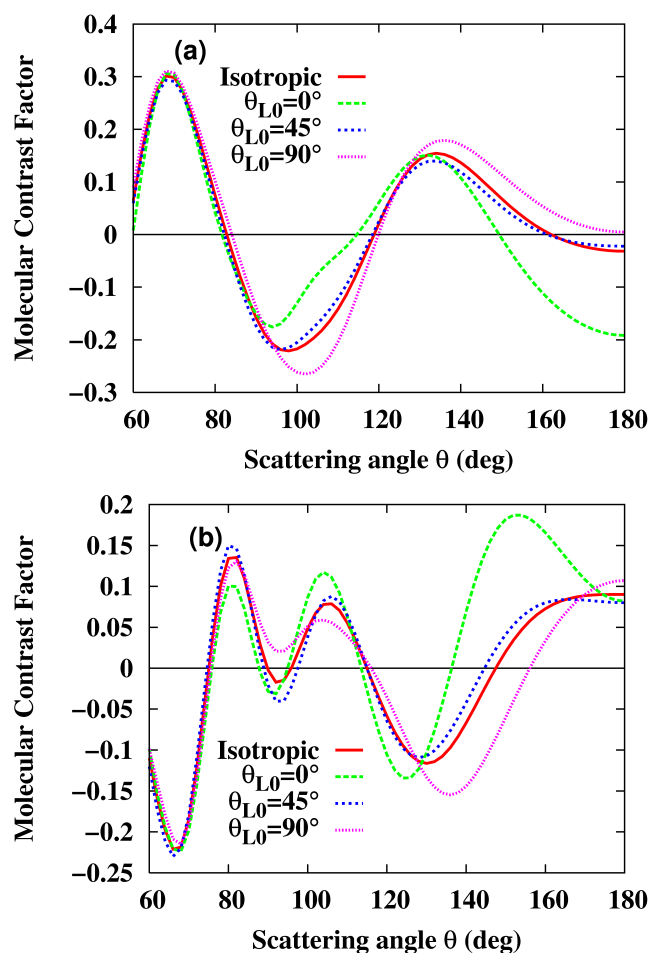
Figure 3.9: *(a) Comparison of molecular contrast factors of C_2F_6 molecules at different alignment conditions for incident energy of 100 eV. (b) Same as in (a) but for 200 eV.*

	ordering	(d_{CI}, θ_I)	(d_{CF}, θ_F)
"real"	IHHFHH	$(2.10\text{Å}, 10.00°)$	$(1.41\text{Å}, 25.00°)$
retrieved	IHHFHH	$(2.10\text{Å}, 9.94°)$	$(1.41\text{Å}, 24.96°)$

Table 3.4: *From the "measured" HATI spectra of 1-fluoro-4iodobenzene, the retrieved parameters using GA are compared to the input parameters.*

θ_{L0}). We consider the alignment axis (the C-C axis) making an angle 0°, 45° and 90°, respectively, with the incident electron beam entering along the z-axis. The IAM is used to calculate the DCS. From the DCS calculated, we extract the molecular contrast factor for the three alignment angles and the isotropic one. The resulting molecular contrast factors versus the scattering angles are shown for scattering energies of 100 eV and 200 eV, in Figures 3.9(a) and 3.9(b), respectively. It is noted that for alignment angle of 45°, the contrast is about the same as the isotropic one. The contrast is still the largest when the molecules are parallel-aligned. Unlike the linear molecules, the contrast for the perpendicularly aligned molecules is no longer small. For this molecule, if the molecule is perpendicularly aligned, the C-C axis is perpendicular to q, but the C-F bond is parallel to q. Comparison of Figures 3.9(a) versus 3.9(b) shows that there are more interference maxima and minima at higher scattering energies.

Retrieving molecular bond lengths (and bond angles) from electron diffraction images of molecules aligned in 3D

So far we have shown that the diffraction images from randomly distributed molecules is very sensitive to the bond lengths of the constituent atoms in the molecule. Clearly the structure retrieval will be significantly improved if diffraction data for aligned/oriented gaseous molecules are available[135].

For simplicity, here we illustrate how the atomic positions in a molecule can be retrieved if the DCS are available from fixed-in-space molecules. In Figure 3.10(a) we construct a fictitious isomerization scenario. For the linear LiCN molecule, we assume that it evolves to CNLi along the (arbitrarily chosen) path indicated in the figure. In the simulation, we
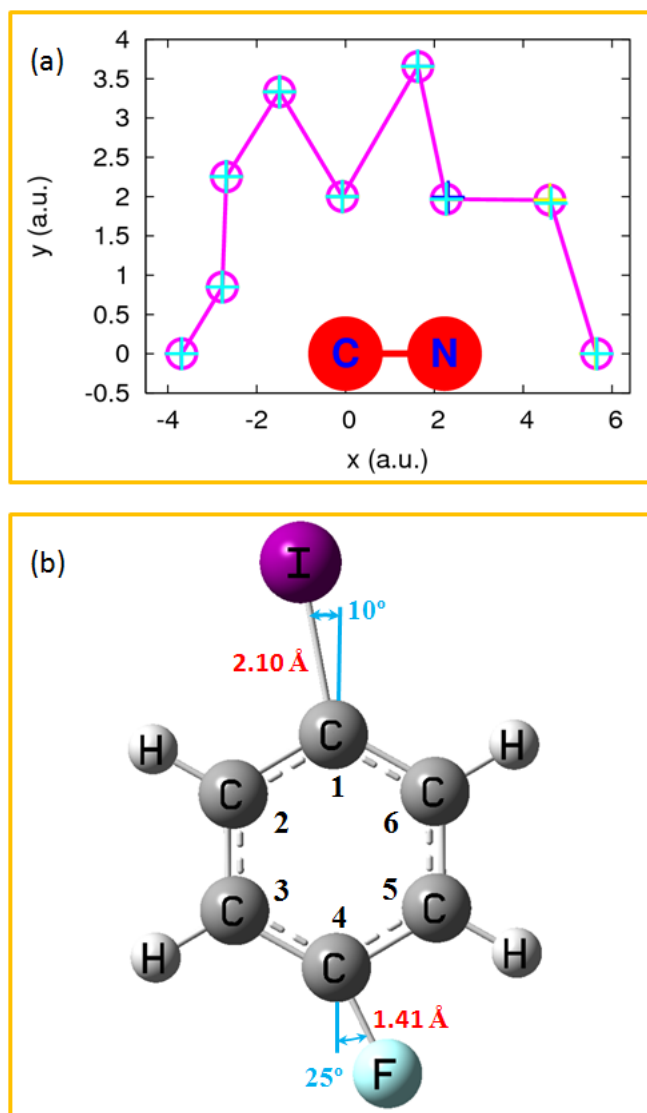
Figure 3.10: *(a) Simulation of the isomerization of LiCN to NCLi. In the model, the plane of the molecule is fixed and laser's polarization is perpendicular to it. The assumed path taken by Li are given by open circles at different steps. From the HATI spectra, the retrieved Li positions from GA are indicated by crosses. (b) A model of 1-fluoro-4-iodobenzene molecule away from its equilibrium configuration. We assume that the iodine and fluorine atoms are at the positions indicated. Laser polarization is perpendicular to the plane. From the "measured" HATI spectra, this molecular geometry is reconstructed, with results shown in Table 3.4.*
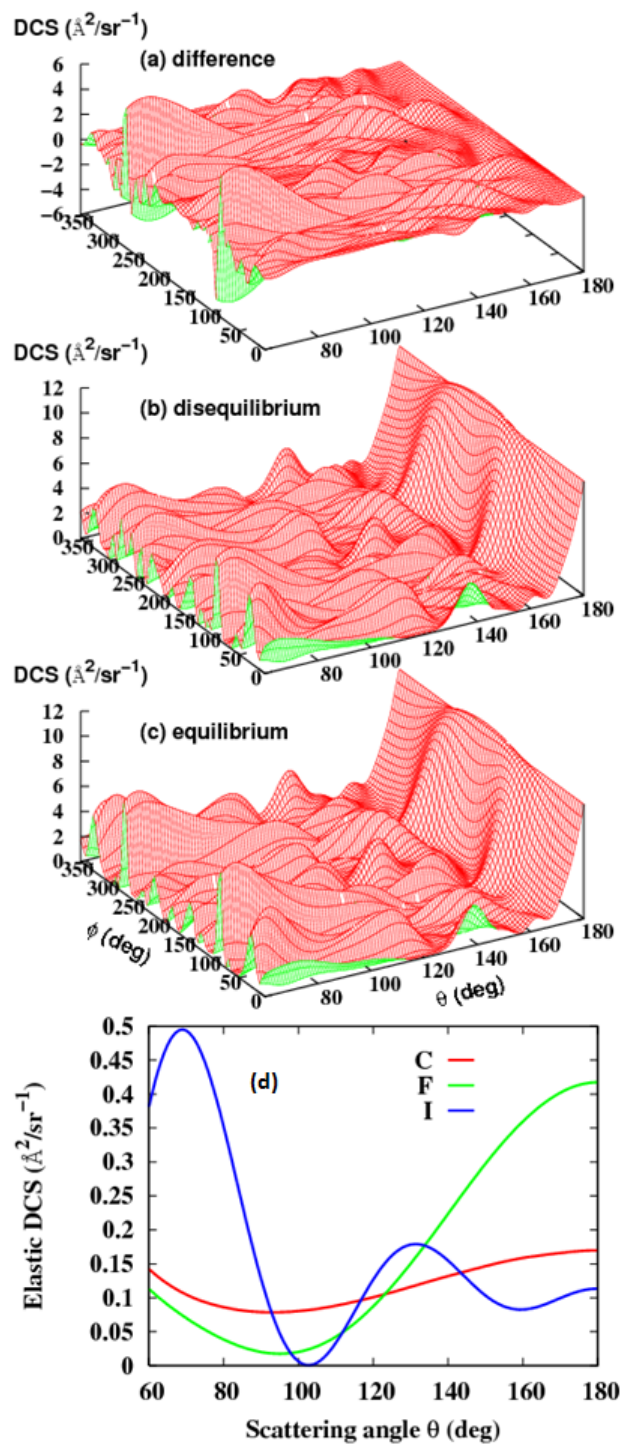
Figure 3.11: *(Color online) (a) The difference of the DCS for electrons colliding with 1-fluoro-4-iodobenzene with I and F atoms at and away from their equilibrium positions. The diffraction spectra for F and I at the non-equilibrium (b) and the equilibrium (c) configurations. (d) Comparison of the differential cross sections for iodine, fluorine and carbon atoms. The electron energy is 200 eV.*

place Li at a new position and restrict it to move only on the plane of the figure[136]. We use IAM to obtain the 2D electron diffraction image for each new position, assuming that the electron beam is perpendicular to the plane. We then introduce a 10% random error to each image data point and treat the results as experimental data. We use GA and the IAM to retrieve the position of Li, i.e., the distance of Li-C and the angle ∠LiCN, with the C-N bond fixed. In Figure 3.10(a), the input position of Li is denoted by the center of each circle, the retrieved position is indicated by the crosses. For this example, retrieval of the position of Li is quite simple.

In another example, we consider a planar 1-fluoro-4-iodobenzene molecule, C_6H_4IF, see Figure 3.10(b), away from its equilibrium configuration. This is a benzene molecule where one of the H's is replaced by fluorine and another replaced by iodine. We will assume that the C-C bond and the C-H bond do not change, but allowing the I and F to change from their normal equilibrium positions as indicated. In the hypothetical experiment, we assume that the incident electrons enter perpendicularly to the plane of the molecule. We use IAM to calculate the DCS (2D spectra), and introduce 10% random errors to each image point and take the results as "experimental" data. In the retrieval, we allow F to switch to a different C site. Here we define the position of the C that is connected to I to be No.1, as indicated in the figure. Using GA, in this example, the search involves five parameters: the two angles and two bond lengths indicated in the figure for I and F, respectively, and the order of the C atom where the fluorine is attached to. From the Table 3.4 we note that the five input parameters are accurately retrieved.

The simulation in Figure 3.10(b) represents a large class of chemical compounds where the hydrogen atoms are replaced by heavy atoms. Since diffraction images from individual heavy atoms are much larger, see Figure 3.11(d), the difference image shown in Figure 3.11(a) is quite large when the positions of heavy atoms are changed. In Figure 3.11(b) the diffraction image taken when F and I are away from their equilibrium positions is compared to Figure 3.11(c) where the F and I are in their normal positions. The simulations were
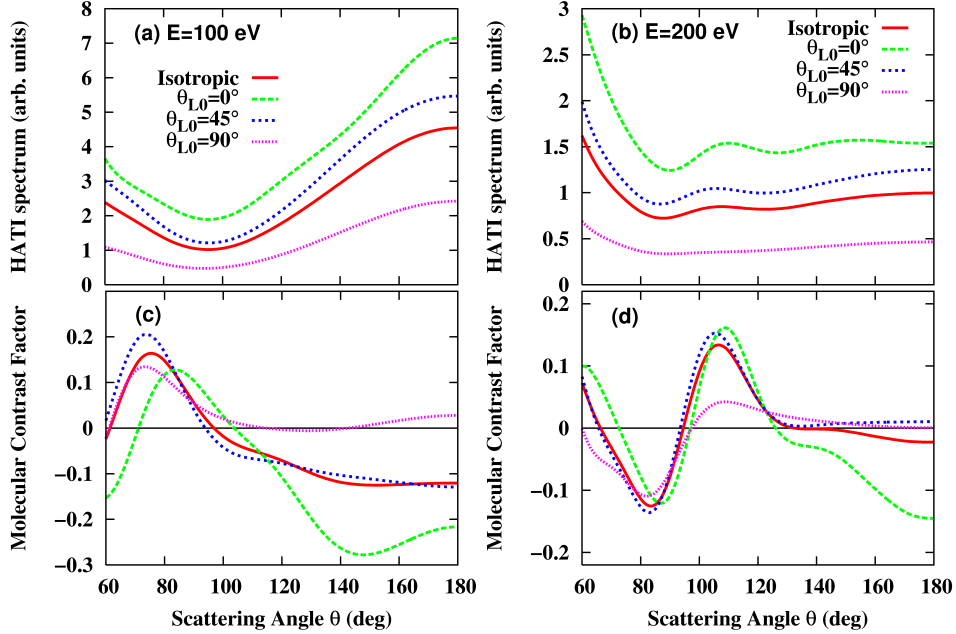
Figure 3.12: *(a,c) Simulation of HATI spectrum of CO_2 at returning electron energy 100 eV and its corresponding molecular contrast factor, based on QRS theory with ionization rate included which is calculated using MO-ADK theory. (b,d) Same as (a,b) but at returning energy of 200 eV.*

carried out at incident electron energy of 200 eV, and the beam is perpendicular to the plane of the molecule. At 200 eV, the DCS for C and F are monotonically decreasing with increasing angles, but not for the heavy iodine atom, see Figure 3.11(d). In the present simulation, a two-term Yukawa potential was used to represent the iodine atom potential.

We have assumed that the molecules are fixed in space, but it is straightforward to generalize the analysis to partially aligned or oriented molecules, as well as other directions for the incident electron beams. In the next subsection, we will show that such flexibility can be easily carried out if the electron beams are replaced by laser induced rescattering electrons.

3.2.3 Electron diffraction using rescattering electrons generated by molecules in an intense laser field

As explained in Section II.B, one can extract field-free DCS, or the diffraction image, of a molecular ion, say CO_2^+, from the HATI electron momentum spectra, by exposing CO_2 molecules to a linearly polarized laser pulse. Within the short time (about three quarters of an optical cycle, i.e., within about two femtoseconds for the commonly used Ti-Sapphire laser) it takes the rescattering electron to return to recollide with the ion, we can safely assume that the atomic positions in the molecule do not change. Thus the diffraction images taken for the ion would reflect the atomic positions of the molecule directly.

In Figure 3.12 we consider partially aligned CO_2 molecules with a distribution assuming to be given by $\cos^6(\theta_L - \theta_{L0})$ as before. From the HATI spectra we can extract the diffraction images, or the DCS. The results for returning energies of 100 eV and 200 eV are shown for a number of alignment angles and for isotropic molecules, see Figures 3.12 (a,b). The corresponding molecular contrast factors are also shown, see Figures 3.12 (c,d). The alignment-dependent tunneling ionization rates used in obtaining Figures 3.12 are taken from [116].

To simulate the HATI spectrum, we need to calculate elastic scattering cross sections for $e^-+CO_2^+$ collisions. Unlike CO_2 target, when the incident electron is far away from CO_2^+, it sees a $-1/r$ potential. Thus it is generally expected that the DCS for $e^-+CO_2^+$ and e^-+CO_2 are quite different. This is true for DCS at small angles where the incident electron probes the outer-shell region. For HATI spectra, the returning electrons are backscattered. They are scattered near the atomic core where the potential is basically the same for the ion and the neutral. Thus we expect the difference in the DCS between neutral and singly charged ions to be negligible for these deep-penetrating scattered electrons. We have checked this conclusion for atomic targets, for energies near and above 100 eV. For our purpose here we check CO_2 in a different way. In Figure 3.12, we calculated the DCS for $e^-+CO_2^+$ collisions, using the IAM model for O-C$^+$-O, O$^+$-C-O and O-C-O$^+$, and the results are averaged with

equal weights. The bond length between C-O was set at 1.163 Å. We treat such result as experimental data and use the IAM model for neutral CO_2 to retrieve the bond length of C-O, using angle-averaged DCS and the GA. The retrieved bond length was 1.149 Å. In other words, unless we are searching for much higher precision, we may as well just use the IAM for neutral molecules for the retrieval of the structure parameters. A more rigorous study on the core-penetrating nature of electron collision with atoms and molecules and identicalness of e-neutral and e-ion DCSs at electron energies above 100 eV will be addressed in Chapter 4. We comment that the error for using IAM is expected to become larger if the scattering energy becomes smaller. For atomic ion, for example, C^+, the potential was written as $V(r){=}{-}(1 + 5e^{-1.532r})/r$ where the exponential parameter was obtained by fitting to the ground state energy of C.

We comment that experimental data from CO_2 for returning electrons with energies at or above 100 eV are not available yet. HATI spectra for CO_2 have been reported by Cornaggia[93,94,110,137] using 800 nm Ti-Sapphire lasers. The returning electron energies from this experiment are about 15-30 eV. At such energies the IAM does not work so the C-O bond length cannot be simply retrieved. Other HATI spectra have been reported for randomly distributed[93,108,109], and for aligned N_2, O_2 molecules[65,110], but only for 800 nm Ti-Sapphire lasers. Again, these data cannot be analyzed using the model presented here. To reach returning energies of 100 eV or more, mid-IR lasers will be needed. Since aligned CO_2 has been used in high-order harmonic generation by mid-IR lasers already[138,139], it is highly desirable to measure HATI spectra in the mid-IR regime from unaligned/aligned N_2, O_2 and CO_2 (or any other simple molecules) to test the theory presented here.

3.3 Summary and Perspective

In this chapter we demonstrated that it is possible to use intense mid-infrared lasers to probe the structure of a molecule. The idea is to use the rescattering electrons generated by the laser. Two basic theoretical ingredients are used here. First, based on the quantitative

rescattering theory for strong field physics, it has been shown that the angular distributions of the high-energy photoelectrons generated by the strong field can be used to extract field-free elastic differential cross sections by the rescattering electrons. These are electrons that have been backscattered from the molecular ion. Thus they are sensitive to the positions of atoms in a molecule, similar to electron diffraction images generated by few hundred keV's electrons in the conventional electron diffraction method. Second, we have established theoretically that the simple independent atom model used in GED can be extended to incident energies in the order of 100 eV, so long that we restrict ourselves to electron images taken at large angles. We established the validity of IAM using electron scattering data taken in the 100-200 eV region for a few molecules. From these limited data we confirm that they can be used to retrieve the bond length of the molecules. Since femtosecond mid-infrared laser pulses are already available, this would suggest that mid-IR laser pulses should be investigated further for its potential for dynamic imaging of transient molecules. Experimentally, current technologies are capable of generating such spectra, for randomly distributed and for aligned molecules. Using CO_2 as an example, we have made the theoretical analysis of HATI spectra from aligned CO_2 molecules. It is desirable that such data become available soon experimentally. This will be the first step toward using mid-IR lasers for dynamic imaging of molecules.

Chapter 4

Mid-IR LIED for Probing Rare Gas Atoms

The theoretical underpinning of molecular imaging is based on the independent atom model with its assumption that probing electrons are able to resolve each atomic core, which is well localized in the molecule. In IAM, the electron diffraction is described as coherent scattering by independent atomic cores in the molecule. For decades, IAM has been well tested and widely used in stereochemical analysis of GED with multi keV electrons involved[3]. In Chapter 3, we have theoretically examined and validated the applicability of IAM for electron energies around 100 eV using e-molecule large-angle collision data, demonstrating resolving powers for molecular bond lengths as small as 5 pm. We also demonstrated the preference of mid-IR lasers to generate electrons with such high rescattering energies for molecular imaging. For LIED, however, the inherent presence of the laser field calls for a more direct and rigorous study. In this Chapter we report high resolution photoelectron angular distributions of rare-gas atoms recorded at mid-infrared wavelengths, generating e-ion recollision events at energies up to 300 eV. This investigation is dedicated to the atomic response in LIED for laser parameters that, when used for molecular targets, are suitable to determine accurate molecular structural information via IAM on a femtosecond time scale. Here we show that (1) At 100 eV or more, the DCS at large angles for neutral atoms and singly-charged ions are nearly same. (2) The DCS extracted using arbitrary

laser intensities and wavelengths are identical for a given returning electron energy; (3) The returning electron wavepacket displays no target structure dependence and its spectral density when scaled in field units obeys a simple universal scaling law. The first finding indicates that the electron's high rescattering energy promotes core-penetrating collisions, and the e-atom interaction is dominated by the strong short range atomic-core potential while the bonding valence electrons look transparent. This is crucial to the applicability of IAM. While the last two findings are anticipated from the QRS theory, a direct experimental demonstration is essential since experimental spectra are taken from the laser focal volume where the intensity is not uniform and not known well in general. The material in this chapter is adapted from a preprint[97].

4.1 Experimental Setup and Data Analysis

Two tunable laser systems producing intensities exceeding 200 TW/cm² are used in the experiments reported here. A mid-infrared system based on difference frequency generation and self-phase modulation produces tunable 3.2-3.9 μm, 100 *fs*, 150 μJ pulses[140]. A second system based on optical parametric amplification pumped by a titanium sapphire subsystem (0.8 μm, 50 *fs*, 4.5 mJ) delivers 1.7-2.3 μm, 50 *fs*, 500 μJ pulses[141]. Photoelectron spectra were recorded in two field-free time-of-flight electron spectrometers using multichannel plate detectors (MCP). To ensure good angular resolutions, small pinholes were installed in front of the MCP detectors, restricting the collection angle to ±1 degrees. Angular distributions were recorded using half wave plates rotated in 1° or 2° steps, with 10^6 laser shots per angle. Additional experimental details can be found elsewhere[142,143].

According to QRS, the detected photoelectron angular distributions $D(p, \theta)$ can be factorized simply as:

$$D(p, \theta) = W(p_r)\sigma(p_r, \theta_r), \tag{4.1}$$

where $W(p_r)$ and $\sigma(p_r, \theta_r)$ are the momentum distribution of returning wavepacket and the electron DCS for free electrons scattering on the target ion, and p, p_r, θ and θ_r are
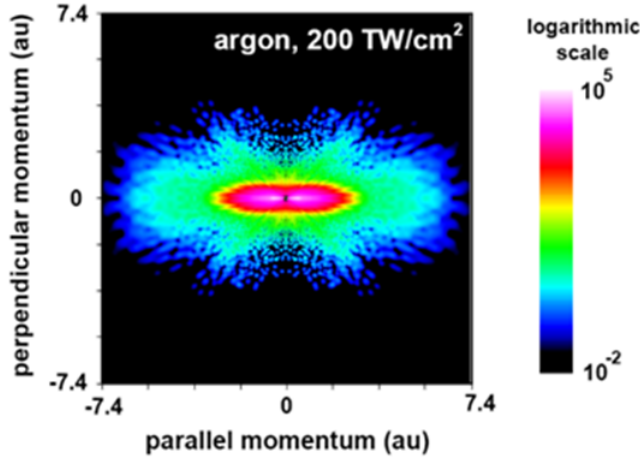
Figure 4.1: *two dimensional photoelectron momentum distributions for Ar irradiated by laser pulses with the wavelength of 2000 µm at the intensity of 2×10^{14} W/cm²*

the detected momentum, rescattering momentum, detected angle and rescattering angle, respectively. In QRS, p and p_r are related (in atomic units) by $\mathbf{p} = \mathbf{p}_r - \mathbf{A}_r$, where the additional momentum $\mathbf{A}_r$ is the the vector potential at recollision. According to the rescattering theory, electrons that return at a given p_r can follow a long trajectory or a short trajectory. Using mid-infrared lasers we are following electron collisions that have return energy of 0.5-2.3 U_p instead of the maximum available energy of 3.2 U_p. For such energies, the wave packet is dominated by contribution from long trajectories since these electrons were born near the peak of the field where the tunneling ionization rate is much larger. Momentum bin $\Delta p_r \sim 0.05$ a.u. is taken when the DCS is extracted from experimental data at a fixed p_r. Compared to previously reported experiments performed using 0.8 µm fields[91–95], the present work investigates the applicability of QRS deep in the tunneling regime.

4.2 Experimental Data and Results

Figure 4.1 shows a typical photoelectron momentum spectra with mid-IR lasers. It was taken from Ar exposed to a 50 fs, linearly polarized, 2 µm mid-IR laser at the peak intensities
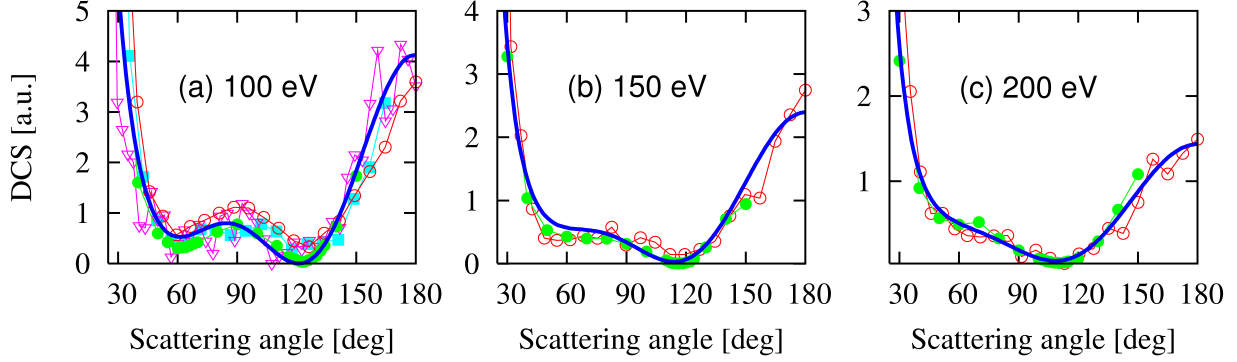
Figure 4.2: *(a) Extracted DCSs of Ar at 100 eV from HATI spectra for different combination of laser intensities and wavelengths. Red circles: 2 μm and 235 TW/cm^2; magenta triangles: 2 μm and 200 TW/cm^2; cyan solid squares: 2.3 μm and 380 TW/cm^2. Green filled circles are experimental DCS for e-Ar collision using electron guns[148], and the blue full curve are theoretical e-Ar$^+$ DCS. (b) At 150 eV, e-Ar$^+$ DCS (red circles) is extracted from HATI spectra at 2 μm and 235 TW/cm^2, in comparison to theoretical e-Ar$^+$ DCS (blue line) and experimental e-Ar DCS (green filled circles)[148]. (c) Same as (b) but for 200 eV.*

of 2×10^{14} W/cm^2. The horizontal axis is the momentum along the polarization axis while the vertical axis is perpendicular to it. Compared with photoelectron spectrum obtained using Ti-Sapphire lasers (see Figure 1.1), the most significant difference is that the angular distribution of the low energy direct electrons in Figure 4.1 is tightly squeezed along the laser polarization. Previous experiments with near IR lasers have been mainly limited, in the language of Keldysh[144], to the multiphoton or mixed ionization regime, and direct electrons fan out in the momentum space, resulting in the broad transverse momentum distribution. In our current work with mid-IR radiation, we are deep in the tunneling regime. According to ADK theory, the perpendicular momentum width is proportional to $E^{1/2}$, about one $4^{th} \sim 10^{th}$ of the parallel width, which is about A_0[145–147] (here A_0 is about 3.32 a.u.). Therefore the direct electrons mainly contribute to a very narrow region along the laser polarization direction.

In Figure 4.2(a) we present the relative DCS extracted in the case of argon for different laser parameters (given in the caption) for 100 eV electrons. We notice that irrespective of the laser parameters, the extracted DCS are identical as predicted by QRS, thus demon-

strating the robustness of the LIED approach. In contrast to the monochromaticity of the the usual CED electron beam, the LIED returning wave packet is broadband, ranging from 0 to 3.17 U_p. As a consequence, one can extract a series of DCS for different returning electon energies from a *single* measured photoelectron angular distribution. For example, in Figure 4.2 (b) and (c) we depict two additional LIED DCS for 150 eV and 200 eV rescattering energies, respectively, from the experimental data taken at 2.0 μm and 235 TW/cm^2 (U_p=88 eV). As the electron energy increases, the diffraction peak at 180° is constantly suppressed compared to the low angle signal, whereas the maximum at about 90° becomes less conspicuous and finally flattens out at 200 eV. It is also worth noting that the range of returning electron energy shown here spans from 1.14 U_p to 2.27 U_p, far from the 3.17 U_p classical cutoff. Finally, a general feature of intense laser photoelectron spectrum is that longer wavelengths produce angular distributions of direct electrons "squeezed" along the laser polarization direction compared to shorter wavelengths; consequently, contamination of the DCS with direct electrons takes place predominantly at small angles. The DCS taken using 2.0 μm pulses depicted in Figure 4.2 are extracted from 30° to 180°, compared to a reduced 110°-180° range covered in experiments using 0.8 μm laser fields[91,92]. Therefore, mid-IR lasers can provide large-range momentum transfer, a critical requirement for achieving good spatial resolutions for molecular imaging.

The extracted DCS at each energy is also compared to theoretical calculations for field-free e-Ar$^+$ collisions. The e-Ar$^+$ interaction is approximated by a model potential in the form

$$V(r) = -(1 + a_1 e^{-a_2 r} + a_3 r e^{-a_4 r} + a_5 e^{-a_6 r})/r, \tag{4.2}$$

where the parameters in the potential are given in[105]. These parameters are obtained by fitting to the binding energies of the ground state and first few excited states of Ar, with the constraint that $1+a_1+a_5=Z$, where Z represents the nuclear charge. The calculated DCS depicted in Figure 4.2 are in good agreement with experimental ones despite the large scattering of the data. On each graph, we also show the experimental DCS from e-Ar
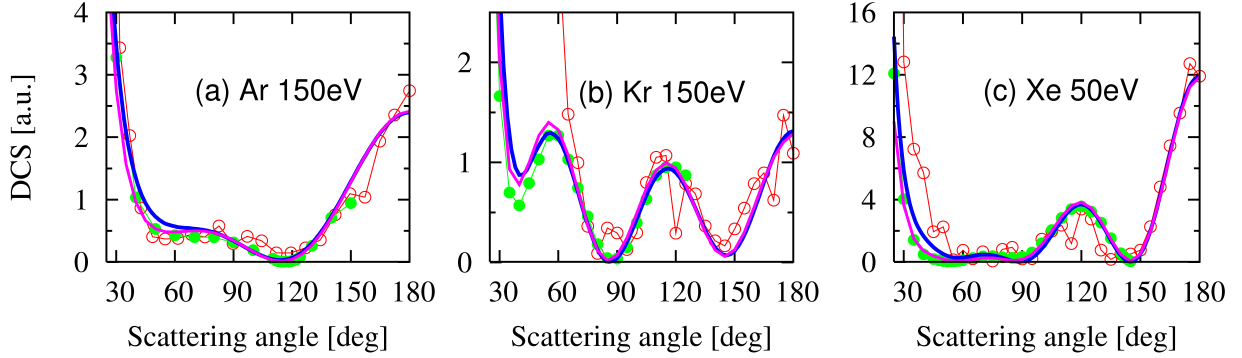
Figure 4.3: *Comparison of DCS from LIED for Ar, Kr, and Xe at 150 eV, 150 eV, and 50 eV, respectively. DCS from HATI: red circles; theory e-ion (blue solid lines); experimental e-neutral (green filled circles); theoretical e-neutral (magenta solid lines).*

collisions[148]. The neutral and ionic DCS for return energies above 100 eV are essentially identical, thus demonstrating that the long range Coulomb potential plays no role in large angle scattering. These collisions are due to scattering close to the center of the atom (less than 0.5 Å for Ar at 100 eV), where the potentials for the neutral and cation are essentially identical. This result is essential for applying the IAM to *e*-molecular-cation collisions since it indicates that electron is indeed penetrating and probing the atomic core.

In Figure 4.3, the DCS extracted from the HATI spectra for Ar at 150 eV, Kr at 150 eV, and Xe at 50 eV are shown. These atoms are irradiated with 2 μm, 50 *fs* pulses at 235 TW/cm^2, 180 TW/cm^2, and 72 TW/cm^2, respectively. On each figure, experimental *e*-neutral-atom DCSs are also shown[148–150]. In the angular region they overlap the two data set agree well, except that the LIED data show larger scattering. Two theoretical curves are also shown in each figure, one from the simple model potential approach for *e*-cation collisions as described above. The other is based on the more sophisticated *e*-neutral-atom collisions given in the literature[151–153]. For Ar and Kr, the difference between the two theories is small over a broad angular range from 70° to 180°. For Xe, due to its lower scattering energy, two theories overlap only at angles larger than 100°, and show a big discrepancy at smaller angles (see supplemental material of the reprint by Xu et al.[97] for the clearer comparison in log scale). Based on the comparison here as well as in Figure 4.2 we can say that the

e-neutral and *e*-cation DCS are the same at the collision energies above 100eV and angular range shown. These conclusions are important for electron diffraction experiments at large scattering angles for 100 eV or higher collision energies.

From the structural retrieval viewpoint, can one use the DCS obtained from the HATI spectra to draw information about the target? For the present purpose, we assume that each cation is represented by a model potential. We assume that the model potential is parameterized in the same form as Eq. 4.2, with six unknown parameters $\{a_1, a_2, a_3, a_4, a_5, a_6\}$ to be fitted.

We used only the data set of Figure 4.3 (i.e., only one collision energy and a limited angular range [70°, 180°] spanned by the experimental data points) and used genetic algorithm[100] to retrieve the parameters in Eq. (2). To be "fair", we do not impose the condition $1+a_1+a_5=Z$, i.e., we assume that we do not know the nuclear charge of the atom. To help GA to converge to the correct answer, we impose constraints on effective nuclear charge $Z(r) = -rV(r)$ that $Z(r)>0$, Z is between 0 and 70, and $Z'(r)>0$ which are clearly satisfied for the potential of the atom of interest here. From the returned best fit we obtain the model potential for each atom. The retrieved nuclear charges Z are 18.6 for Ar, 38.7 for Kr, and 50.0 for Xe, which are close to the correct values for these rare gas atoms. The accuracy is not good enough to identify which atom it is, but it certainly can identify which of the rare gas atom is. This limitation is not due to the LIED itself. Since the potential was retrieved from a single collision energy, only a small part of the model potential is probed by the scattering experiment. This can be seen by comparing the retrieved effective charges with those fitted in the paper by Tong et al.[105]. The comparison of the two effective charges is given in the left panels of Figure 4.4. Note that for Ar and Kr, the two sets of curves agree well within about 0.5 a.u. The discrepancy at larger r is not surprising since this part of the potential is not important for the DCS at 150 eV and scattering angles above 38° for Ar and 60° for Kr. This illustrates an important but obvious lesson in scattering theory that each scattering event probes only a certain aspect of the target. As an illustration, we now used
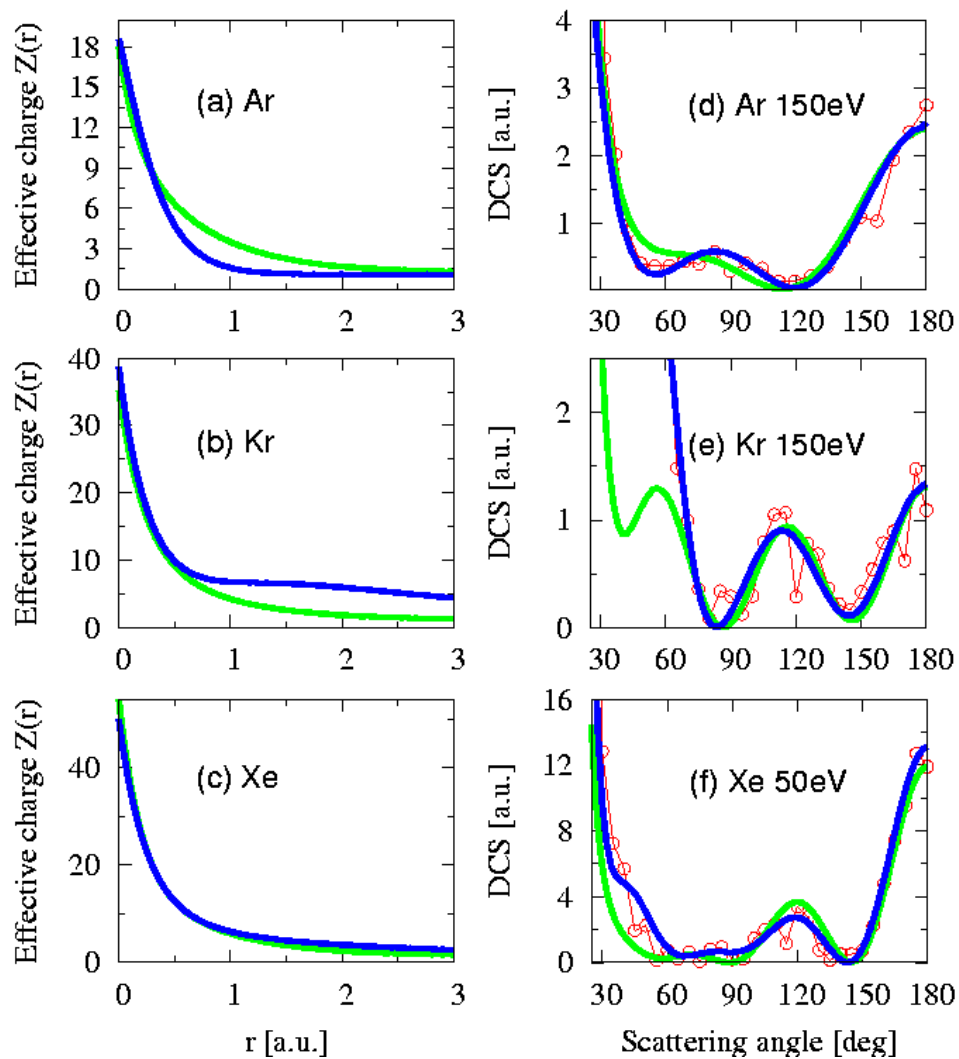
Figure 4.4: *Retrieved atomic potentials from DCS from the LIED data in Figure 4.3 for Ar, Kr and Xe, respectively. In (a,b,c), blue lines are the fitted effective charges as a function of r, compared with a "known" potential for each atom (green lines). DCS calculated from the fitted potentials are shown in (d,e,f) by the blue lines. Experimental data from LIED (red circles) and DCS from the known potentials (green lines) are also shown.*

the retrieved potential from GA to calculate the DCS. In the right panel of Figure 4.4 we also depict the calculated DCSs using fitted potentials. We can see that the DCS extracted from the HATI spectra are indeed well reproduced, despite that the two potentials are quite different at larger r, as seen in the right panels. In the case of Xe, the returning energy 50 eV is relatively low thus it would probe the larger r region. Figure 4.4(c) shows that the two potentials agree well up to about 1 a.u..

As a further remark, we comment that DCS from lower energy electrons would probe the effective potential of the outer part of the atom. However, at low energies, electron exchange and many-electron effects become important and thus it is less accurate to describe the collision by an effective potential. The more accurate and detailed the measurement is, the more sophisticated, i.e., the fewer approximations, the theory should be used. Thus in low-energy electron scattering or photoionization experiments, one often does not attempt to retrieve the "structure" of the target from the measured cross sections. In other words, our understanding of the "structure" of the target is always limited by what measurements were made.

Similar to all previously reported data, up to now we have only used LIED to extract relative field-free DCS. According to the QRS, i.e. Eq. (4.1), from the measured angular distribution if one knows the absolute DCS it is possible to extract the relative spectral weight of the returning wave packet. Experimental RWP at fixed p_r is defined as the overall factor that the absolute DCS $\sigma(p_r)$ multiplies to be normalized to the extracted relative DCS at p_r. Scanning p_r, we can obtain RWP as a function of returning electron momentum. In Figure 4.5 we plot the extracted returning wave packets for Ar, Kr, and Xe at different laser parameters. The extracted returning wave packet displays a monotonic decrease, attributable to the fact that electrons returning with high energies are born after the peak of the laser field when the tunneling rate decreases. The monotonic decrease in the returning wave packet spectral density with increasing the electron momentum is a general feature, observed in all collected data sets. When the electron momentum is plotted
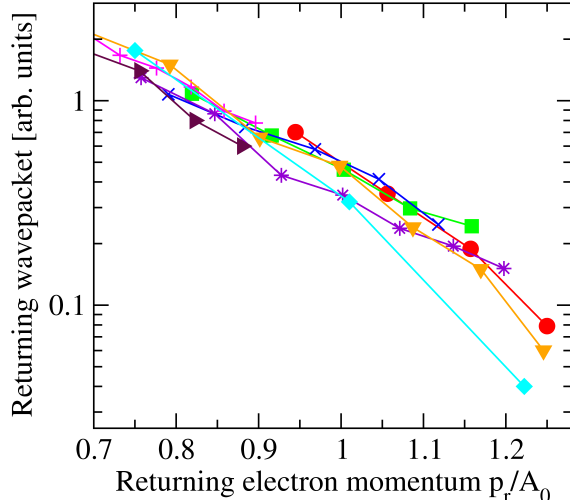
Figure 4.5: *Returning electron wave packets against returning electron momentum extracted from the photoelectron spectra for different laser parameters and different atoms. (Target, wavelength in μm, intensity in TW/cm^2) are: Red points: (Ar, 1.7, 208); green solid squares: (Ar, 2.0, 200) ; blue crosses: (Ar, 2.0, 215); purple asterisks:(Ar, 2.0, 235); magenta pluses: (Ar, 2.3, 380); orange solid inverted triangles: (Kr, 2.0, 180); maroon solid right triangles:(Kr, 3.6, 98) ; cyan solid diamonds: (Xe, 2.0, 72).*

in units of the corresponding maximum value of the vector potential A_0, a scaling law $W(p_r/A_0) \sim (p_r/A_0)^{-2.6\pm0.3}$ is found. We emphasized that the target independence of the returning wave packet is reflected in the QRS theory. In the case of HHG, similar results have been shown earlier in Levesque et al.[154].

In conclusion, we have demonstrated that with mid-infrared lasers, laser-induced electron diffraction is a powerful method to extract accurate electron-ion collision DCSs with dynamic ranges comparable with traditional gas-phase electron diffraction techniques. The HATI electrons are due to close collisions with the atomic cores and thus the DCS for the atomic cation is the same as that for the neutral. The experimental data also confirmed the predictions of the quantitative rescattering theory that the extracted DCS does not depend on the laser parameters, and that the returning electron wave packet, if plotted in units of the maximum value of the vector potential, is independent of the target and the laser intensity. These results provide the essential ingredients needed for validating LIED for time-resolved structure retrieval of a molecule under conformal transformation, as

demonstrated in revealing the bond relaxation of O_2 and N_2 molecules following tunneling ionization[68], which will be reported in the next Chapter.

Chapter 5

Mid-IR LIED for Probing Diatomic Molecules: Bond Relaxation of O_2^{+*}

The framework of mid-IR laser induced electron diffraction for molecular reconstruction is well put in the previous chapters. It bridges a number of concepts from strong-field rescattering physics and conventional gas-phase electron diffraction: tunnel ionization, high-energy electron production and core-penetrating collisions. In particular, core-penetrating nature of the recollisions, i.e. unimportance of valence electrons, indeed benefit the LIED study of molecules. At the energies mid-IR reaches, we can treat the e-neutral-molecule collision as an e-molecular-cation collision at large scattering angles. In this chapter, we report our LIED investigation on two simple diatomic molecules, N_2 and O_2. This study is performed by measuring the diffracted photoelectron momentum distribution produced by strong-field ionization of N_2 and O_2 at several mid-IR wavelengths (1.7, 2.0 and 2.3 μm). We demonstrate that the experiment has the sensitivity to measure a 0.1 Å displacement in the oxygen bond length occurring in a time interval of $\sim$5 fs after ionization. The investigation establishes a foundation for a novel method for spatio-temporal imaging of gas-phase molecules. The material in this chapter have been published in Nature in 2012[68]. This is a joint work by Agostini-DiMauro's group who carried out the experiments and Lin's Group who did the theoretical analysis.

5.1 Experimental Setup and Data Analysis

5.1.1 Experimental details

Details of the laser system used in the experiment have been previously described. Briefly, an optical parametric amplifier (Topas-HE by LightConversion) pumped by a near-infrared titanium sapphire front end subsystem (0.8 μm, 4.4 mJ, 50 fs, 1 kHz) generates continuously tunable ultra-short (0.5 mJ, 50 fs) linearly polarized pulses from 1.2 to 2.3 μm. Angle-resolved (collection angle 1.6°) photoelectron energy distributions were recorded by focusing the laser in a $\sim$22 cm field-free time-of-flight electron spectrometer using multichannel plate detectors. At each wavelength, the laser driven diffraction image was obtained by rotating the laser polarization with respect to the spectrometer axis in steps of 2° using zero-order half wave plates. The sequence of collection angles was randomized to minimize systematic errors. For each angle, data was collected for approximately 10^6 laser shots, thus ensuring the necessary dynamic range while the count rate was kept below 3 hits/shot to minimize space-charge effects.

The energy Calibration of spectrometer was performed by recording the well-known above-threshold ionization (ATI) spectra of various noble gases with long (230 ps) pulses. The relative energy resolution $\Delta E/E$ of the apparatus was determined to be better than 1.4% inferred from the long-lived Rydberg series present in the ATI spectrum of argon taken with 50 fs, 0.8 μm pulses. Finally, for each wavelength the peak intensities were estimated by analyzing the 2 U_p and 10 U_p classical cutoffs present in the photoelectron energy distribution. The cutoff values agree well with numerical results based on single-active electron quantum calculations and we estimate the accuracy of our technique to be within an error of 15%.

5.1.2 Extraction of DCSs

For each momentum distribution measurement at a given laser peak intensity, select an electron return energy, e.g. 100 eV (p_r =2.71 a.u.). Using the classical dynamics for long

trajectories, calculate the birth (t_b) and return (t_r) times for the prescribed experimental wavelength λ. Using the return time the laser's vector potential, $\boldsymbol{A_r} = \boldsymbol{A}(t_r)$, is determined and finally, using the values of $\boldsymbol{p_r}$ and $\boldsymbol{A_r}$, a scattering circle at constant scattering energy is constructed.

To improve the statistics, a desired uncertainty, Δp_r, is selected, typically a few percent. From $p_r^{min} = p_r - \Delta p_r$ and $p_r^{max} = p_r + \Delta p_r$ the corresponding values for the vector potential, A_r^{min} and A_r^{max} are estimated, respectively. Next, for a given detected angle, θ, we determine the detected momenta p^{min} and p^{max} and scattering angles θ_r^{min} and θ_r^{max} using the sine law for the triangles formed by $(p_r^{min}, A_r^{min}, \theta)$ and $(p_r^{max}, A_r^{max}, \theta)$, respectively. Then, using the raw electron time-of-flight data recorded at an angle θ, we integrate the counts in the time interval, τ, corresponding to the momentum interval $p_r^{max} - p_r^{min}$. Each time bin t is weighted by the Jacobian, $J = p^3$, and the yield of electrons scattered at the angle $\theta_r(\theta) = (\theta_r^{max} + \theta_r^{min})/2$ is obtained. Finally, repeating the above procedure for every detected angle θ, we obtain the yields for electrons scattered with momentum p_r. The statistical error bars plotted in the figures are obtained from the total number of counts N contained in the interval τ, assuming Poisson statistics, i.e. $\Delta N = N^{1/2}$. Obviously, the uncertainty ΔN is directly related to the chosen uncertainty Δp_r and in practice the value is selected to obtain a relative uncertainty $\Delta N/N$ better than 10%.

5.1.3 The Genetic Algorithm fitting procedure

Same as in Chapter 3, we assume the atomic components are known, and need only fit the structural parameters, e.g. the bond length in this study. To calculate atomic scattering amplitudes, the e-atom interaction is modeled by a Yukawa potential $V(r) = Ze^{-\lambda r}r/r$ with $Z = 7$ and $\lambda = 1.695$ a.u. for nitrogen and $Z = 8$ and $\lambda = 1.720$ a.u. for oxygen. Using the experimental DCS, we fit the interatomic distance R using a genetic algorithm. The fitness function is defined as,

$$\chi^2(R) = \sum_i [\frac{I_i^{exp't}}{\sigma_i^{atom}} - \beta \times \frac{I_i^{theory}(R)}{\sigma_i^{atom}}]^2 \tag{5.1}$$

where i refers to discretized values of q and β is a normalization constant since the experimental DCS is not absolute. At each angle, the experimental and theoretical cross sections are normalized by the atomic cross sections in order to have equal weighting at all angles. Recall that the molecular DCS oscillates around the smooth atomic DCS. At the energies treated here, the atomic DCS has a minimum at some angle. The smallest value of q is selected close to where the atomic DCS and the extracted DCS begin to deviate. For computational efficiency, we limit the search to a range of R [0.95 Å, 1.60 Å].

The e-atom interaction is modeled by a Yukawa potential $V(r) = Ze^{-\lambda r}r/r$ with $Z = 7$ and $\lambda = 1.695$ for nitrogen and $Z = 8$ and $\lambda = 1.720$ for oxygen, respectively (see Table 3.1).

5.2 Bond Relaxation of O_2^+

5.2.1 Results and Discussions

Figures 5.1(a,b) shows the photoelectron momentum spectra taken from randomly distributed N_2 and O_2 molecules exposed to a 50 fs, linearly polarized, 2 μm mid-IR laser. The laser peak intensities for N_2 and O_2 are 2.6×10^{14} W/cm^2 and 1.33×10^{14} W/cm^2, respectively. The horizontal axis is the momentum along the polarization axis while the vertical axis is perpendicular to it. Since molecules are not aligned, the electron spectra have cylindrical symmetry. Same as atomic case (see Figure 4.2), the angular distribution of the low energy direct electrons is squeezed along the laser polarization direction for both molecules. DCSs extracted from spectra are displayed in Figures 5.1(c,d) for N_2 and O_2 at p_r=2.97 a.u. (120 eV) and 2.71 a.u.(100 eV), respectively. In comparison to their corresponding IAM predictions, which are calculated with equilibrium internuclear distances, we can see good agreement over the shown angular region for both molecules. As pointed out in Chapter 3, the general features of shown DCSs are due to diffraction from individual atoms, which do not convey any structural information. In the quest for bond length information, we need extract and study the molecular contrast factors.

It is worth noting that for strong-field ionization, a remarkable difference of molecules
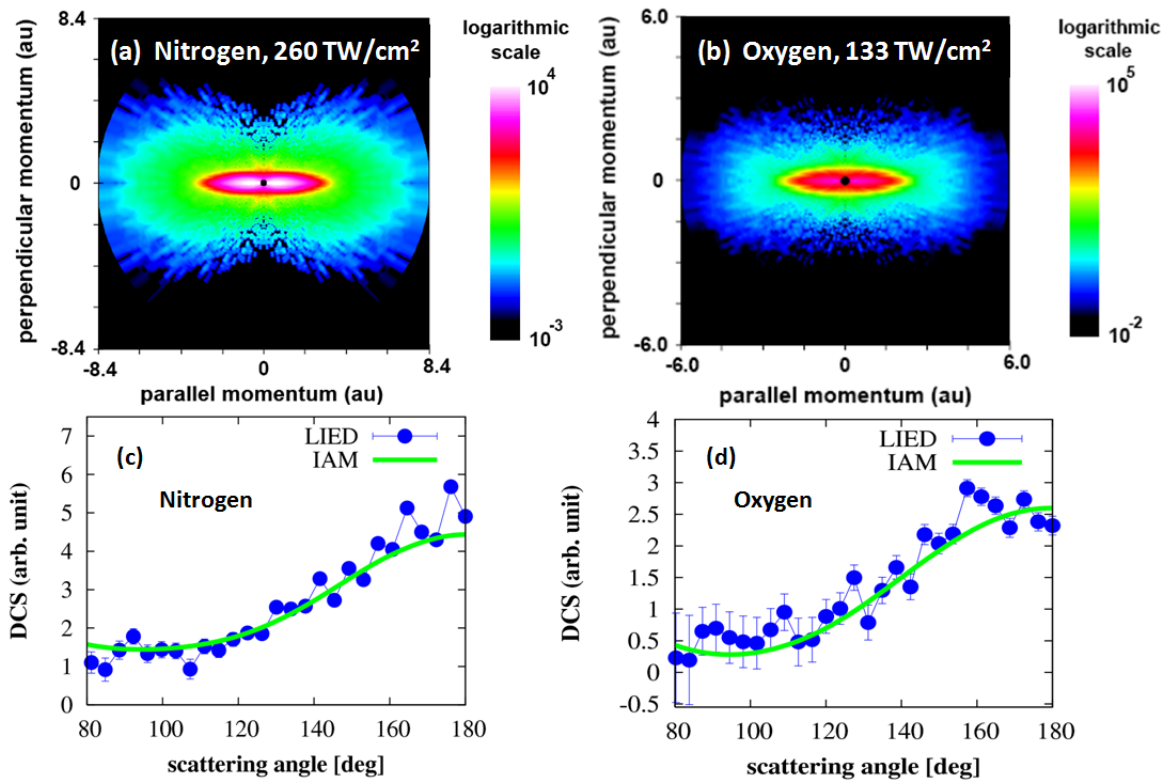
Figure 5.1: *(a,b) angular-resolved photoelectron momentum distributions for N_2 and O_2 irradiated by laser pulses with the wavelength of 2000 μm at the intensity of 2.6×10^{14} W/cm^2 and 1.33×10^{14} W/cm^2, respectively. (c,d) Extracted DCSs from spectra in (a,b) for N_2 and O_2 at $p_r = 2.97$ a.u. (120 eV) and 2.71 a.u.(100 eV), respectively.*

from atoms is that after removal of one electron, the rearrangement of the remaining electrons will result in a adjustment of internuclear distances, which may be big for anti-bonding orbitals such as O_2 and small for bonding orbitals such as N_2. The dynamics of the rescattering process implies that, at constant p_r, the time Δt between birth and rescattering of the electron wave packet is proportional to the laser optical cycle and hence the wavelength. Consequently, following ionization at t_b, the bond length begins adjusting to the new electronic configuration and thus at t_r the returning wave packet captures the diffraction image corresponding to a non-equilibrium internuclear distance. Thus, a series of images captured at different wavelengths equates to mapping the nuclear motion. If the electron removal is rapid, then the Frank-Condon (FC) principle[155] can be applied to evaluate the subsequent motion of the vibrational wave packet. We emphasize that FC estimates are only approximate since tunnel ionization is not expected to be of the impulsive nature. In this study, the photoelectron momentum distributions of N_2 and O_2 are measured at three mid-IR wavelengths, 1.7, 2.0 and 2.3 μm. The three wavelengths are, in principle, probing the internuclear separation 4-6 fs after tunneling ionization.

We will start our analysis with N_2. The baseline for our LIED investigation was ionization of the highest occupied molecular orbital (HOMO) of N_2, the bonding σ_g orbital. Removal of a σ_g electron results in a small change in the equilibrium N-N distance from 1.10 Å (neutral) to 1.12 Å (ion)[156]. The experimental DCS (e.g. Figure 5.1(c)) is matched to an IAM calculation by fitting the normalization constant and the internuclear separation so as to minimize the variance between experiment and theory. Figure 5.2(a) shows the best fit MCF (red line) retrieved from the 2 μm experiment (symbols), obtained with a N-N distance of 1.14 Å. Comparing conventional molecular collision data at similar collision energies (see Chapter 3), we estimate a 0.05 Å error on the retrieved bond length. For comparison, we also plot in Figure 5.2(a) the theoretical MCF calculated for N-N distances deviating from the fitted value by ± 5 pm (dashed lines) and equal to that of neutral N_2 (dotted line). Figure 5.2(c) shows the analysis performed for a collision momentum of 4.11 a.u. (230

eV energy) using 290 TW/cm^2, 2.3 μm pulses. The retrieved N-N distance is 1.12 Å. In addition, LIED measurements performed at 1.7 μm result in a retrieved bond length of 1.15 Å. These three retrieved bond lengths are plotted in Figure 5.2(e) as a function of time, using the classical correspondence with wavelength discussed above. The three retrieved bond lengths agree, within a 0.05 Å uncertainty, with the accepted N$_2$ equilibrium value. However, the experiment cannot resolve the small N-N bond motion ($\sim$0.02 Å) during the 4-6 fs time interval following tunnel ionization.

In contrast to N$_2$, the O$_2$ HOMO is an anti-bonding a π_g orbital and ionization leads to a large change in the O-O equilibrium distance from 1.21 Å (neutral) to 1.10 Å (ion)[156]. Following the same procedure as outlined above, the extracted O-O distances for 1.7, 2.0 and 2.3 μm LIED measurements are 1.10, 1.11 and 1.02 Å, respectively. Figures 5.2(b) and (d) present the MCF analysis at the last two wavelengths, again by comparing experimentally determined MCF values against the theoretical best fit, and against theoretical fits obtained for a bond length that differs from the best fit by $\pm$5 pm or is equal to that of neutral O$_2$. In contrast to the N$_2$ experiments, the MCF curve calculated using the neutral equilibrium distance does not fit the experiment at either wavelength. The O-O distances derived from the best fits deviate by 2-4 standard deviations from the equilibrium value, providing a high degree of confidence ($>$ 99.9%) that the bond has shortened in the 4-6 fs interval after ionization. The FC curve in Figure 5.2(f) shows the free time evolution of the center of the nuclear wave packet (O-O distance, solid red line) whereas red dotted lines indicate its width (FWHM). The three experimental data points in Figure 5.2(f) clearly show a statistically significant reduction (0.1 Å) in the O-O bond length from its initial, neutral equilibrium distance of 1.21 Å, as indicated by the vertical arrows. However, the spatial resolution of the experiment is insufficient to track the much smaller bond length change ($\sim$0.05 Å resolution) occurring within the 4-6 fs time window spanned by the three measurement points.
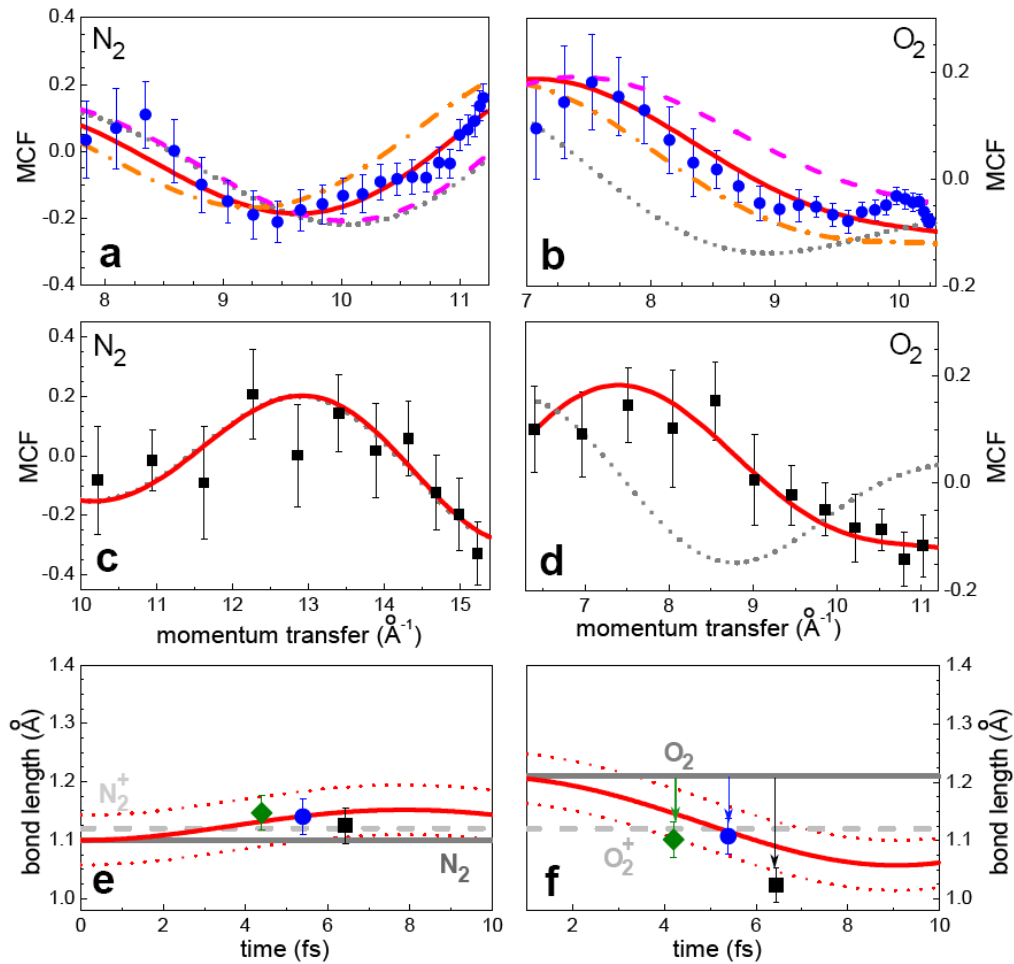
Figure 5.2: *(a-d) MCF extracted from the experimental data (scattered symbols) in comparison with theoretical predictions. The best fit bond lengths are obtained by fitting the DCS extracted directly from the measurement. The red solid line is the MCF calculated using the best fit bond length. The gray dotted line is the MCF calculated using the equilibrium bond length. The dash magenta and dashed-dotted orange lines in (a,b) are the calculated MCF using bond lengths that deviate by -5 pm and +5 pm, respectively, around the best fit. The error bars obey a Poisson statistical distribution. (a) N_2 data with 260 TW/cm^2, 2.0 μm pulses (p_r = 2.97 a.u.). (c) N_2 data with 290 TW/cm^2, 2.3 μm pulses (p_r = 4.11 a.u.). (b) O_2 data with 133 TW/cm^2, 2.0 μm pulses (p_r = 2.91 a.u.). (d) O_2 data with 150 TW/cm^2, 2.3 μm laser (p_r = 2.97 a.u.). (e,f) Illustration of bond changes for N_2 and O_2 following ionization. The bond lengths extracted from the LIED measurements at each wavelength (squares: 2.3 μm, circles: 2 μm, diamonds: 1.7 μm) are corelated with the propagation time based on a classical analysis. The red curves depict the evolution of the nuclear wave packetfs center (solid) and its associated full width at half maximum (dotted), computed in the FC approximation. The equilibrium bond length is indicated by the solid (neutral) and dashed grey (ion) lines. For O_2, the vertical arrows indicate that the measured bond lengths for all three wavelengths are consistently shorter (∼0.1 Å) than the neutral's equilibrium length and statistically meaningful.*

79

5.2.2   Error estimate of Contribution of Excitations in LIED

Both GED and LIED experiments measure the differential cross sections of molecular targets produced by energetic electrons. Typical neutral molecules have excited electronic (in addition to rotational and vibrational) states that are only a few eV's above the ground state, thus the measured DCS would inevitably include contributions from both the elastic and inelastic scattering. However, theoretical DCS calculated within IAM does not explicitly include the DCS from inelastic collisions. How much error does this approximation introduce? This issue could potentially compound the interpretation of an LIED experiment. Below we show through a combination of theoretical analysis and experimental evidence that contribution of inelastic collisions to the DCS is small.

In the IAM model, a molecule is approximated as a collection of non-interacting atoms. If the interactions among the atoms are included, then molecular orbitals are formed by a combination of atomic orbitals. Thus for N_2, the set of molecular orbitals that are constructed from the $2p$ orbitals of the the two nitrogen atoms should be degenerate, and included as elastic channels within the IAM. [Analogously: if spin-orbit interaction is not included, then the fine structure levels are treated as degenerate.] Clearly this is a good approximation only when the collision energy is large compared to the excitation energies. For excitation energies of 10 eV and collision energies of 100 eV, at each scattering angle, the difference of momentum transfer for the elastic and inelastic processes will differ by ∼2.5%. Assuming that the inelastic collision is as important as elastic scattering then a 2.5% error is introduced into the bond length determination. However, typical experimental data for neutral targets shows that for incident energies of 100 eV or higher the inelastic cross sections are only a few percent of the elastic channel[157]. Differential measurements for $e^- - ion$ collisions, such as N_2^+ and O_2^+, are rarer and unfortunately, to the best of our knowledge, nonexistent, including the energies covered in our experiment. Therefore, we take the ratio of a few percents or less for the inelastic collision as compared to the elastic one around 100 eV to be true for molecular ion targets just as it was found for neutrals. In addition,

the elastic and inelastic DCS recorded at the same collision energy for N_2O experiment[158] display a very similar angular dependence for both channels at large scattering angles. This is easily understood since large-angle scattering occurs only when the electron is scattered close to the atomic core, thus a loss of a few eV's in the incident energy due to excitation will not significantly alter the scattering angle or shift the interference fringe pattern. Thus we conclude, as has been done for decades in GED experiments, that IAM is a valid model for DCS analysis in our LIED measurement.

5.2.3 Error Estimate of the Recollision Time

In our experiment, pulses of 50 fs duration are used (7-8 cycles at 2 μm). The time propagation of the electron between birth and recollision $\Delta t = t_r - t_b$ is calculated from 1D classical mechanics, ignoring the ionic potential. For the long trajectories, Δt is 4.3, 5.4, and 6.3 fs for the wavelengths of 1.7, 2.0, and 2.3 μm, respectively. These estimated times can be modified by several factors and are discussed below.

First, as discussed earlier, Δt depends on the value of the vector potential at the atom position and therefore must be averaged over the focal volume intensity distribution. It is reasonable to limit the range of intensities to $\pm 15\%$ because of the exponential dependence of the tunneling rate. The resulting uncertainty on the propagation time is approximately 0.2-0.3 fs.

Second, the classical model predicts two classes of rescattering trajectories, dubbed short and long. Our analysis of the high-energy events is based on long trajectories but the short trajectories will affect the propagation time for all detected energies except at the 10 U_p cutoff where the two trajectories merge. The corresponding times are approximately a quarter-cycle shorter (2 fs at 2 μm) than the long but this difference decreases rapidly with increasing return energy and vanishes at the cutoff. The exact contribution of the short and long trajectories to the LIED image is difficult to evaluate but some general statements can be inferred. For one, the short trajectories have an initial phase that is later in the field-cycle
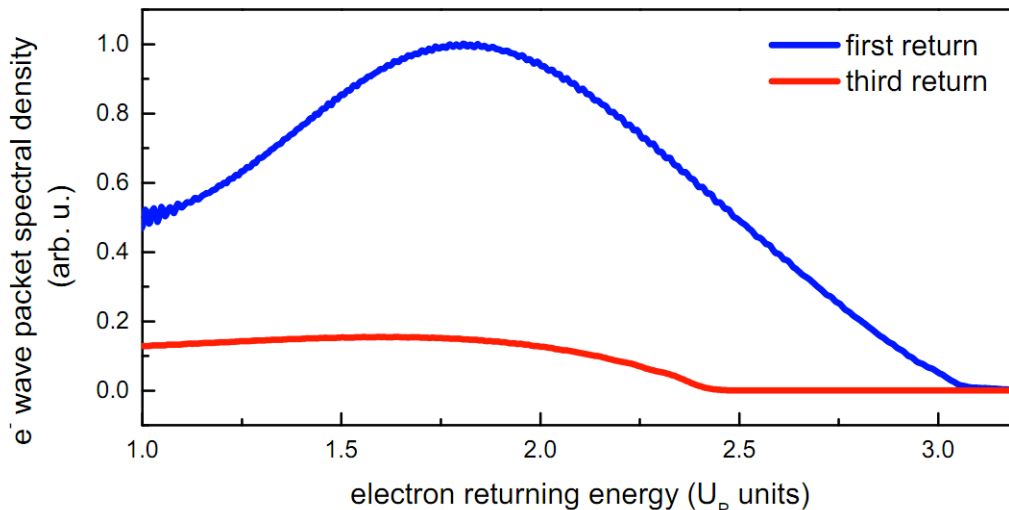
Figure 5.3: *Comparison of rescattering momentum distributions due to the 1st and 3rd returns for a 15-cycle, 2 μm pulse at peak intensity of 1.2×10^{14} W/cm^2. The quantum calculation is performed using the strong field approximation (SFA2) and the results were averaged over the laser focal volume.*

(low field amplitude) electric field strength favors long trajectory production. For the return energies of 1.5-2 U_p typically used in our LIED analysis and a peak intensity at 1.3×10^{14} W/cm^2, the short trajectory contribution is 6-14% of the long one. For a 2.3 μm LIED experiment this would give return times of 3.3±0.2 fs and 6.3±0.2fs for the short and long trajectories, respectively. For our current LIED investigation, a conservative estimate of the temporal resolution is 2-3 fs. However, improvement in future experiments can increase the temporal resolution by analyzing the electron momentum near the classical cutoff or using bichromatic fields for differential control over the short and long trajectories. Resolution of this issue needs further experimental and theoretical investigations.

Third, the electron wave packet continues to oscillate in the field after the first recattering and may re-encounter the ion several more times, resulting in a large uncertainty in the recollision time. These multiple returns are all children of the long trajectory discussed above and as it continues to propagate the wave packet spreads ($\propto \lambda^2$) in the transverse dimension, thus diminishing the electron flux with each subsequent return. In addition, the

rescattering energy is reduced below 2.4 U_p for these multiple returns, as compared to 3.2 U_p for the first returns. Thus the high energy portion of the momentum distribution is produced mostly by single return events. Furthermore, if the multiple returns were significant, then the recollision events in LIED would temporally sample the molecular core at very different internuclear distances. Consequently, the MCF fringe visibility would be strongly reduced due to the sum of shifted patterns and it would be impossible to fit the data with a single R value, let alone derive physically significant bond lengths. In fact, the importance of multiple returns has been previously analyzed for 0.8 μm ionization[90]. Using the second-order strong-field approximation[90], we calculate the wave packets for the first and third returns for 2 μm pulses. The result is plotted in Figure 5.3 and includes the average over the focal volume intensity distribution. The figure shows that at a 2 U_p return energy, the 3rd-return is only 12% of the 1st-return and its contribution diminishes at higher energies. U_p is defined by the peak intensity at the focus. The 2nd-return (not shown) is not a relevant trajectory since the field drives the recollision with the ion from the opposite direction relative the 1st and 3rd returns. In conclusion, the effect of multiple returns is our LIED measurements is considered negligible. In the future, experiments using few-cycle (2-3 cycles) long wavelength pulses can further reduce this effect.

5.3   Conclusion and Outlook

Our findings illustrate that LIED can image sub-Angstrom structural changes in gas-phase molecules with femtosecond time-resolution. We anticipate that the use of few-cycle pulses, bichromatic fields, additional wavelengths and improved counting rates will enhance the temporal resolution, and that the method can be used in pump-probe set-ups to interrogate molecules undergoing conformational transformations. An exciting next step would be to apply LIED to more complex molecules, to aligned or oriented molecules, and to vibrationally or electronically excited molecules. Compared to a GED experiment, LIED's ability to coherently control the returning electron wave packet via bichromatic laser fields and/or

ellipticity could open new paths in electron diffraction.

Chapter 6

Final Remarks

In recent years, strong-field imaging has become one of the most promising approaches to investigate ultrafast dynamics of molecules on the femtosecond timescale[13]. Earlier works have demonstrated the potential of laser-induced electron diffraction for molecular imaging because of the sensitivity of the photoelectron spectrum to structures of matter[74,76].

In this dissertation, I aimed at formulating this new molecular imaging scheme, which can be summarized in three pragmatic steps[68]:

1) measure the electron momentum angular distribution produced by tunnel ionization by a mid-infrared laser. The relevant electrons in the distribution are those created by high-energy rescattering events (>100 eV), whose de Broglie wavelength is comparable to typical bond size (1 Å).

2) Extract *field-free* electron-ion differential cross sections at large scattering angles from the momentum distribution using the principles of the quantitative rescattering theory. The theory formalizes the LIED process as a field-driven wave packet (as the electron beam in GED) scattering from a molecular ion.

3) Retrieve the best-fit bond length using genetic algorithm, in which theoretical DCSs for different interatomic separations are calculated using IAM and compared to the experimental DCSs.

I also reported in this dissertation the first application of the LIED method formulated above to retrieve the bond lengths of two simple molecules N_2 and O_2, providing the direct

evidence of bond relaxation of O_2^+ following tunnel ionization. LIED is capable of capturing a bond length change of 0.1 Å in ~ 5 femtoseconds. Instead of time resolution, the major concern about LIED is the spatial resolution it can achieve due to the rather low electron energy, compared to GED. As we know, changes of internuclear separations in molecular geometrical transformations are on order of 1 Å, so 0.1 Å resolution is more than enough for us to keep track of the structural change in a transient molecule. This result provides the first experimental demonstration of LIED for achieving sub-Angstrom spatial resolution.

An important advantage of using laser-induced rescattering electrons to generate electron-diffraction images is that it can be readily synchronized to perform typical pump-probe measurements. The pump optical beam can be used to initiate a molecular dynamic process[96], e.g. to select a reaction path, and the probe pulse arrives later to monitor the transient structures of the molecule at different time delays after the pump pulse. With the emergence of intense mid-infrared sources in many laboratories, LIED has the potential to become a powerful tool for dynamic imaging of transient molecules with sub-Angstrom spatial and few-femtosecond temporal resolution[68].

Publications

Junliang Xu, Cosmin I. Blaga, Anthony D. DiChiara, Emily Sistrunk, Kaikai Zhang, Zhangjin Chen, Anh-Thu Le, Toru Morishita, C. D. Lin, Pierre Agostini, and Louis F. DiMauro, "Mid-infrared laser-induced electron diffraction for probing the core of rare gas atoms" Phys. Rev. Lett (submitted on Feb 6 2012).

Cosmin I. Blaga, Junliang Xu, Anthony D. DiChiara, Emily Sistrunk, Kaikai Zhang, Pierre Agostini, Terry A. Miller, Louis F. DiMauro, and C. D. Lin, "Imaging ultrafast molecular dynamics with laser-induced electron diffraction", Nature **483**, 194 (2012).

Junliang Xu, Yaqiu Liang, Zhangjin Chen, and C. D. Lin, "Elastic scattering and impact ionization by returning electrons induced in a strong laser field", J. Phys. Conf. Series **288**, 012017 (2011).

Song-Feng Zhao, Junliang Xu, Cheng Jin, Anh-Thu Le, and C. D. Lin, "Effect of orbital symmetry on the orientation dependence of strong field tunneling ionization of nonlinear polyatomic molecules", J. Phys. B **44**, 035601 (2011).

Junliang Xu, Zhangjin Chen, Anh-Thu Le, and C. D. Lin, "Self-imaging of molecules from diffraction spectra by laser-induced rescattering electrons", Phys. Rev. A **82**, 023814 (2010).

Junliang Xu, Hsiao-Ling Zhou, Zhangjin Chen, and C. D. Lin, "Genetic-algorithm implementation of atomic potential reconstruction from differential electron scattering cross sections", Phys. Rev. A **79**, 052508 (2009).

Junliang Xu, Anh-Thu Le, Toru Morishita, and C. D. Lin, "Signature of Ericson fluctuations in helium inelastic scattering cross sections near the double ionization threshold", Phys. Rev. A **78**, 012701 (2008).

Bibliography

[1] A. H. Zewail and J. M. Thomas. *Electron Microscopy: Imaging in Space and Time.* London: Imperial College Press, 2010.

[2] F. C. D. Schryver, S. D. Feyter, and G. Schweitzer, editors. *Femtochemistry.* Weinheim, Germany: WILEY-VCH, 2001.

[3] I. Hargittai and M. Hargittai, editors. *Stereochemical Applications of Gas-Phase Electron Diffraction,* volume I and II. New York: VCH, 1988.

[4] Mark Ladd and Rex Palmer. *Structure Determination by X-ray Crytallography.* New York: Kluwer Cademic/Plenum Publishers, 4th edition, 2003.

[5] H. M. Berman, T. Battistuz, T. N. Bhat, W. F. Bluhm, P. E. Bourne, K. Burkhartdt, Z. Feng, et al. The protein data bank. *Acta Crys. D*, 58:899–907, 2002.

[6] G. E. Bacon. *Neutron Diffraction.* Oxford, 3rd edition, 1975.

[7] J. W. Emsley and J. C. Lindon. *NMR Spectroscopy Using Liquid Crystal Solvents.* Elmsford, New York: Pergamon Press, 1975.

[8] J. W. Moore, C. L. Stanitski, and P. C. Jurs. *Chemistry: The Molecular Science.* Orlando, FL: Harcourt College Publishers, 1st edition, 2002.

[9] A. H. Zewail. The new age of structural dynamics. *Acta Crys. A*, 66:135–136, 2010.

[10] H. N. Chapman. X-ray imaging beyond the limits. *Nature Materials*, 8:299–301, 2009.

[11] F. Carbone, P. Musumeci, O. J. Luiten, and C. Hebert. A perspective on novel sources of ultrafast electron and X-ray pulses. *Chem. Phys.*, 392:1–9, 2012.

[12] J. Kim, K. H. Kim, J. H. Lee, and H. Ihee. Ultrafast X-ray diffraction in liquid, solution and gas: Present status and future prospects. *Acta Crys. A*, 66:270–280, 2010.

[13] C. D. Lin, A. T. Le, Z. Chen, T. Morishita, and R. Lucchese. Strong-field rescattering physics—self-imaging of a molecule by its own electrons. *J. Phys. B*, 43:122001, 2010.

[14] C. Altucci, R. Velotta, and J. P. Marangos. Ultra-fast dynamic imaging: an overview of current techniques, their capabilities and future prospects. *J. Mod. Opt.*, 57:916952, 2010.

[15] E. G. Stout and L. H. Jensen. *X-ray Structure Determination, a Practical Guide.* New York: Macmillan, 1968.

[16] G. Rhodes. *Crystallography Made Crystal Clear.* San Diego: Academic Press, 1993.

[17] Andrew P. Carter, Carol Cho, Lan Jin, and Ronald D. Vale. Crystal structure of the dyein motor domain. *Science*, 331:1159–1165, 2011.

[18] Dmitry Shorokhov and Ahmed H. Zewail. 4D electron imaging: Principles and perspectives. *Phys. Chem. Chem. Phys.*, 10:2879–2893, 2008.

[19] http://www.nobelprize.org/nobel_prizes/physics/laureates/1915/.

[20] Max Born and Emil Wolf. *Principles of Optics.* London: Pergamon Press Ltd, 7th (expanded) edition, 1999.

[21] J. Miao, T. Ishikawa, Q. Shen, and T. Earnest. Extending X-ray crystallography to allow the imaging of noncrystalline materials, cells, and single protein complexes. *Annu. Rev. Phys. Chem.*, 59:387–410, 2008.

[22] H. Mark and R. Wierl. Atomformfaktorbestmmung mit elektronen. *Z. Phys*, 60:741, 1930.

[23] S. Lothar. Electron diffraction as a tool of structural chemistry. *Appl. Spectrosc.*, 30:123–149, 1976.

[24] F. Krasniqi, B. Najjari, L. Strüder, D. Rolles, A. Voitkiv, and J. Ullrich. Imaging molecules from within: Ultrafast angström-scale structure determination of molecules via photoelectron holography using free-electron lasers. *Phys. Rev. A*, 81:033411, 2010.

[25] http://www.nobelprize.org/nobel_prizes/chemistry/laureates/2009/.

[26] Majed Chergui and Ahmed H. Zewail. Electron and X-ray methods of ultrafast structural dynamics: Advances and appliations. *ChemPhysChem*, 10:28–43, 2009.

[27] H. N. Chapman, P. Fromme, A. Barty, T. A. White, R. A. Kirian, A. Aquila, et al. Femtosecond X-ray protein nanocrystallography. *Nature*, 470:73–77, 2011.

[28] J. Miao, H. N. Chapman, J. Kirz, D. Sayre, and K. O. Hodgson. Taking X-ray diffraction to the limit: Macromolecular structures from femtosecond X-ray pulses and diffraction microscopy of cells with synchrotron radiation. *Annu. Rev. Biophys. Biomol. Struct.*, 33:157–176, 2004.

[29] J. Miao, P. Charalambous, J. Kirz, and D. Sayre. Extending the methodology of X-ray crystallography to allow imaging of micrometre-sized non-crystalline specimens. *Nature*, 400:342–344, 1999.

[30] J. Miao, K. O. Hodgson, and D. Sayre. An approach to three-dimensional structures of biomolecules by using single-molecule diffraction images. *Proc. Natl. Acad. Sci. USA*, 98:6641–6645, 2001.

[31] Gilbert N. Lewis. The atom and the molecule. *J. Am. Chem. Soc.*, 38:772, 1916.

[32] H. H. James and A. S. Coolidge. The ground state of the hydrogen molecule. *J. Chem. Phys.*, 1:825–835, 1933.

[33] Linus Pauling. The nature of the chemical bond. III. the transition from one extreme bond type to another. *J. Am. Chem. Soc.*, 54:988–1003, 1932.

[34] H. Eyring and M. Polanyi. Uber einfache gasreaktionen (on simple gas reactions). *Z. Phys. Chem. B*, 12:279–311, 1931.

[35] M. G. Evans and M. Polanyi. Some applications of the transition state method to the calculation of reaction velocities, especially in solution. *Trans. Faraday Soc.*, 31:875, 1935.

[36] Ahmed H. Zewail. Femtochemistry: Atomic-scale dynamics of the chemical bond using ultrafast lasers. *Angew. Chem. Int. Ed.*, 39:2586–2631, 2000.

[37] N. F. Scherer, J. L. Knee, D. D. Smith, and A. H. Zewail. Femtosecond photofragment spectroscopy: The reaction ICN → CN + I. *J. Chem. Phys.*, 89:5141–5143, 1985.

[38] M. Dantus, M. J. Rosker, and A. H. Zewail. Real-time femtosecond probing of "transition states" in chemical reactions. *J. Chem. Phys.*, 87:2395–2397, 1987.

[39] M. J. Rosker, M. Dantus, and A. H. Zewail. Femtosecond real-time probing of reactions. I. the technique. *J. Chem. Phys.*, 89:6113–6127, 1988.

[40] M. Dantus, M. J. Rosker, and A. H. Zewail. Femtosecond real-time probing of reactions. II. the dissociation reaction of ICN. *J. Chem. Phys.*, 89:6128–6134, 1988.

[41] http://www.nobelprize.org/nobel_prizes/chemistry/laureates/1999/.

[42] J. van Tilborg, T. K. Allison, T. W. Wright, M. P. Hertlein, R. W. Falcone, Y. Liu, H. Merdji, et al. Femtosecond isomerization dynamics in the ethylene cation measured in an EUV-pump NIR-probe configuration. *J. Phys. B*, 42:081002, 2009.

[43] Y. H. Jiang, A. Rudenko, O. Herrwerth, L. Foucar, M. Kurka, K. U. Kühnel, M. Lezius, et al. Ultrafast extreme ultraviolet induced isomerization of acetylene cations. *Phys. Rev. Lett.*, 105:263002, 2010.

[44] R. J. D. Miller, R. Ernstorfer, M. Harb, M. Gao, C. T. Hebeisen, H. Jean-Ruel, C. Lu, et al. 'Making the molecular movie': First frame. *Acta Crys. A*, 66:137–156, 2010.

[45] J. R. Dwyer, C. T. Hebeisen, R. Ernstorfer, M. Harb, V. B. Deyirmenjian, R. E. Jordan, and R. J. D. Miller. Femtosecond electron diffraction: 'Making the molecular movie'. *Phil. Trans. R. Soc. A*, 364:741–778, 2006.

[46] A. Rousse, C. Rischel, and J.-C. Gauthier. Colloquium: Femtosecond X-ray crytallography. *Rev. Mod. Phys.*, 73:17–31, 2001.

[47] Ahmed H. Zewail. Femtochemistry: Atomic-scale dynamics of the chemical bond. *J. Phys. Chem. A*, 104:5660–5694, 2000.

[48] R. Srinivasan, V. A. Lobastov, C.-Y. Ruan, and A. H. Zewail. Ultrafast electron diffraction (UED): A new development for the 4D determination of transient molecular structures. *Helvetica Chimica Acta*, 86:1763–1838, 2003.

[49] P. Reckenthaeler, M. Centurion, W. Fuβ, S. A. Trushin, F. Krausz, and E. E. Fill. Time-resolved electron diffraction from selectively aligned molecules. *Phys. Rev. Lett.*, 102:213001, 2009.

[50] A. H. Zewail. 4D ultrafast electron diffraction, crystallography, and microscopy. *Annu. Rev. Phys. Chem.*, 57:65–103, 2006.

[51] A. H. Zewail. Four-dimensional electron microscopy. *Science*, 328:187–193, 2010.

[52] J. Cao, H. Ihee, and A. H. Zewail. Ultrafast electron diffraction and direct observation of transient structures in a chemical reaction. *Proc. Natl. Acad. Sci. USA*, 96:338–342, 1999.

[53] H. Ihee, V. A. Lobastov, U. M. Gomez, B. M. Goodson, R. Srinivasan, C.-Y. Ruan, and A. H. Zewail. Direct imaging of transient molecular structures with ultrafast diffraction. *Science*, 291:458–462, 2001.

[54] B. J. Siwick, J. R. Dwyer, R. E. Jordan, and R. J. D. Miller. An atomic-level view of melting using femtosecond electron diffraction. *Science*, 302:1382–1385, 2003.

[55] M. Dantus, S. B. Kim, J. C. Williamson, and A. H. Zewail. Ultrafast electron diffraction. 5. Experimental time resolution and applications. *J. Phys. Chem.*, 98:2782–2796, 1994.

[56] C. Rischel, A. Rousse, I. Uschmann, P.-A. Albouy, J.-P. Geindre, P. Audebert, J.-C. Gauthier, et al. Femtosecond time-resolved X-ray diffraction from laser-heated organic films. *Nature*, 390:490–492, 1997.

[57] A. Rousse, C. Rischel, S. Fourmaux, I. Uschmann, S. Sebban, G. Grillon, Ph. Balcou, et al. Non-thermal melting in semiconductors measured at femtosecond reslution. *Nature*, 410:65–68, 2001.

[58] Thomas Elsaesser and Michael Woerner. Photoinduced structural dynamics of polar solids studied by femtosecond X-ray diffraction. *Acta Crys. A*, 66:168–178, 2009.

[59] Richard Neutze, Remco Wouts, David van der Spoel, Edgar Weckert, and Janos Hajdu. Potential for bimolecular imaging with femtosecond X-ray pulses. *Nature*, 406:752–757, 2000.

[60] H. N. Chapman, A. Barty, M. J. Bogan, S. Boutet, M. Frank, S. P. Hau-Riege, S. Marchesini, et al. Femtosecond diffractive imaging with a soft-X-ray free-electron laser. *Nature Phys.*, 2:839–843, 2006.

[61] Mark S. Hunter and Petra Fromme. Toward structure determination using membrane-protein nanocrystals and microcrystals. *Methods*, 55:387–404, 2011.

[62] S. H. Lin, A. A. Villaeys, and Y. Fujimura, editors. *Advances In Multi-photon Processes And Spectroscopy*, volume 17. Singapore: World Scientific, 2006. pp.1-28.

[63] S. Baker, J. S. Robinson, C. A. Haworth, H. Teng, R. A. Smith, C. C. Chirilă, M. Lein, et al. Probing proton dynamics in molecules on an attosecond time scale. *Science*, 312:424–427, 2006.

[64] W. Li, X. Zhou, R. Lock, S. Patchkovskii, A. Stolow, H. C. Kapteyn, and M. M. Murnane. Time-resolved dynamics in N_2O_4 probed using high harmonic generation. *Science*, 322:1207–1211, 2008.

[65] M. Meckel, D. Comtois, D. Zeidler, A. Staudte, D. Pavičić, H. C. Bandulet, H. Pépin, et al. Laser-induced electron tunneling and diffraction. *Science*, 320:1478–1482, 2008.

[66] C. Z. Bisgaard, O. J. Clarkin, G. Wu, A. M. D. Lee, O. Geβner, C. C. Hayden, and A. Stolow. Time-resolved molecular frame dynamics of fixed-in-space CS_2 molecules. *Science*, 323:1464–1468, 2009.

[67] Y. Huismans, A. Rouzée, A. Gijsbertsen, J. H. Jungmann, A. S. Smolkowska, P. S. W. M. Logman, F. Lépine, et al. Time-resolved holography with photoelectrons. *Science*, 331:61–64, 2011.

[68] Cosmin I. Blaga, Junliang Xu, Anthony D. DiChiara, Emily Sistrunk, Kaikai Zhang, Zhangjin Chen, Anh-Thu Le, et al. Imaging ultrafast molecular dynamics with laser-induced electron diffraction. *Nature*, 483:194–197, 2012.

[69] M. Aidelsburger, F. O. Kirchner, F. Krausz, and P. Baum. Single-electron pulses for ultrafast diffraction. *Proc. Natl. Acad. Sci. USA*, 107:19714–19719, 2010.

[70] R. Kanya, Y. Morimoto, and K. Yamanouchi. Observation of laser-assisted electron-atom scattering in femtosecond intense laser fields. *Phys. Rev. Lett.*, 105:123202, 2010.

[71] M. Protopapas, C. H. Keitel, and P. L. Knight. Atomic physics with super-high intensity lasers. *Rep. Prog. Phys.*, 60:389–486, 1997.

[72] P. B. Corkum. Plasma perspective on strong field multiphoton ionization. *Phys. Rev. Lett.*, 71:1994–1997, 1993.

[73] K. J. Schafer, Baorui Yang, L. F. DiMauro, and K. C. Kulander. Above threshold ionization beyond the high harmonic cutoff. *Phys. Rev. Lett.*, 70:1599–1602, 1993.

[74] T. Zuo, A. D. Bandrauk, and P. B. Corkum. Laser induced electron diffraction: a new tool for probing ultrafast molecular dynamics. *Chem. Phys. Lett.*, 259:313–320, 1996.

[75] M. Lein, J. P. Marangos, and P. L. Knight. Electron diffraction in above-threshold ionization of molecules. *Phys. Rev. A*, 66:051404(R), 2002.

[76] T. Morishita, A. T. Le, Z. Chen, and C. D. Lin. Accurate retrieval of structural information from laser-induced photoelectron and high-order harmonic spectra by few-cycle laser pulses. *Phys. Rev. Lett.*, 100:013903, 2008.

[77] Z. Chen, A. T. Le, T. Morishta, and C. D. Lin. Quantitative rescattering theory for laser-induced high-energy plateau photoelectron spectra. *Phys. Rev. A*, 79:033409, 2009.

[78] A. T. Le, R. R. Lucchese, S. Tonzani, T. Morishita, and C. D. Lin. Quantitative rescattering theory for high-order harmonics from aligned molecules. *Phys. Rev. A*, 80:013401, 2009.

[79] A. Čerkić, E. Hasović, D. B. Milošević, and W. Becker. High-order above-threshold ionization beyond the first-order Born approximation. *Phys. Rev. A*, 79:033413, 2009.

[80] M. V. Frolov, N. L. Manakov, and A. F. Starace. Analytic formulas for above-threshold ionization or detachment plateau spectra. *Phys. Rev. A*, 79:033406, 2009.

[81] J. Itatani, J. Levesque, D. Zeidler, H. Niikura, H. Pépin, J. C. Kieffer, P. B. Corkum, and D. M. Villeneuve. Tomographic imaging of molecular orbitals. *Nature*, 432:867–871, 2004.

[82] S. Haessler, J. Caillat, W. Boutu, C. Giovanetti-Teixeira, T. Ruchon, T. Auguste, Z. Diveki, et al. Attosecond imaging of molecular electric wavepackets. *Nature Phys.*, 6:200–206, 2010.

[83] C. Vozzi, M. Negro, F. Calegari, G. Sansone, M. Nisoli, S. D. Silvestri, and S. Stagira. Generalized molecular orbital tomography. *Nature Phys.*, 7:822–826, 2011.

[84] V. H. Le, A. T. Le, R. H. Xie, and C. D. Lin. Theoretical analysis of dynamic chemical imaging using high-order harmonic generation. *Phys. Rev. A*, 76:013414, 2007.

[85] Z. B. Walters, S. Tonzani, and C. H. Greene. Limits of the plane wave approximation in the measurement of molecular properties. *J. Phys. Chem. A*, 112:9439–9447, 2008.

[86] M. Spanner, O. Smirnova, P. B. Corkum, and M. Y. Ivanov. Reading diffraction images in strong-field ionization of molecules. *J. Phys. B*, 37:L243–L250, 2004.

[87] M. Busuladžić, A. Gazibegović-Busuladžić, D. B. Milošević, and W. Becker. Angle-resolved high-order above-threshold ionization of a molecule: Sensitive tool for molecular characterization. *Phys. Rev. Lett.*, 100:203003, 2008.

[88] M. Peters, T. T. Nguyen-Dang, C. Cornaggia, S. Saugout, E. Charron, A. Keller, and O. Atabek. Ultrafast molecular imaging by laser-induced electron diffraction. *Phys. Rev. A*, 83:051403(R), 2011.

[89] W. Becker, F. Grasbon, R. Kopold, D. B. Milošević, G. G. Paulus, and H. Walther. Above-threshold ionization: From classical features to quantum effects. *Adv. At. Mol. Opt. Phys.*, 48:35–98, 2002.

[90] Zhangjin Chen, Toru Morishita, Anh-Thu Le, and C. D. Lin. Analysis of two-dimensional high-energy photoelectron momentum distributions in single ionizaiton of atoms by intense laser pulses. *Phys. Rev. A*, 76:043402, 2007.

[91] D. Ray, B. Ulrich, I. Bocharova, C. Maharjan, P. Ranitovic, B. Gramkow, M. Magrakvelidze, et al. Large-angle electron diffraction structure in laser-induced rescattering from rare gases. *Phys. Rev. Lett.*, 100:143002, 2008.

[92] M. Okunishi, T. Morishita, G. Prümper, K. Shimada, C. D. Lin, S. Watanabe, and K. Ueda. Experimental retrieval of target structure information from laser-induced rescattered photoelectron momentum distributions. *Phys. Rev. Lett.*, 100:143001, 2008.

[93] M. Okunishi, H. Niikura, R. R. Lucchese, T. Morishita, and K. Ueda. Extracting electron-ion differential scattering cross sections for partially aligned molecules by laser-induced rescattering photoelectron spectroscopy. *Phys. Rev. Lett.*, 106:063001, 2011.

[94] C. Cornaggia. Electron-ion elastic scattering in molecules probed by laser-induced ionization. *J. Phys. B*, 42:161002, 2009.

[95] A. Gazibegović-Busuladžić, E. Hasović, M. Busuladžić, D. B. Milošević, F. Kelkensberg, W. K. Siu, M. J. J. Vrakking, et al. Above-threshold ionization of diatomic molecules by few-cycle laser pulses. *Phys. Rev. A*, 84:043426, 2011.

[96] Junliang Xu, Zhangjin Chen, Anh-Thu Le, and C. D. Lin. Self-imaging of molecules from diffraction spectra by laser-induced rescattering electrons. *Phys. Rev. A*, 82:023814, 2010.

[97] Junliang Xu, Cosmin I. Blaga, Anthony D. DiChiara, Emily Sistrunk, Kaikai Zhang, Zhangjin Chen, Anh-Thu Le, et al. Laser induced electron diraction for probing rare gas atoms. *Phys. Rev. Lett.* (submitted on Feb 06 2012).

[98] Junliang Xu, Hsiao-Ling Zhou, Zhangjin Chen, and C. D. Lin. Genetic-algorithm implementation of atomic potential reconstruction from differential electron scattering cross sections. *Phys. Rev. A*, 79:052508, 2009.

[99] A. Lovell and K. Amos. Fixed-energy inversion of 5-eV e-Xe-atom scattering. *Phys. Rev. A*, 63:012707, 2000.

[100] David L. Carroll, FORTRAN Genetic Algorithm (GA) Driver, 1999: *http://cuaerospace.com/carroll/ga.html* (accessed in May 2008).

[101] D. E. Goldberg. *Genetic Algorithms in Search, Optimization & Machine Learning.* Massachusetts: Addison-Wesley, 1989.

[102] M. Mitchell. *An Introduction to Genetic Algorithms.* Cambridge, Massachusetts: MIT Press, 1996.

[103] H. Wilson, R. Batra, C. Bert, A. Davis, R. Schapery, D. Stewart, and F. Swinson, editors. *Developments in Theoretical and Applied Mechanics* XVIII. School of Engineering, The University of Alabama, Tuscaloosa, 1996. pp.411-424.

[104] K. A. Berrington, W. B. Eissner, and P. H. Norrington. RMATRX1: Belfast atomic R-matrix codes. *Comput. Phys. Commun.*, 92:290, 1995.

[105] X. M. Tong and C. D. Lin. Empirical formula for static field ionization rates of atoms and molecules by lasers in the barrier-suppression regime. *J. Phys. B*, 38:2593, 2005.

[106] http://physics.nist.gov/PhysRefData/ASD/levels_form.html.

[107] T. Morishita, A. T. Le, Z. Chen, and C. D. Lin. Potential for ultrafast dynamic chemical imaging with few-cycle infrared lasers. *New J. Phys.*, 10:025011, 2008.

[108] M. Okunishi, R. Itaya, K. Shimada, G. Prümper, K. Ueda, M. Busuladžić, A. Gazibegović-Busuladžić, et al. Angle-resolved high-order above-threshold ionization spectra for N_2 and O_2: Measurements and the strong-field approximation. *J. Phys. B*, 41:201004, 2008.

[109] M. Okunishi, R. Itaya, K. Shimada, G. Prümper, K. Ueda, M. Busuladžić, A. Gazibegović-Busuladžić, et al. Two-source double-slit interference in angle-resolved high-energy above-threshold ionization spectra of diatoms. *Phys. Rev. Lett.*, 103:043001, 2009.

[110] S. K. Lee, Y. F. Lin, L. Yan, and W. Li. Laser-induced low energy electron diffraction in aligned molecules. *J. Phys. Chem. A*, 116:1950–1955, 2012.

[111] G. Sciaini and R. J. D. Miller. Femtosecond electron diffraction: Heralding the era of atomically resolved dynamics. *Rep. Prog. Phys.*, 74:096101, 2011.

[112] P. D. McCaffrey, J. K. Dewhurst, D. W. H. Rankin, R. J. Mawhorter, and S. Sharma. Interatomic contributions to high-energy electron-molecule scattering. *J. Chem. Phys.*, 128:204304, 2008.

[113] S. L. Hinchley, D. A. Wann, and D. W. H. Rankin. Structure by theory and experiment: One nationality, two languages. *Int. J. Quant. Chem.*, 101:878–884, 2005.

[114] Howard D. Cohen and U. Fano. Interference in the photo-ionization of molecules. *Phys. Rev.*, 150:30–33, 1966.

[115] X. M. Tong, Z. X. Zhao, and C. D. Lin. Theory of molecular tunneling ionization. *Phys. Rev. A*, 66:033402, 2002.

[116] Song-Feng Zhao, Cheng Jin, Anh-Thu Le, T. F. Jiang, and C. D. Lin. Determination of structure parameters in strong-field tunneling ionization theory of molecules. *Phys. Rev. A*, 81:033423, 2010.

[117] Song-Feng Zhao, Junliang Xu, Cheng Jin, Anh-Thu Le, and C D Lin. Effect of orbital symmetry on the orientation dependence of strong field tunneling ionization of nonlinear polyatomic molecules. *J. Phys. B*, 44:035601, 2011.

[118] T. Morishita, M. Okunishi, K. Shimada, G. Prümper, Z. Chen, S. Watanabe, K. Ueda, and C. D. Lin. Retrieval of experimental differential electronion elastic scattering cross sections from high-energy ATI spectra of rare gas atoms by infrared lasers. *J. Phys. B*, 42:105205, 2009.

[119] T. Morishita, T. Umegaki, S. Watanabe, and C D Lin. High-resolution spatial and temporal microscopy with intense-laser-induced rescattering electrons. *J. Phys. Conf. Ser.*, 194:012011, 2009.

[120] D. F. Register, H. Nishimura, and S. Trajmar. Elastic scattering and vibrational excitation of CO_2 by 4, 10, 20 and 50 eV electrons. *J. Phys. B*, 13:1651–1662, 1980.

[121] I. Iga, M. G. P. Homem, K. T. Mazon, and M.-T. Lee. Elastic and total cross sections for electroncarbon dioxide collisions in the intermediate energy range. *J. Phys. B*, 32:43734388, 1999.

[122] I. Kanik, D. C. McCollum, and J. C. Nickel. Absolute elastic differential scattering cross sections for electron impact on carbon dioxide in the intermediate energy region. *J. Phys. B*, 22:1225–1230, 1989.

[123] H. Tanaka, T. Ishikawa, T. Masai, L. Beosten, M. Takekawa, Y. Itikawa, and M. Kimura. Elastic collisions of low- to intermediate-energy electrons from carbon dioxide: Experimental and theoretical differential cross sections. *Phys. Rev. A*, 57:1798–1808, 1998.

[124] T. Andersen, H. K. Haugen, and H. Hotop. Binding energies in atomic negative ions: III. *J. Phys. Chem. Ref. Data*, 28:1511–1533, 1999.

[125] L. I. Schiff. *Quantum Mechanics*. New York: McGraw-Hill, 3rd edition, 1968. pp.145.

[126] I. Iga, I. P. Sanches, P. Rawat, M. G. P. Homem, and M.-T. Lee. Experimental study

on electronhexafluoroethane (C_2F_6) collisions in the low- and intermediate-energy ranges. *J. Phys. B*, 38:3477–3487, 2005.

[127] H. S. W. Massey and E. C. Bullard. The scattering of electrons by nitrogen molecules. *Proc. Cambridge Phil. Soc.*, 29:511–521, 1933.

[128] H. S. W. Massey. *Electronic and Ionic Impact Phenomena*, volume II. Oxford: Clarendon Press, 1969. Chap. 10.

[129] D. Herrmann, K. Jost, J. Kessler, and M. Fink. Differential cross sections for elastic electron scattering. II. Charge cloud polarization in N_2. *J. Chem. Phys.*, 64:1–5, 1976.

[130] I. Iga, I. P. Sanches, E. de Almeida, R. T. Sugohara, L. Rosani, and M.-T. Lee. Experimental verification on the applicability of the independent-atom model (IAM) for elastic electron-molecule scattering in the intermediate-energy range. *J. Electron Spectrosc. Relat. Phenom.*, 155:7–13, 2007.

[131] L. M. Brescansin, I. Iga, and M.-T. Lee. Elastic and absorption cross sections for electron scattering by ethylene in the intermediate energy range. *J. Phys. B*, 37:471483, 2004.

[132] S. Habershon and A. H. Zewail. Determining molecular structures and conformations directly from electron diffraction using a genetic algorithm. *ChemPhysChem*, 7:353–362, 2006.

[133] Z. Zhou and K. D. M. Harris. Counteracting stagnation in genetic algorithm calculations by implementation of a micro genetic algorithm strategy. *Phys. Chem. Chem. Phys.*, 10:7262–7269, 2008.

[134] Henrik Stapelfeldt and Tamar Seideman. Colloquium: Aligning molecules with strong laser pulses. *Rev. Mod. Phys.*, 75:543557, 2003.

[135] J. C. Williamson and A. H. Zewail. Ultrafast electron diffraction. 4. Molecular structures and coherent dynamics. *J. Phys. Chem.*, 98:2766–2781, 1994.

[136] V. S. Rao, A. Vijay, and A. K. Chandra. A comparative study of the energetics, structures, and mechanisms of the HCN ↔ HNC and LiCN ↔ LiNC isomerizations. *Can. J. Chem.*, 74:1072, 1996.

[137] C. Cornaggia. Molecular rescattering signature in above-threshold ionization. *Phys. Rev. A*, 78:041401(R), 2008.

[138] O. Smirnova, S. Patchkovskii, Y. Mairesse, N. Dudovich, , and M. Y. Ivanov. Strong-field control and spectroscopy of attosecond electron-hole dynamics in molecules. *Proc. Natl. Acad. Sci. USA*, 106:1655616561, 2003.

[139] R. Torres, T. Siegel, L. Brugnera, I. Procino, J. G. Underwood, C. Altucci, R. Velotta, et al. Revealing molecular structure and dynamics through high-order harmonic generation driven by mid-IR fields. *Phys. Rev. A*, 51:051802(R), 2010.

[140] Anthony D. DiChiara, Emily Sistrunk, Terry A. Miller, Pierre Agostini, and Louis F. DiMauro. An investigation of harmonic generation in liquid media with a mid-infrared laser. *Opt. Express*, 17:20959–20965, 2009.

[141] C. P. Hauri, R. B. Lopez-Martens, C. I. Blaga, K. D. Schultz, J. Cryan, R. Chirla, P. Colosimo, G. Doumy, et al. Intense self-compressed, self-phase-stabilized few-cycle pulses at 2 μm from an optical filament. *Opt. Lett.*, 32:868–870, 2007.

[142] C. I. Blaga, F. Catoire, P. Colosimo, G. G. Paulus, H. G. Muller, Pierre Agostini, and Louis F. DiMauro. Strong-field photoionization revisited. *Nature Phys.*, 5:335–338, 2009.

[143] P. Colosimo, G. Doumy, C. I. Blaga, J.. Wheeler, C. Hauri, F. Catoire, J. Tate, et al.

Scaling strong-field interactions towards the classical limit. *Nature Phys.*, 4:386–389, 2008.

[144] L. V. Keldysh. Ionization in the field of a strong electromagnetic wave. *Sov. Phys. JETP*, 20:1945–1950, 1964.

[145] N. B. Delone and V. P. Krainov. Energy and angular electron spectra for the tunnel ionization of atoms by strong low-frequency radiation. *J. Opt. Soc. Am. B*, 8:1207–1211, 1991.

[146] M. Y. Ivanov, M. Spanner, and O. Smirnova. Anatomy of strong field ionization. *J. Mod. Opt.*, 52:165–184, 2005.

[147] L. Arissian, C. Smeenk, F. Turner, C. Trallero, A. V. Sokolov, D. M. Villeneuve, A. Staudte, and P. B. Corkum. Direct test of laser tunneling with electron momentum imaging. *Phys. Rev. Lett.*, 105:133002, 2010.

[148] J. F. Williams and B. A. Willis. The scattering of electrons from inert gases I. Absolute differential elastic cross sections for argon atoms. *J. Phys. B*, 8:1670–1682, 1975.

[149] A. Danjo. Electron scattering from Kr: I. Differential cross section for elastic scattering. *J. Phys. B*, 21:3759–3766, 1988.

[150] D. F. Register, L. Vuskovic, and S. Trajmar. Elastic electron scattering cross sections for Xe in the 1-100 ev impact energy region. *J. Phys. B*, 19:1685–1697, 1986.

[151] Sultana N. Nahar and J. M. Wadehra. Elastic scattering of positions and electrons by argon. *Phys. Rev. A*, 35:2051–2064, 1987.

[152] J. E. Sienkiewiczt and W. E. Baylis. Differential cross sections for the elastic scattering of electrons from krypton. *J. Phys. B*, 25:2081–2088, 1992.

[153] R. P. McEachran and A. D. Stauffer. Elastic scattering of electrons from krypton and xenon. *J. Phys. B*, 17:2507–2518, 1984.

[154] J. Levesque, D. Zeidler, J. P. Marangos, P. B. Corkum, and D. M. Villeneuve. High harmonic generation and the role of atomic orbital wave functions. *Phys. Rev. Lett.*, 98:183903, 2007.

[155] B. H. Bransden and C. J. Joachain. *Physics of Atoms and Molecules*. New York: Prentice-Hall, 2nd edition, 2003.

[156] R. L. Dekock and H. B. Gray. *Chemical Structure and Bonding*. Sausalito CA: University Science Books, 1989. pp.229.

[157] M. J. Brunger and S. J. Buckman. Electron-molecule scattering cross-sections. I. experimental techniques and data for diatomic molecules. *Phys. Rep.*, 357:215–458, 2002.

[158] B. Marinkovic, C. Szmytkowski, V. Pejcev, D. Filipovic, and L. Vuskovic. Differential cross sections for elastic and inelastic scattering of electrons by N_2O in the range from 10-80 eV. *J. Phys. B*, 98:2365–2375, 1986.

Appendix A

Copyright Policies of American Physical Society (APS) and Nature Publishing Group (NPG)

A.1   APS Copyright Policies

APS Copyright Policies: http://publish.aps.org/pub_rights.html.

The following text is excerpted from APS Copyright FAQ [http://publish.aps.org/copyright FAQ.html]:

"As the author of an APS-published article, may I include my article or a portion of my article in my thesis or dissertation?

Yes, the author has the right to use the article or a portion of the article in a thesis or dissertation without requesting permission from APS, provided the bibliographic citation and the APS copyright credit line are given on the appropriate pages."

A.2   NPG Copyright Policies

NPG Copyright Policies: http://www.nature.com/reprints/index.html.

The following text is excerpted from Permissions Requests from NPG [http://www.nature.com/reprints/permission-requests.html]:

"**Author Requests**

If you are the author of this content (or his/her designated agent) please read the following. Since 2003, ownership of copyright in in original research articles remains with the Authors*, and provided that, when reproducing the Contribution or extracts from it, the Authors acknowledge first and reference publication in the Journal, the Authors retain the following non-exclusive rights:

a. To reproduce the Contribution in whole or in part in any printed volume (book or thesis) of which they are the author(s).

b. They and any academic institution where they work at the time may reproduce the Contribution for the purpose of course teaching.

c. To reuse figures or tables created by them and contained in the Contribution in other works created by them.

d. To post a copy of the Contribution as accepted for publication after peer review (in Word or Tex format) on the Author's own web site, or the Author's institutional repository, or the Author's funding body's archive, six months after publication of the printed or online edition of the Journal, provided that they also link to the Journal article on NPG's web site (eg through the DOI).

NPG encourages the self-archiving of the accepted version of your manuscript in your funding agency's or institution's repository, six months after publication. This policy complements the recently announced policies of the US National Institutes of Health, Wellcome Trust and other research funding bodies around the world. NPG recognizes the efforts of funding bodies to increase access to the research they fund, and we strongly encourage authors to participate in such efforts.

Authors wishing to use the published version of their article for promotional use or on a web site must request in the normal way.

If you require further assistance please read NPG's online author reuse guidelines.

Note: British Journal of Cancer and Clinical Pharmacology & Therapeutics maintain

copyright polices of their own that are different from the general NPG policies. Please consult these journals to learn more.

* Commissioned material is still subject to copyright transfer conditions"